MEMBRANE TENSION HOMEOSTASIS OF MAMMALIAN CELLS

-MECHANOSENSITIVE STUDY OF THE AREA REGULATION OF ADHERENT CELLS

DISSERTATION

for the award of the degree
“Doctor rerum naturalium”
of the Georg-August-Universität Göttingen

within the doctoral program International Max Planck Research School
“Physics of Biological and Complex Systems”
of the Georg-August University School of Science (GAUSS)

submitted by
Bastian Rouven Brückner
from Stadtoldendorf / Germany

Göttingen, 2016

Thesis Committee
Prof. Dr. Andreas Janshoff
Institute of Physical Chemistry
Georg August University of Göttingen

Prof. Dr. Sarah Köster
Institute for X-Ray Physics
Georg August University of Göttingen

Prof. Dr. Mikael Simons
Cellular Neuroscience
Max-Planck-Institute of Experimental Medicine

Members of the Examination Board
Referee:
Prof. Dr. Andreas Janshoff, Institute of Physical Chemistry,
Georg August University of Göttingen

2nd Referee:
Prof. Dr. Sarah Köster, Institute for X-Ray Physics,
Georg August University of Göttingen

Further Members of the Examination Board
Prof. Dr. Mikael Simons, Cellular Neuroscience,
Max-Planck-Institute of Experimental Medicine

Prof. Dr. Michael Meinecke, Department of Biochemistry II,
Georg August University of Göttingen

Dr. Florian Rehfeldt, 3rd Institute of Physics – Biophysics,
Georg August University of Göttingen

Prof. Dr. Silvio O. Rizzoli, Dept. of Neuro- and Sensory Physiology,
University Medical Center Göttingen

Date of oral examination: 03.06.2016

I, Bastian Rouven Brückner, hereby certify that my doctoral thesis entitled “Membrane tension homeostasis of mammalian cells -mechanosensitive study of the area regulation of adherent cells” has been written independently and with no other sources and aids than quoted.

Göttingen, Germany, 10.04.2017

Bastian Rouven Brückner

to my family

„Wenn man auf ein Ziel zugeht,
ist es äußerst wichtig, auf den Weg zu achten.
Denn der Weg lehrt uns am besten, ans Ziel zu gelangen,
und er bereichert uns, während wir ihn zurücklegen.“
Paulo Coelho,
brasilianischer Schriftsteller

Table of Content

Abstract

Although a cell is the smallest unit that is viable on its own, its construction and processes are of great complexity. Many functions, which keep a cell alive, are only poorly understood up to now. Plasma membrane tension is supposed to be a key player in controlling a variety of cellular functions, such as cell migration, division or apoptosis. In order to investigate how membrane tension is controlled by enlargement or reduction of excess surface area, polarised epithelial cell monolayers were studied. Madin-Darby canine kidney cells (MDCK II) serve as a cellular model system to unravel the question how tension-driven membrane surface area regulation is realised to accommodate tension changes. The mechanical behaviour of cells was measured by force-indentation experiments followed by membrane tether extraction. These experiments carried out by atomic force microscopy (AFM) in conjunction with the application of a powerful mechanical model, the tension model, provide a deep insight into the interplay between tension control and excess surface area regulation. The performance of the tension model in reproducing the mechanical behaviour of plasma membranes was investigated. In order to provoke tremendous changes in the mechanical behaviour of cells, the role of the cytoskeleton for tension homeostasis was unravelled. Since the membrane-cytoskeleton attachment dominates membrane tension, the importance of the linker molecule ezrin was studied by ezrin depletion. Cells stabilise each other in a confluent monolayer by forming tight connections to neighbouring cells. Tight junctions mediated by *zonula occludens-1* and adherens junctions built up by E-cadherins are important cell-cell connections in MDCK II cells. The role of both proteins for tension homeostasis was clarified by experiments disrupting one or the other connection. Furthermore, the role of endocytosis, a process driven by membrane surface area changes and cytoskeleton rearrangement, was investigated in terms of tension and membrane surface area adjustment.

In summary, this study allows us to draw a comprehensive picture of membrane tension homeostasis by surface area regulation. Our data demonstrate the importance of an intact cytoskeleton and an intact membrane-cytoskeleton interface for tension maintenance. Alterations of the cellular morphology of the cell monolayer

do not necessarily provoke an altered mechanical behaviour of the cells, as long as the cytoskeleton is unaffected and a stable contact to binding partners is maintained.

1 Introduction

Since the beginning of modern science humans have tried to gain a deep understanding of the origin of all life, built up by biological membranes and cells. Up to now, intensive research enabled a distinct understanding in the organisation of lipids, proteins, and cellular compounds. Cells are very complex biological systems. Thus, there are many open questions that still need to be investigated and clarified. In the last years, scientists found that cells are highly sensitive to their environment [1]. In cancer research it was found that *maligne* cells behave totally different from *benigne* ones, which is reflected in the mechanical behaviour of those cells [2]. Forces and mechanics in general play a pivotal role for cells. Signal cascades can be initiated by external cues, such as forces and stress [3]. Since the mechanical behaviour of cells can be used as a measure for different cellular properties, different techniques were investigated to study cellular mechanics. One of the first methods was micropipette aspiration [4,5]. In order to deform the plasma membrane of a cell, the lipid bilayer is aspirated into a small micropipette. By measuring the deformation induced by the applied force, mechanical properties of the specimen can be determined [5-7]. This technique is limited to cells in suspension. In order to apply forces to adherent cells, one of the most commonly used methods is to indent their plasma membrane with a small probe. Atomic force microscopy is a very sensitive method to measure small forces beginning in the range of tens of pN [8]. Furthermore, the atomic force microscope can be used to determine the topographical properties of the sample by scanning laterally across the surface [9]. Since the AFM provides these two methods for cell analysis, this technique will be used in this study as one of the main techniques. In order to quantify the data measured by AFM indentation experiments, various mechanical modelling approaches were developed for different samples and cell types. While classical approaches do not take into account the often quite intricate architecture of the probed sample, newer models were specifically developed for distinct cell shapes [10-12]. In this study the tension model will be used to investigate the mechanical behaviour of confluent epithelial cell monolayers. Since the tension model was introduced in 2005 by Sen and co-workers and adapted in 2012 by Pietuch, no one has verified yet that this model is independent of the shape of the indenter [10,13].

The results gained by other models depend on the indenter shape [14]. Verification of the indenter independency for the tension model will be one aim of the present study.

However, the mechanical behaviour of cells is inevitably connected to different cellular properties. Here, the focus is set on epithelial cells. This class of cells surrounds and shields deeper cell layers of an organ. In order to provide stability and shape, the cell is supported by a cytoskeleton. While microtubuli and intermediate filaments are mainly located in the inner region of a cell, filamentous actin fences the whole plasma membrane at the cytoplasmic side. To enhance the cellular stability, the plasma membrane is connected to the F-actin cytoskeleton by specific binding proteins out of the ezrin-radixin-moesin family. Furthermore, cells are connected to their neighbours via specific junctional proteins such as *zonula occludens-1* or E-cadherin.

Epithelial cells constitute a tight and stable network with a defined tension. This tension is known as an important regulator in a variety of cellular processes such as cell migration [15,16], membrane repair [17], osmoregulation [18], and cell spreading [19-21]. During all of these processes the cell undergoes tension changes. In order to compensate the lateral stress of the plasma membrane, membrane reservoirs have to be disintegrated to avoid membrane lysis [22]. Active contraction of the cellular cytoskeleton as well as the connection between plasma membrane and the underlying cytoskeleton contribute to the overall or in-plane tension of the membrane. Different studies conclude that plasma membrane-cytoskeleton linking proteins function as tension regulators in eukaryotic cells [23-26].

Furthermore, membrane protrusions or invaginations can have an impact on the mechanical behaviour of the plasma membrane. Owing to its liquid-crystalline structure, the plasma membrane is largely inextensible (up to 2-3%) [27]. To avoid membrane lysis due to tension changes, cells react to such stresses by surface area regulation. For instance, one strategy can be the recruitment of excess membrane area, stored in wrinkles and infoldings or exo- and endocytosis of vesicles. The membrane tension of a typical cell is 100 to 1000 times below the membrane lysis tension [12,28,29]. When the plasma membrane is uncoupled from the cytoskeleton, even lower tension values could be observed [30,31].

All these findings lead to the conclusion that cells control their tension by membrane remodelling mechanisms. However, until today it is only poorly understood which cellular compartments are mainly responsible for membrane tension homeostasis of epithelial cells. In the present study, the role of a variety of different cellular proteins determining the cell structure and cellular processes will be investigated in terms of tension homeostasis. In a first approach, the role of the cellular structure stabilizing F-actin will be studied in both ways, after either degradation or reinforcement of F-actin. In a second step, the study will focus on the membrane-cytoskeleton interface. Here ezrin depletion will be achieved in two different ways. A pure chemical one will be the application of a drug such as NSC 668394. Additionally, a genetic suppression will be achieved by application of short interference RNA. Together with previous studies concerning the role of ezrin binding sites in the plasma membrane [23,32], it will be possible to draw a comprehensive picture of how the complex interplay between plasma membrane and underlying cytoskeleton influences the mechanical behaviour of epithelial cells.
In a confluent cell monolayer cells are not separated from each other. They form a dense cellular network with tight connections (*vide supra*). To address the question how these connections influence the mechanics of the cells, the focus will be set on tight junctions, which are the uppermost cell-cell connection. As in the previous experiment, short interference RNA will be applied to deplete the expression of the tight junction protein *ZO-1*. The second cell-cell-junctional protein which will be investigated, is the E-cadherin mediated adherens junction belt. Here the cadherin-mediated connection will be impaired by a chemical inducing a conformational change of the protein. These two approaches will allow a better understanding of how tension maintenance relies on an intact cell monolayer.
At the end of the study a process that relies on excess membrane material acquisition in conjunction with F-actin remodelling will be investigated. The endocytosis machinery of cells controls the formation and internalisation of plasma membrane invaginations. This part of the study will address the question if tension homeostasis can be realised, when either endocytosis is blocked or the endocytosis rate is enhanced.
Altogether, fundamental cellular compartments and their role for membrane tension homeostasis will be investigated. The ultimate goal is to garner a detailed picture of

how tension homeostasis is realised in epithelial cells through membrane surface area regulation.

2 Principles

2.1 Eukaryotic Cells

All life is built up from cells. These small units are often viable on their own and can replicate independently. Although there are many different types of cells, most of them share the same facilities in basic functions. In general, cells can be divided into two classes: the first one, called prokaryotic cells, has neither internal membranes nor intracellular organelles. There is no nucleus and the whole cell is built up in a primitive way. Bacteria such as *Escherichia coli* belong to this group. The second class comprises the group of eukaryotic cells. Here, the cell compartments are divided from each other via internal membranes. Each eukaryotic cell contains a nucleus holding the genetic information. Eukaryotes are thus far more developed than prokaryotes. All plant and animal cells are eukaryotic cells.

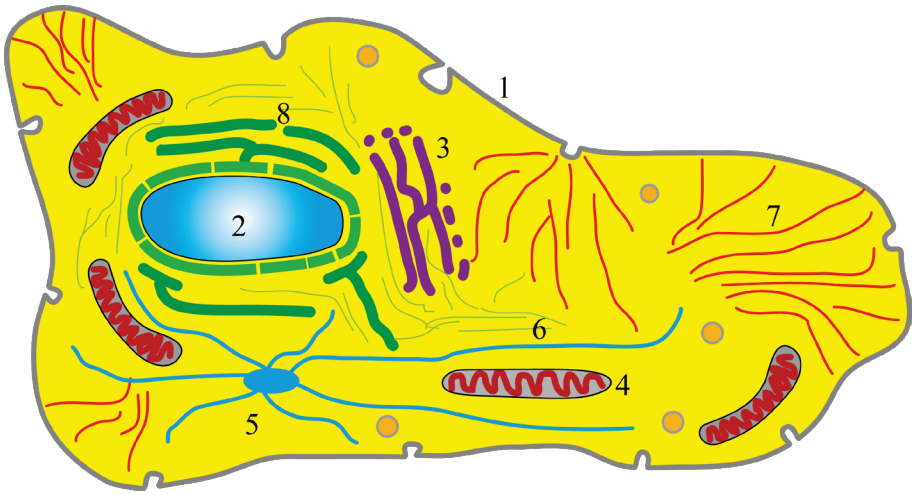

Figure 2.1: **Schematic view of an eukaryotic cell showing important organelles. 1: Plasma membrane. 2: Nucleus, surrounded by a nuclear envelope. 3: Golgi apparatus. 4: Mitochondria. 5: Centrosome with microtubules. 6: Intermediate filaments. 7: Actin filaments. 8: Endoplasmic reticulum.**

Eukaryotic cells contain many different organelles and proteins, tightly packed, highly organised and surrounded by the cytoplasm. Countless processes in the cell,

at the cell surface, and interactions between cells are necessary to stay alive. In this study, the focus is set on eukaryotic cells, more precisely on epithelial cells. Since this work addresses questions regarding the mechanical behaviour of cells, only cellular elements playing a role in this context will be introduced. A more comprehensive and detailed introduction of cellular structures is given in prominent text books, such as the definitive work “Molecular Biology of the Cell” written by Bruce Alberts and co-workers. Fundamental components of an eukaryotic cell are shown in Figure 2.1.

The cell is segregated from its surrounding by a lipid bilayer (1). The whole genetic information is stored in the DNA, located in the cellular nucleus, which is surrounded by a nuclear envelope (2). Material can be released and internalised by nuclear pores in this double membrane layer. Proteins, which have to traverse the cell to a certain place, are encapsulated by the golgi apparatus (3) into a vesicle. Mitochondria (4) are the power plant of the cell producing ATP. Microtubules (5), intermediate filaments (6) and actin filaments (7) form the cytoskeleton of the cell. Proteins and lipids are produced at the endoplasmic reticulum (8). Actin will be introduced in a more detailed way in chapter 2.5.

2.2 Madin-Darby Canine Kidney Cells

Madin-Darby Canine Kidney (MDCK) cells are widely used as a model system for epithelial cells. They show a clear apical-basolateral polarity, grow relatively fast and are easy to handle in the laboratory. Additionally, these cells are very tractable during experimentation [33]. However, there exist different types of MDCK cells in different cell databases. The European Collection of Authenticated Cell Cultures (ECACC, [34]) provides six different type of MDCK cells. In the American Type Culture Collection (ATCC, [35]) nine different MDCK cell lines are available (correct as of March 2016). In most of the studies MDCK I and MDCK II cells were used. Both strains originate from the parental MDCK cell line, which was established in 1958 by Madin and Darby [36]. They derived the cells from an adult female cocker spaniel. Gaush *et al.* characterized the cells for the first time [37]. It was found that those cells are not clonal. Moreover, differences in cell size or an apical cilium were found [38]. Since these differences exist, MDCK cells do not serve as an adequate model system. Thus, two sub-clones of MDCK cells, MDCK I and MDCK II, were derived from the parental cell line [39,40]. Type I MDCK cells were derived from a low passage of the parental cell line. They were found to be smaller and flatter compared to MDCK II cells, which were derived from a higher passage of MDCK cells. Differences in the trans-epithelial resistance *TER* as a measure for cell-cell connectivity demonstrate that MDCK I cells built up a very closely connected cellular network ($TER > 4000\ \Omega / \mathrm{cm}^2$) compared to MDCK II cells ($TER < 300\ \Omega / \mathrm{cm}^2$).

Both cell lines are widely used as a model system for epithelial cells. Due to the fact that in the ECACC description of MDCK I cells it can be found that the phenotype may be unstable and an incomplete harvesting of confluent cells may select for a smooth muscle cell phenotype [41], MDCK II cells are the most commonly used strain of MDCK cells. One disadvantage of all types of MDCK cells is their canine origin, since many commonly available antibodies and siRNAs are designed and tested for cells of other origin, such as human.

However, MDCK II cells are a well-known model system for epithelial cells, which are widely used in cell research.

2.3 The Cellular Plasma Membrane

The cellular plasma membrane is a lipid bilayer shielding a cell from its environment. It is highly ordered. Phospholipids, such as phosphatidylcholine or phosphatidylethanolamine, are the main components [42]. All lipids have a hydrophilic head group facing outwards and a hydrophobic alkyl chain facing inside the membrane. The lipids move freely within the membrane with a lateral diffusion coefficient of about $D \approx 1\,\mu m/s$ [43]. In addition, the plasma membrane contains cholesterol. Cholesterol is an amphipathic molecule, which arranges its hydroxyl group with the phospholipid head groups. The residue faces to the inside of the membrane. The important interaction between phospholipids and cholesterol reduces the fluidity of the membrane since cholesterol has a small head group and a big tail.

Besides lipid molecules many proteins are present in the membrane. Some only occur in the inner or outer leaflet, other pervade the full lipid bilayer (Figure 2.2). In general, the lipid composition of the inner and outer leaflet is not alike. Bulky head groups in one layer enable curvature of the membrane. In epithelial cells the plasma membrane is polarised. The lipid composition of the upper part of the cell (apical side) differs from the lower (basal) part. The apical side forms a robust barrier that shields the underlying tissue against external aggressors in the environment. Therefore, a glycosphingolipid- and cholesterol enriched membrane can be found at the apical side in MDCK cells [44,45].

Due to its liquid-crystalline structure, the plasma membrane is largely inextensible, only up to 2-3%. The lipid bilayer is highly connected to inner cellular structures, to the environment and to surrounding cells. Specific lipids and proteins are responsible for these connections. A strong linkage of the plasma membrane to the underlying cytoskeleton provides shape and stability of the cell (Figure 2.2 and Figure 2.5). Specific lipids or proteins in the inner membrane leaflet are responsible for establishing this strong binding. One of the best known binding site is phosphatidylinositol 4,5-bisphosphate (PIP_2). The linkage between PIP_2 and the F-actin cytoskeleton is mediated by specific linker proteins [46].

2.4 The Membrane-Cytoskeleton Interface

Alongside with radixin and moesin, ezrin is one of the three linker proteins of the ERM family. Endothelial cells mainly express moesin, whereas epithelial cells mainly contain ezrin [47]. In this study the focus is set on ezrin since MDCK cells mainly express this ERM protein [48]. At the N-terminal side of all members of the ERM family, however, a 4.1 ezrin, radixin, moesin domain (FERM domain) is located. The protein binds via this approximately 300 amino acids long domain to PIP_2 in the plasma membrane. On the C-terminal end an ezrin, radixin, moesin association domain (C-ERMAD) enables linkage to the F-actin cytoskeleton. An α-helical region connects both ends of the protein. For ezrin the last 80 amino acids of C-ERMAD have a high affinity to bind to the FERM domain [46]. Thus, most of the ezrin is in the dormant state, where C- and N-terminal region are associated to each other [49]. To open this conformation, PIP_2 must be present in the lipid bilayer. The opening is often accompanied by phosphorylation of the specific threonine residue Thr-567 [50-52]. When ezrin is activated, a connection to PIP_2 in the membrane and to actin filaments will be formed [23,52,53]. Figure 2.2 summarises the structure of a lipid bilayer and visualises the connection between plasma membrane and cytoskeleton mediated by ezrin.

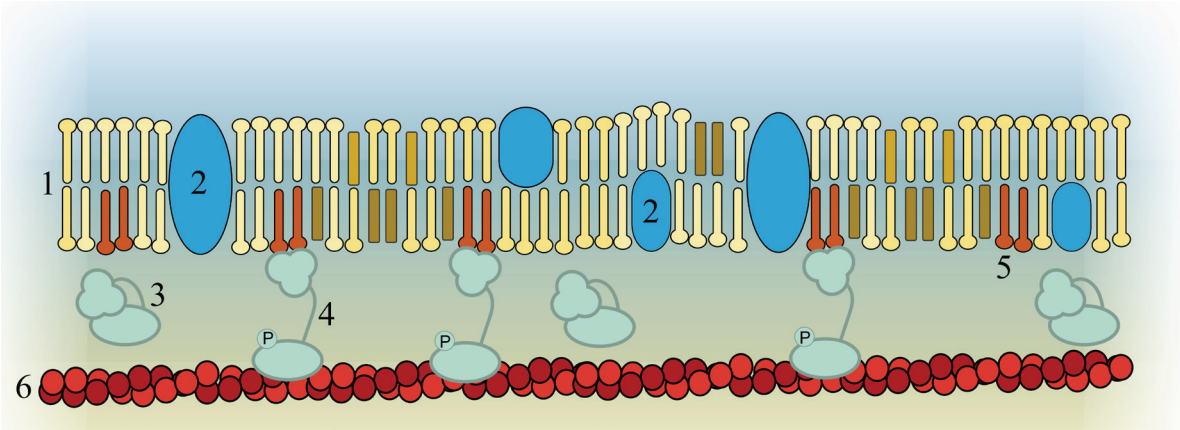

Figure 2.2: **The plasma membrane and its connection to the underlying cytoskeleton. 1: Lipid bilayer containing different lipids and cholesterol. 2: Membrane proteins. 3: Dormant ezrin. 4: Activated ezrin, binding to PIP_2 (5) in the plasma membrane via a FERM domain and to the F-actin cytoskeleton (6) via C-ERMAD.**

Apart from fulfilling an important linker function by connecting plasma membrane and underlying cytoskeleton, ezrin is involved in many cellular processes, such as membrane dynamics, adhesion, and forming protrusions [54]. Moreover, it is involved in physiology and disease. Many different studies show that tumour metastasis is promoted by ezrin. An enhanced expression of the protein was found in metastatic tumours, for e.g. human or mouse *osteosarcomas* and *rhabdomyosarcomas* [55]. An up- and downregulation occurs in different stages of *osteosarcoma* metastasis [56]. However, there is clear evidence that the interplay between plasma membrane, linker molecules, such as ezrin, and the cytoskeleton are important for the structure and the mechanical behaviour of cells.

2.5 The Cytoskeleton of the Cell

The cytoskeleton of a cell provides stability and shape [57,58]. The mechanical behaviour is heavily reliant on the arrangement of the cytoskeleton [2]. Furthermore, it is involved in many cellular processes, such as cell migration [15], cell division [59], and endocytosis [60]. Three different protein types belong to the cellular cytoskeleton: Microtubules, intermediate filaments, and actin filaments. Since the focus of this study is set to the F-actin cytoskeleton, this is the only cytoskeletal protein discussed here.

Actin filaments are right-handed twisted structures formed by polymerisation of actin monomers, so-called globular actin (G-actin). The time determining step is given by the association of two or three 42 kDa G-actin proteins to form dimers and trimers [61]. This nucleation process is thermodynamically limited. Further polymerisation is very fast, depending on the polymerisation side, since actin has a "+"-end (barbed end) and a "-"-end (pointed end), and on the G-actin concentration ("critical concentration" at the barbed end: 0.1 µM [62]). On the barbed end polymerisation is favoured. The polymerisation rate (11.6 $\mu M^{-1}s^{-1}$) is approximately ten times higher compared to the pointed end of actin. The building process of actin to filaments with a diameter of approximately 8 nm is ATP-driven [63].

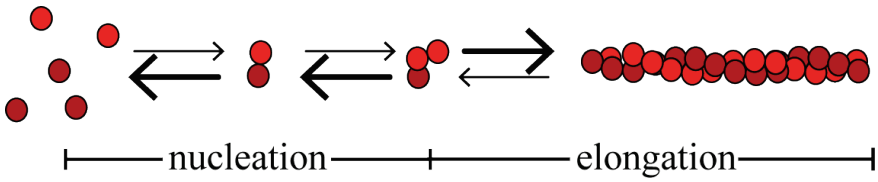

Figure 2.3: Actin filaments are built up from single actin molecules (G-actin). After association of a few G-actin proteins (nucleation), a fast growing occurs (elongation) ending in filaments.

F-actin has a persistence length of 10 µm [64]. The polymerisation mechanism is highly controlled (Figure 2.3). Specific proteins, such as profilin, cap globular actin molecules [65,66]. The G-actin concentration is lowered and prolongation is hindered. To ensure that not only existing actin filaments grow on the favoured barbed end but also new bundles and branched bundles can arise, the actin related

protein complex 2/3 (Arp2/3) uses profilin capped monomers and enables polymerisation of new actin structures. Furthermore, the actin polymerisation rate can be significantly increased at the barbed end by coaction of profilin with formin [67]. All these processes acting together results in a well-balanced state, the so-called actin homeostasis.

Actin is largely dispersed over the cell. The whole plasma membrane is supported by a thin (several hundred nanometres) actin network, the so-called cortex [68]. At the apical side of epithelial cells, small finger-like protrusions face out of the plasma membrane in the direction of the lumen. These microvilli are stabilised by parallel actin bundles (Figure 2.5) [69,70]. At the basal side, anti-parallel ordered bundles form stress fibres, which are connected to integrins to form focal adhesion points to the environment [71,72]. The cellular cytoskeleton is linked to the plasma membrane via specific binding proteins, such as ezrin (see chapter 2.3). In addition, actin is connected to different cell-cell junction proteins. It binds to E-cadherins of adherens junctions in the plasma membrane together with myosin II [73] and to tight junctions [74] (see also chapter 2.6 and Figure 2.5).

In order to form these various multi-dimensional actin structures, F-actin interacts with different binding partners to crosslink the network. α-actinin and filamin are long linker proteins, which combine actin fibres to loose networks or bundles [75]. Shorter linker molecules enable the formation of tightly arranged F-actin bundles in parallel, anti-parallel or mixed arrangement. Prominent examples for short linkers are fascin and fimbrin [64]. To generate specific and directed forces, motor proteins are necessary. Myosin binds to antiparallel actin bundles and can contract in an ATP-driven process. Actin bundles are buckled [59,76]. In single cells, an F-actin-myosin II belt is responsible for local tension generation [77]. Apart from single F-actin-myosin interactions the overall viscoelastic properties of a branched F-actin network can be more fluid caused by myosin II [78]. Furthermore, it is discussed whether myosin could also rupture actin filaments [79]. A variety of studies demonstrated that myosin II, located at the apical cell side, is important for contractile force generation in different cell types [80-82]. However, up to now it is only poorly understood how cells realise an apical actomyosin contraction. Phosphorylation of myosin II was found to generate contractile pulses [83].

In summary, the actin cytoskeleton is a highly organised, adaptable and important protein network. It provides cellular stability, organises and maintains the shape and is important for the mechanical behaviour of cells.

To investigate the role of the cytoskeleton and to study the impact of different manipulations, a variety of drugs are commonly available. Most of them are natural toxins, which are produced in organisms for self-defence. An overview of drugs affecting the actin cytoskeleton is given in Table 2.1. In this study Latrunculin A and Jasplakinolide will be used.

Table 2.1: Overview of drugs affecting the cellular actin cytoskeleton.

Drug	Mode of action
Cytochalasin D	Binds to actin filaments, blocks prolongation
Latrunculin A	Binds one-to-one to G-actin, blocks polymerisation
Swinholide	Blocks dimers, cuts actin filaments
Phalloidin	Binds to actin filaments, prevents disruption of filaments
Jasplakinolide	Increases actin polymerisation

2.6 Cells in Contact to their Neighbourhood

Epithelial cells are not separated organisms. When cells separate from each other, they lose their polarisation, in most cases they eventually die. Cancer cells, on the other hand, do not die necessarily after uncoupling from the environment. Healthy, non-malignant cells are connected to each other by different classes of junctions. Since epithelia line organs and blood vessels, a tight connection protecting the underlying tissue and controlling the flux of substances from and into the lumen is inevitable. Desmosomes, together with tight junctions and adherens junctions, form the epithelial junctional complex. Desmosomes interact with intermediate filaments on the intercellular side. Tight and adherens junctions interact with F-actin. This study focuses on those two classes of intercellular contacts. Both will be described in the following chapters. Figure 2.4 shows the tight and adherens junctions in the lateral plasma membrane.

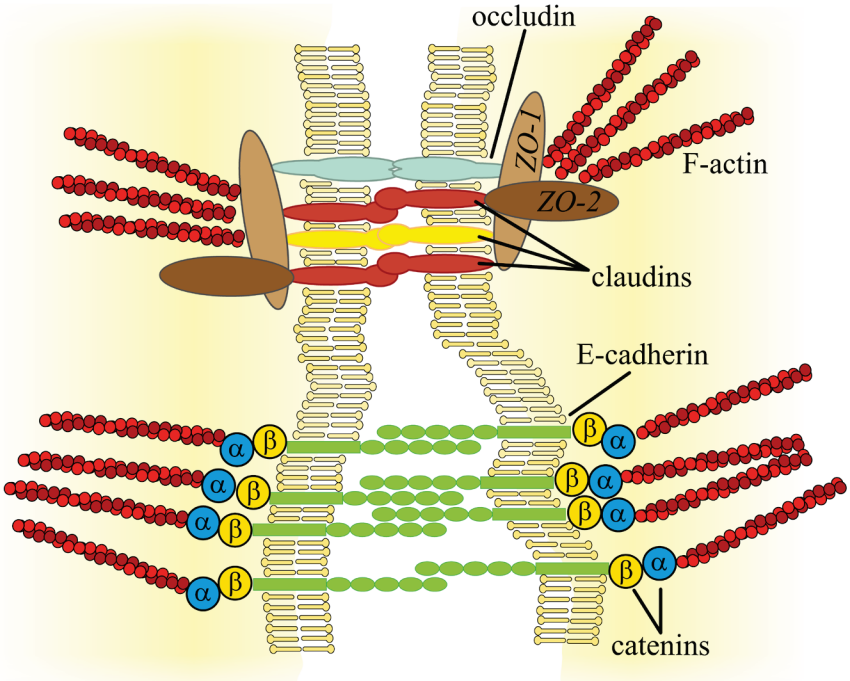

Figure 2.4: **Scheme showing the connection between two cells mediated by tight junctions (top) or adherens junctions (bottom). Tight junctions are formed by occludin and claudins. At the cytoplasmic side *zonula occludens* binds to these transmembrane proteins and mediates a connection to the F-actin cytoskeleton. Adherens junctions are built up in epithelial cells by E-cadherins, whose ectodomains associate with each other. Inside the cell F-actin binds to α-catenins, which are connected to β-catenins. β-catenins bind in term to E-cadherin.**

2.6.1 Tight Junctions

Tight junctions are the uppermost apical cell-cell connections. They have two different functions. By forming a tight connection between cells and closing the intercellular space, tight junctions control the diffusion along the paracellular pathway. Different transmembrane proteins built up a fence. Thus, apical membrane domains cannot diffuse to the basal side and *vice versa*. The extracellular domain of transmembrane proteins from neighbouring cells, such as claudins and occludins, associate to one another [84]. Junctional adhesion molecules form the third group of tight junction transmembrane proteins.

Inside the cell different proteins form the cytoplasmic plaque of tight junctions. It regulates e.g. paracellular adhesion. The first identified member of the cytoplasmic plaque was the tight junction protein 1, *zonula occludens-1* (*ZO-1*). *ZO-1* regulates the assembly of tight junctions and can interact with F-actin [85,86]. Figure 2.4 visualises the tight junction-mediated connection between two cells.

2.6.2 Adherens Junctions

Alongside tight junctions, adherens junctions form the most important cell-cell connections on the apical cell side. Adherens junctions are placed just beneath the tight junctions. Depending on the cell type, different transmembrane proteins form the adherens belt of a cell. In epithelial cells, E-cadherins are responsible to build up adherens junctions. Cadherins span the membrane. The ectodomain contains five repeats of the so-called cadherin domain. Cadherins form a homophilic adhesion to the cadherins of adjacent cells [87]. The association is calcium dependent. Removal of calcium leads to detachment of the cadherin-cadherin connection. This process is fully reversible [88,89]. The innercellular domain connects the F-actin cytoskeleton to the membrane via catenins and other anchor proteins (Figure 2.4). Thus, cadherins enable cells to build up a stable actin network, the so-called contractile ring [90].

A side-view of an epithelial cell is shown in Figure 2.5. The distribution of important cell features, which will be investigated in this study, are highlighted.

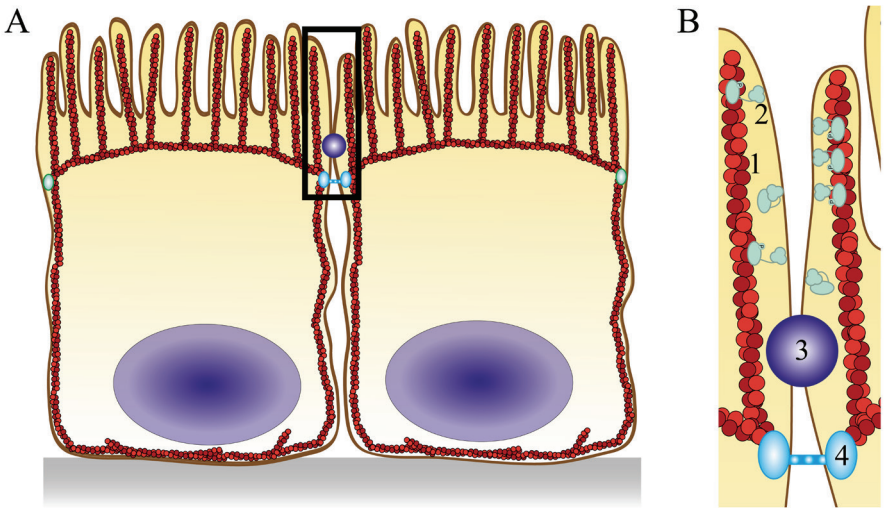

Figure 2.5: **Scheme of a *xz*-section of an epithelial cell. A: Two cells of a confluent cell monolayer. B: Zoom into the boxed region from A depicting important cellular structures for the mechanical behaviour of cells. (1) F-actin cytoskeleton, (2) actin-plasma membrane linker molecule ezrin, (3) tight juntions, (4) adherens junctions.**

2.7 Clathrin Mediated Endocytosis

The cellular plasma membrane is a very complex entity. By controlling the lipid bilayer composition, the cell communicates with the environment and controls different processes [91]. To regulate the plasma membrane composition and to enable an uptake of many different cargoes, different endocytosis pathways exist in different types of cells [92,93]. When electron microscopy became available in the 1960s, these internalisation processes were visualised for the first time [94,95]. One of the most important endocytosis pathways in epithelial cells is the clathrin mediated endocytosis (CME). It is used in all known eukaryotic cells. Clathrin mediated endocytosis can be divided into five stages. In the first steps, *initiation* and *cargo selection*, the cellular plasma membrane is slightly deformed, cargoes accumulate near the plasma membrane [96] and eventually bind to receptors. In order to form a pit (*coat assembly*), clathrin with its triskelia shape polymerises into pentagons and hexagons. There is no direct connection between the clathrin cage and the plasma membrane. Adaptor proteins and accessory proteins are necessary. After the pit is formed and fully caged, these proteins are recycled and can be reused by the cell. Dynamin assembles at the neck of the pit and pinches it off. The *scission* is supported by actin assembly at the pit. Then the pit is internalised (*internalisation*) and the clathrin cage is dismantled (*uncoating*). The cargo is sorted in endosomes.

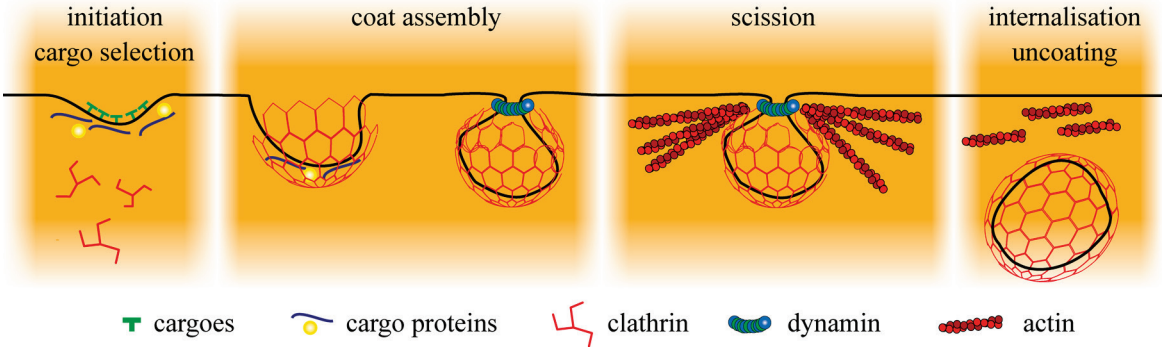

Figure 2.6: **Clathrin mediated endocytosis. After an initiation step, where the cargo is selected, a cage of polymerised clathrin supports the budding membrane invagination. Dynamin pinches the pit; scission occurs in an actin supported process. The pit is internalised, uncoated, and sorted.**

Endocytosis in general is a highly controlled process. Different signals can influence the endocytosis rate. Proteins out of the GTP-binding protein (G protein) class serve as molecular switches in cells. ADP ribosylation factors (ARF), members of the G protein family, regulate vesicular traffic in general [97,98]. For MDCK cells it has been figured out that GTP-bound ARF6 is involved in clathrin mediated endocytosis on both cell sides [99-102]. To study the internalisation process, there exist different chemical stimuli as well as genetic manipulations to arrest or enhance endocytosis rates [99,103,104]. Cells can be genetically modified to express a GTPase-defective mutant of ARF6. Thereby the endocytosis rate can be enhanced [99]. To block the clathrin-mediated endocytosis pathway different drugs are available. Those chemicals interfere with molecules which are necessary for a successful pit formation and maturation [103,104]. Prominent examples are Dynasore and Pitstop, which interfere with dynamin and the terminal domain of clathrin, respectively.

3 Techniques and Theory

3.1 Atomic Force Microscopy

In 1982 Gerd Binnig and Heinrich Rohrer invented the scanning probe microscopy by developing the raster tunnelling microscope [105]. In 1986 Binnig together with Quate and Gerber succeeded to map not only conductive surfaces but also insulating materials. The atomic force microscope (AFM) was developed [106,107].

In the early AFM technique a small, nanoscopic tip stays in contact with the sample. This tip is the end of a cantilever. An infrared laser beam, directed at the reflecting surface of this cantilever, is collected by a quadruple photo diode. The displacement of the cantilever is reflected in the deflection of the laser beam from the centre of the photo diode. This displacement in *x*- and *y*-direction can be calculated according to eqs. (3.1) and (3.2):

$$I_x = \frac{(I_B + I_D) - (I_A + I_C)}{I_{\text{total}}} \tag{3.1}$$

$$I_y = \frac{(I_A + I_B) - (I_C + I_D)}{I_{\text{total}}} \tag{3.2}$$

I_x and I_y are the current signals in these two dimensions. I_A, I_B, I_C and I_D describe the currents through the four different quadrants (Figure 3.1).

Today, the AFM technique is used in a wide field of different applications. Different probes with different rigidities and tip geometries are commonly available. To study topographical surface properties (imaging mode), the AFM can be used in three different operation modes: contact mode, where the tip stays in permanent contact with the sample, intermittent contact mode (tapping mode), where the tip oscillates and is only at the lowest oscillation point in contact with the surface and non-contact mode, where the tip oscillates without touching the surface. In contact mode the position of the cantilever can be kept constant, while scanning laterally across the surface (constant height) or the *z*-piezo, controlled by a feedback system, regulates the position of the tip to keep the force constant (constant force).

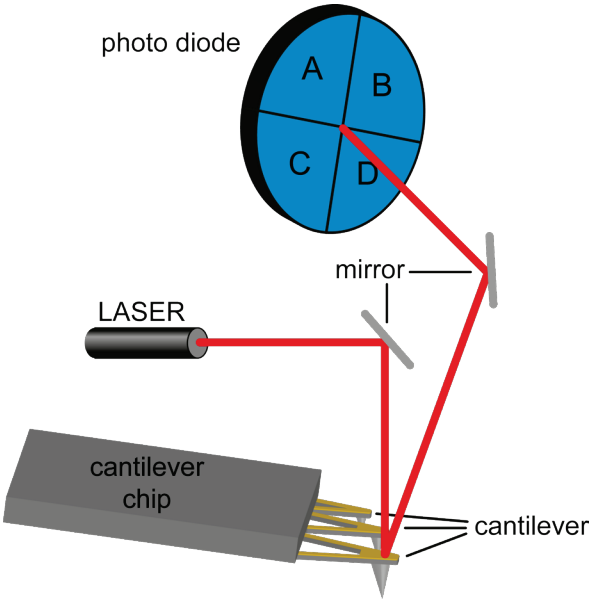

Figure 3.1: Scheme depicting the AFM principle. The vertically on the cantilever directed LASER beam is deflected and collected on a quadruple photo diode.

Furthermore, the atomic force microscope is widely used to determine mechanical properties. The probe is very small and the forces that can be applied to the sample are in an optimal range to determine the mechanics of biological samples, such as artificial membrane systems or cells [108,109].

The mechanical behaviour of the cantilever can be described by Hooke's law:

$$F = -k_c \cdot d_z \tag{3.3}$$

F is the force, k_c the spring constant of the cantilever and d_z describes the displacement of the leaf spring in z-direction.

The spring constant of a cantilever depends on the geometry of the tip. Thus, the exact spring constant of each probe has to be determined prior to the measurement. Besides calculations based on cantilever geometry or use of a reference cantilever, the thermal noise method is the standard technique for cantilever calibration, at least for soft cantilevers [8,110]. In this case thermal fluctuations of the environment are measured as a function of frequency. The greatest amplitude, located around the cantilever resonance frequency, is fitted by a Lorentz function. When the temperature is known, the amplitude only relies on the spring constant of the cantilever. Thus k_c can be calculated [110].

Prior to determination of the cantilever's spring constant, the sensitivity of the setup has to be determined. This value correlates the deflection of the tip with a defined movement of the laser on the photodiode. Thus, the signal, measured in volts, can be translated into forces [111,112].

3.2 Mechanical Models

3.2.1 Contact Models

Knowing the exact mechanical properties of the AFM cantilever enables one not only to image surfaces, but also to sense the mechanical response upon indentation of a specimen. The mechanical response can be recorded by indentation into the sample. The resolution is limited by the thermal noise in the deflection signal. The signal is often visualised in a *xy*-plot deflection against the height of the piezo. After the calibration process of the cantilever (see section 3.1), the deflection signal can be readily transformed into forces and distances between tip and sample (Figure 3.2). The tip is indented up to a default indentation force followed by an optional dwell time and retraction of the cantilever.

One of the simplest ways to describe the indentation is to apply continuum mechanics as proposed by Hertz or Sneddon:

$$F = r\frac{E}{\left(1-\nu\right)^2}\delta^j, \tag{3.4}$$

where ν is the Poisson ratio and *r* and *j* are parameters taking the geometrical properties of the indenter into account [113-115]. Examples for *r* and *j* are given in Table 3.1.

Table 3.1: Exemplary parameters *r* and *j* to account for different indenter geometries in eq. (3.4). θ: half-opening angle of the conical indenter. r_{sphere}: radius of the spherical indenter.

Indenter shape	*r*	*j*
cone	$\frac{2\tan(\theta)}{\pi}$	2
sphere	$\frac{4}{3}\sqrt{r_{sphere}}$	$\frac{3}{2}$

This approach leads to a Young's modulus *E*, which is defined as the tensile stress divided by the tensile strain. Since this theory is inherently restricted to small indentation depths, it fails to describe mechanical properties of biological samples such as cells. Nevertheless, this approach is widely used to study the mechanical behaviour of cells [116-118].

3.2.2 Tension Model

Classical approaches to describe the mechanical behaviour of cells, such as the Hertz model, fail to take the intricate architecture of the probed cell into account. The theory was worked out for two elastic bodies, which stay in contact. Furthermore, the calculated Young's modulus depends on the thickness of the probed specimen [119].

An alternative approach was reported by Pietuch *et al.* The liquid droplet model, which was first introduced theoretically by Sen and co-workers [10], enables access to more than one mechanical parameter of a biological cell. The model assumes an isotropic tension *T* originating from a pre-stress or overall tension t_0 of the membrane and the area dilatation or stretching of the membrane and underlying cortex upon deeper indentation. By using force balance and the Young-Laplace law, the isotropic tension can be written as

$$T = t_0 + K_A \frac{\Delta A}{A_0}, \tag{3.5}$$

where K_A is the area compressibility modulus and ΔA describes the area dilation with respect to the initial area A_0. Constant volume during indentation is assumed. Knowledge of the geometry of the non-deformed cell is necessary for adequate parameterisation to compute the shape of the indented cell at each indentation depth.

At small indentation depths t_0 might prevail (Figure 3.2). This pre-stress is dominated by an active cortical tension t_{act} of the actin cortex. In addition, a part originating from the membrane tension t_t contributes:

$$t_0 = t_{act} + t_t \tag{3.6}$$

Due to the liquid-crystalline structure of the membrane it is only extensible up to 2-3% [27]. Excess membrane material A_{ex} is stored in wrinkles and infoldings. This additional material can be used to accommodate deeper indentation of the cell with an AFM tip and prevents lysis of the plasma membrane. To take this effect into account, K_A is replaced by an apparent area compressibility modulus $\tilde{K}_A$:

$$\tilde{K}_A = K_A \frac{A_0}{A_0 + A_{ex}} \tag{3.7}$$

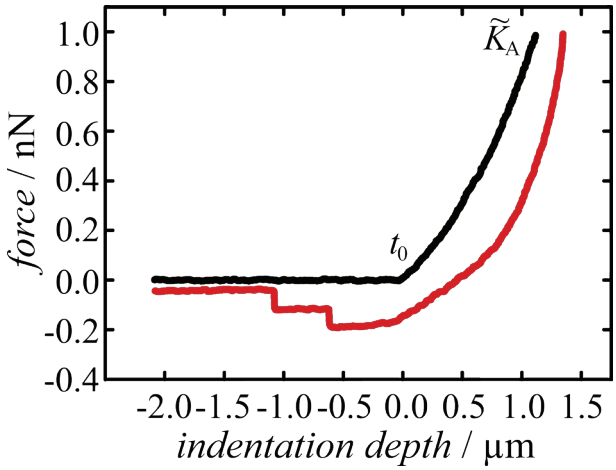

Figure 3.2: **Typical force-indentation cycle. The indentation curve is shown in black. Overall tension dominates the mechanical behaviour of a cell at low penetration, whereas area dilatation prevails at higher strain. The retraction curve is shown in red. Tether formation is reflected in specific steps (see chapter 3.3).**

3.3 Membrane Tether Formation

Indentation, however, is not the only way to probe the mechanical properties of biological samples. Pulling out small nanotubes provides further details of the mechanical behaviour of cells. Hochmuth described the first experiments of tether pulling out of red blood cells in 1982 [120]. Besides micropipette aspiration or magnetic or optical tweezers, membrane nanotubes can also be drawn out of a membrane using an atomic force microscope [121]. For this purpose, a strong binding between tip and membrane is necessary. Lectins are often used for tip functionalisation. They bind to specific sugars at the plasma membrane.

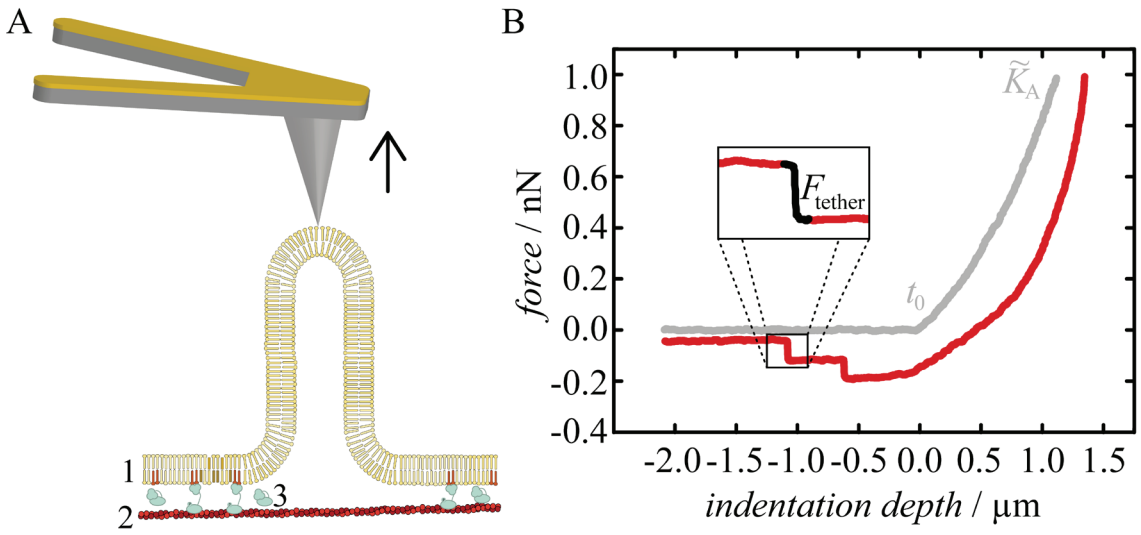

Figure 3.3: Membrane tether formation. A: The AFM tip strongly interacts with the plasma membrane. During retraction a membrane nanotube is pulled out. The plasma membrane (1) is connected to the underlying cytoskeleton (2) via linker proteins such as ezrin (3). This connection limits the tether formation. At a certain point a rupture occurs. B: Representative force-retraction curve (red), recorded with an AFM. Every tether rupture event is reflected in a force plateau with a specific tether rupture force F_{tether} (inset).

However, after indenting the membrane with a functionalised probe, a strong interaction between tip and sample occurs. During retraction, a small nanotube can be pulled out (Figure 3.3 A). This is reflected in a constant force in the force-distance curve. At a certain point the tether ruptures, resulting in a specific step in the force-distance curve (inset in Figure 3.3 B). The tether length and the rupture force

depend on the membrane material, from which the tether is formed. Thus, the membrane tension t_t is composed of the membrane's in-plane tension γ_m and the connection strength between plasma membrane and underlying cytoskeleton γ_{ad} [12]:

$$t_t = \gamma_m + \gamma_{ad} \tag{3.8}$$

The tether rupture force F_{tether}, measured at constant pulling velocity v_t can be written as [122,123]:

$$F_{tether} = 2\pi\sqrt{2\kappa \cdot t_t} + \frac{2\pi\eta v_t}{C}, \tag{3.9}$$

where η describes the membrane viscosity and C is a correction factor. A typical value used for cell membranes is $C = 1.6$ [120,123]. As an approximation, viscous contributions described by the second term can be neglected [122,124]. The bending rigidity κ depends on the amount of cholesterol in the membrane. When κ is known, the membrane tension can be calculated by

$$t_t = \frac{F_{tether}^2}{8\pi^2\kappa} \tag{3.10}$$

In the present study $\kappa = 2.7 \cdot 10^{-19}$ J is used to calculate the membrane tension. This is a typical value representing fluid lipid bilayers [30].

3.4 Electric Cell-Substrate Impedance Sensing

The electric cell-substrate impedance sensing (ECIS) technique is a powerful tool for monitoring morphological changes of cultured cells in real-time [125-127].

An alternate current (AC) between an ultra-small gold electrode (working electrode) and a counter electrode is applied. The scheme of an ECIS set-up is shown in Figure 3.4. The phase shift and the amplitude ratio between the input signal and a reference signal is determined by a lock-in amplifier and converted into the complex impedance Z at different frequencies. For an uncovered working electrode, the impedance spectra can be described as an Ohmic resistor R_{bulk} together with a constant phase element (CPE). Cells behave di-electric-like. Thus, coverage of the electrode is reflected in a frequency depending, increasing impedance.

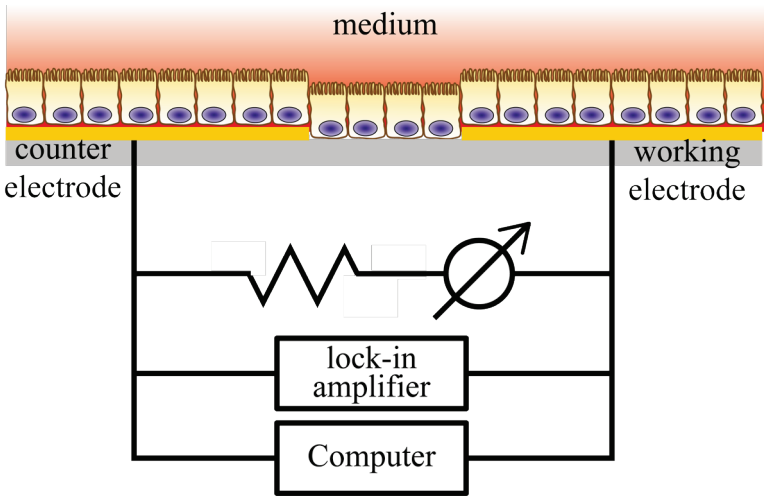

Figure 3.4: **Scheme depicting an ECIS setup. Between both electrodes an alternate current flows via the cell culture medium. The complex impedance *Z* is determined by measuring the phase shift and amplitude ratio between the input signal and a reference signal with a lock-in amplifier. When cells cover the electrodes, the impedance increases as a result of the decreasing current flow.**

The resulting frequency spectra can be divided into three regimes providing different information about the cellular morphology (Figure 3.5). At low frequencies ($\omega < 10{,}000\,\mathrm{Hz}$), the current uses the paracellular pathway to pass the cell barrier between working and counter electrode (Figure 3.5 A). It can be described as an Ohmic resistor R_b (Figure 3.5 B), reflecting the strength of the lateral connections

between the cells. Furthermore, the current passes the gap between cell and electrode (Figure 3.5 A). Contributions from this pathway can be modelled by a parameter α, which is a measure of cell-substrate distance *h*:

$$\alpha \propto \sqrt{\frac{1}{h}} \tag{3.11}$$

At higher frequencies ($\omega > 10{,}000\,\text{Hz}$), the impedance signal is dominated by the capacitance of the cellular plasma membrane C_m (Figure 3.5 C). The model, applied in this study, was first describe by Lo and co-workers [128,129].

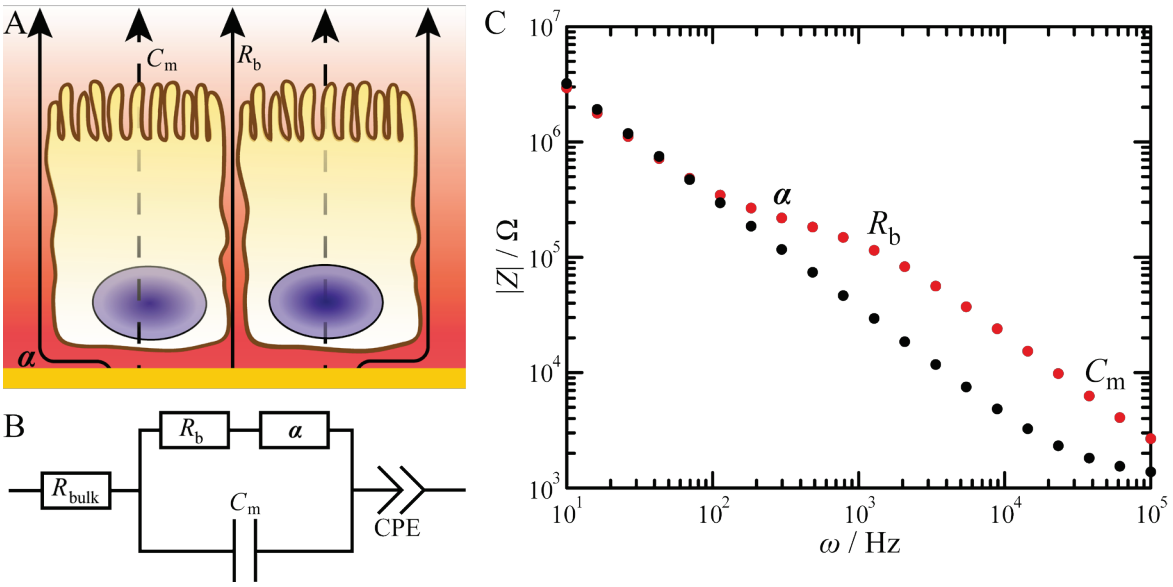

Figure 3.5: **A: Scheme depicting different pathways of the alternate current depending on its frequency. B: Equivalent circuit diagram for a cell-covered electrode of an ECIS set-up. C: Frequency spectra of an uncovered (black dots) and cell-covered (red dots) electrode. α and R_b can be calculated at lower frequencies. C_m is dominated by the high-frequency regime.**

3.5 RNA interference

Interference with the genetic machinery of a cell is a high-precision tool to block the expression of specific proteins. The protein biosynthesis takes place at the ribosomes. Messenger RNA (mRNA) released from the nucleus is read out and translated into an amino acid sequence. To analyse specific functions of proteins, it is possible to destroy the mRNA strand using small RNA fragments. This short interference RNA (siRNA) is commonly available for many different targets of different cell types. It can be inserted in the cell using techniques such as electroporation or lipofection. siRNA contains double stranded RNA fragments composed of 21-23 nucleotides. At the 3'-end of the fragment an overlap of 2-3 nucleotides was found. This end contains a free hydroxyl-group, whereas the 5'-end is phosphorylated [130,131]. In the cell the double stranded RNA is recognized by a dicer, which cuts it into a siRNA duplex [132,133]. Together with proteins, a RNA-inducing silencing complex (RISC) is formed. The RISC recognises the fitting target mRNA. By cleavage of the mRNA gene expression is blocked [134]. Figure 3.6 summarises the whole process.

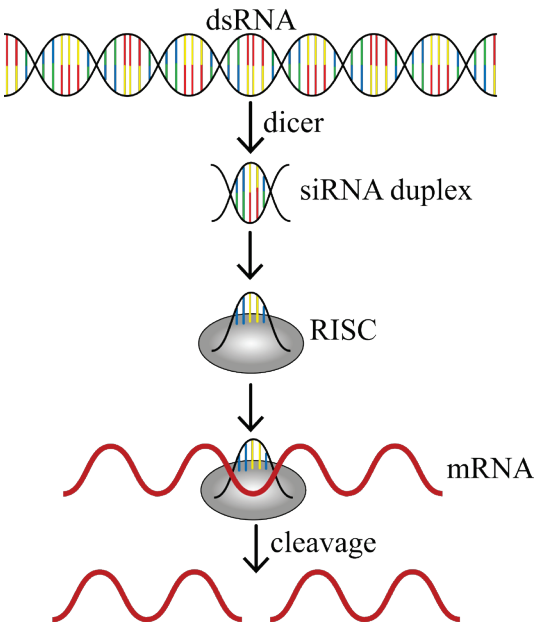

Figure 3.6: RNA interference by siRNA. Double stranded RNA is cut into siRNA duplexes. These duplexes form a RNA-inducing silencing complex (RISC). The RISC is directed to the fitting position at the mRNA strand. Cleavage takes place.

4 Material and Experimental Procedure

4.1 Buffers

The following table summarises all buffers used for the experiments.

Table 4.1: Composition and conditions of buffers used.

Buffer	Composition, Conditions
PBS^{--} (Phosphate buffered saline without Ca^{2+} and Mg^{2+})	8 g/L NaCl, 0.2 g/L KCl, 1.15 g/L Na_2HPO_4 in ultrapure water pH = 7.4
LB medium	10 g/L Tryptone/Peptone ex casein 5 g/L yeast extract 10 g/L NaCl
LB agar	10 g/L Tryptone/Peptone ex casein 5 g/L yeast extract 10 g/L NaCl 15 g/L agar 50 mg/L Kanamycin
PFA solution	4% (*w*/*v*) paraformaldehyde in PBS^{--} pH = 7.1
Blocking buffer	5% (*w*/*v*) bovine serum albumin (BSA), 0.3% (*v*/*v*) Triton X-100 in PBS^{--}
Dilution buffer	1% (*w*/*v*) bovine serum albumin (BSA), 0.3% (*v*/*v*) Triton X-100 in PBS^{--}
TBT buffer	10 mM Tris-HCl, 150 mM NaCl, 0.2% (*v*/*v*) Tween 20, 5% low fat dry milk in ultrapure water pH = 7.4
SDS-PAGE sample buffer (2x)	125 mM TRIS-HCl, 100 mM DTT, 20% (*v*/*v*) Glycerol, 2% (*v*/*v*) SDS, 0.02% (*w*/*v*) bromophenol blue in ultrapure water

4.2 Consumables

For cell culture all consumables were purchased from TPP, Trasadingen, Switzerland. As Petri dishes µ-Dish^{35mm}, low or µ-Dish$^{Grid-500}$ (ibidi, Martinsried, Germany) were used. All plastic products were tissue culture treated and pre-sterilized.

4.3 Cell Culture

Madine-Darby canine kidney cells (strain II, MDCK II; Health Protection Agency, Salisbury, UK) were maintained in minimum essential medium (MEM; Lonza, Verviers, Belgium) containing Earle's salts and 2.2 g/L $NaHCO_3$ supplemented with 4 mM L-glutamine and 10% fetal bovine serum (FBS; Biowest, Nuaillé, France) in a humidified incubator set to 37 °C and 5% CO_2. Cells were grown to confluency, released from culture flasks (25 cm^2 or 75 cm^2) using trypsin/EDTA (0.05%/0.02%; Biochrom, Berlin, Germany) and subcultered twice a week. During experimental procedure medium additionally contained penicillin (0.2 mg/mL; Biochrom, Berlin, Germany), streptomycin (0.2 mg/mL; Biochrom, Berlin, Germany), Amphotericin B (0.5 mg/mL; Biochrom, Berlin, Germany) and HEPES (15 µM; Biochrom, Berlin, Germany).

4.4 Microscopy Techniques

4.4.1 Phase Contrast Microscopy

Cells only slightly absorb light. Thus, it is not possible to visualize them using bright field microscopy. However, to make optically thin samples visible by means of light microscopy Frits Zernike developed phase contrast microscopy in 1932. This technique is based on the fact that not only the amplitude but also the phase of the light changes depending on the refractive index of the specimen passed by the light [135,136].

For phase contrast microscopy, an inverted light microscope (IX 81; Olympus, Tokyo, Japan) equipped with a 10X objective (UPLFLN 10X2PH, NA = 0.3; Olympus, Tokyo, Japan) and a 40X objective (LUCPLFKN 40XPH, NA = 0.6, Olympus, Tokyo, Japan) was used. The light source was a 100 W halogen lamp.

4.4.2 Fluorescence Microscopy

Fluorescence microscopy is widely used in cell research. Different proteins can be marked with different fluorescent dyes in one sample. Because of the arrangement of filters and dichroic mirrors only light of the desired wavelength is detected.

Epifluorescence microscopy was performed using an upright microscope (BX51; Olympus, Tokyo, Japan) equipped with two water immersion objectives (40X magnification: LUMPLFLN 40XW, NA = 0.8; 100X magnification: LUMPLFL 100XW, NA = 1.0; both Olympus, Tokyo, Japan) and the appropriate filter cubes to observe fluorescence dyes as indicated. A 120 W mercury-arc lamp (X-Cite 120Q; Lumen Dynamics Group, Ontario, Canada) served as light source.

For confocal fluorescence microscopy, a confocal laser scanning microscope (FluoView FV1200; Olympus, Tokyo, Japan) equipped with two oil immersion objectives (60X magnification: UPLFKN60XOIPH, NA = 0.65-1.25; 100X magnification: UPLFLN100XO2PH, NA = 1.3; both Olympus, Tokyo, Japan) and a 20X magnification objective (UCPLFLN20XPH, NA = 0.7; Olympus, Tokyo, Japan)

was used. Diode lasers with three different excitation wave lengths ($\lambda_{ex} = 405, 488$ or $561\,nm$) were applied.

Images were processed with software provided by the microscope manufacturer, with Bitplane Imaris, and with Adobe Photoshop.

4.4.3 Cell Labelling Technique

Cells were grown on Petri dishes, treated as desired and fixed by incubation with PFA solution for 20 min at room temperature. To permeabilise the cellular plasma membrane and to block unspecific binding sites, cells were treated with blocking buffer for 30 min at room temperature.

Direct labelling technique: The fluorescently labelled antibody was diluted with dilution buffer and the cells were incubated with this solution for 1 h at room temperature.

Indirect labelling technique: The primary antibody targeting the desired protein was diluted with dilution buffer. The cells were incubated with the antibody containing dilution buffer for 1 h. Afterwards the secondary antibody, binding to the primary, was diluted with dilution buffer and cells were incubated for 1 h at room temperature.

Nuclei staining: Cell nuclei staining was performed using 4',6-diamidino-2-phenylindole (DAPI). Cells were incubated with DAPI containing dilution buffer for 20 min at room temperature.

Between every labelling steps cells were rinsed three times with PBS^{--} on a vibratory plate (75 rpm) for 5 min each.

Plasma membrane staining: The plasma membrane of living MDCK II cells was stained using Cell Mask™ orange plasma membrane stain (Life Technologies, Carlsbad, USA). The dye was diluted 1:1000 with medium and the cells were incubated for 5 min at 37 °C. For green plasma membrane staining PFA-fixed cells were incubated with 4 µM PKH67 Green Fluorescent Cell Linker (Sigma-Aldrich, Steinheim, Germany) for 45 min.

All antibodies and labelling reagents are summarised in Table 4.2.

Table 4.2: Antibodies and reagents used for cell labelling.

Target	Reagent	Concentration
ezrin	Mouse anti-ezrin IgG1 (BD Biosciences, Heidelberg, Germany)	4 µg/mL
F-actin	Alexa Fluor 488- or Alexa Fluor 546- conjugated Phalloidin (Life Technologies, Carlsbad, USA)	165 nM
zonula occludens-1	Unconjugated or Alexa Fluor 488- conjugated mouse anti-ZO-1 (Thermo Fisher Scientific, Schwerte, Germany)	5 µg/mL
E-cadherin	Mouse anti-E-cadherin IgG_{2a} (BD Biosciences, Heidelberg, Germany)	5 µg/mL
Mouse IgG	Alexa Fluor 488- or Alexa Fluor 546-conjugated goat anti-mouse IgG (Life Technologies, Carlsbad, USA)	5 µg/mL
Nuclei	4',6-diamidino-2-phenylindole (DAPI) (Life Technologies, Carlsbad, USA)	50 ng/mL

4.4.4 Transferrin uptake assay

To analyse the clathrin-mediated endocytosis rate of MDCK II cells, cells were grown to confluence and cooled down to 0 °C for 10 min. Afterwards cells were washed three times with Life Cell Imaging Solution (Life Technologies, Carlsbad, USA) containing 1 % BSA and 20 mM glucose. The cells were incubated with Life Cell Imaging Solution (Life Technologies, Carlsbad, USA) containing 1 % BSA, 20 mM glucose and Alexa Fluor 546-conjugated transferrin (25 µg/mL; Life Technologies, Carlsbad, USA) in a humidified incubator set to 37 °C and 5% CO_2

for 15 min. Afterwards the cells were washed three times with pre-warmed Life Cell Imaging Solution (Life Technologies, Carlsbad, USA) containing 1 % BSA and 20 mM glucose and imaged in this medium by confocal fluorescence microscopy immediately.

4.5 Atomic Force Microscopy

4.5.1 Imaging Mode

Topographical images of cells were recorded with a Nanowizard® II or 3 AFM (JPK Instruments, Berlin, Germany). The AFM was mounted on an inverted microscope (IX 81, Olympus Tokyo, Japan) enabling phase contrast and fluorescence microscopy during AFM imaging. MDCK II cells were seeded onto Petri dishes and treated as desired. Prior to imaging cells were fixed using 2.5% Glutaraldehyde (GDA; Sigma-Aldrich, Steinheim, Germany) in PBS^{--} with an incubation time of 20 min. Samples were imaged in PBS^{--} at room temperature in contact mode. Silicon nitride cantilevers (MLCT; Bruker AFM Probes, Camarillo, USA) with a nominal spring constant of 10 mN/m were applied. The scan rate was 0.2 Hz. Images were processed using software provided by the AFM manufacturer.

4.5.2 AFM for Mechanical Measurements

All experiments were carried out using a Nanowizard® II or 3 AFM (JPK Instruments, Berlin, Germany) mounted on an inverted microscope (IX 81, Olympus, Tokyo, Japan). This enables one to determine the exact position for the indentation experiments. The force-indentation curves were recorded while scanning laterally across the sample, referred to as force mapping. Prior to the experiments, cantilevers (MLCT; Bruker AFM Probes, Camarillo, USA) were plasma cleaned (30 s Argon; Harrick Plasma, Ithaca, USA) and incubated with 2.5 mg/mL FITC-labelled Concanavalin A (Sigma-Aldrich, Steinheim, Germany) in PBS^{--} for 1.5 h. The exact spring constant of each cantilever used was determined by the thermal noise method [110]. The indentation and retraction speed was set to 2 µm/s. After indentation up to a maximal indentation force of 1 nN, a dwell time of 0.5 s was chosen before the cantilever was retracted.

Indentation curves were analysed by applying the tension model (see section 3.2.2). Tether rupture forces from the retraction curves were analysed as described in section 3.3. For each experiment at least eight cells were analysed.

4.6 Electric Cell-Substrate Impedance Sensing

Set-up. The ECIS measurements were performed with two different set-ups. The commonly available system was the Zθ set-up (Applied Biophysics, Troy, NY). Second, a homebuilt system was used, which consists out of a SR830 Lock-in amplifier (Stanford Research Systems, Sunnyvale, CA, USA) equipped with a SR550 pre-amplifier (Stanford Research Systems, Sunnyvale, CA, USA). The set-up was configured as a voltage divider with a constant Ohmic resistor R_1 (R_1 = 1 MΩ) and the measured complex impedance Z of the ECIS well. The reference output of the lock-in amplifier was used as voltage source. The resulting frequency dependent in- and out-of-phase voltages were measured by the lock-in amplifier and translated into the complex impedance Z of the ECIS well according to

$$Z = Z_{\mathrm{re}} + iZ_{\mathrm{im}} = \frac{U_{\mathrm{out}}/U_{\mathrm{in}} \cdot R}{1 - U_{\mathrm{out}}/U_{\mathrm{in}}}, \tag{4.1}$$

where $U_{\mathrm{out}} = 100\,\mathrm{mV}$ is the output voltage of the voltage source and U_{in} describes the measured in- and out-of-phase voltages. Different frequencies from 62.5 to 64,000 Hz for the Zθ set-up or from 10 to 100,000 Hz (homebuilt system) were measured. To switch between the different wells of the used 8W1E arrays (Applied Biophysics, Troy, NY) of the homebuilt set-up, an 8-channel USB-relay (K8090, Velleman, Gavere, Belgium) was used. A Matlab-software was used for data acquisition.

Measurements. The 8W1E electrode array (Applied Biophysics, Troy, NY) was placed in a 5% CO_2 humidified incubator set to 37 °C. 100 µL of cell culture medium were pipetted into each well. After incubation of the electrodes for 1 h with the medium, 200,000 cells suspended in 100 µL cell culture medium were added to each well and incubated until the cells reached confluence, reflected in a plateau of the impedance spectrum at approximately 4 kHz (approximately 25 hours). Afterwards, cells were treated as desired. After drug treatment, the medium was completely exchanged by pre-warmed cell culture medium to follow recovery of the cells.

4.7 Western Blotting

Cells were grown in 6-well plates to confluence, treated as desired and washed three times with PBS^{--}. Cell lysis was achieved by incubation with radioimmunoprecipitation (RIPA) buffer (Sigma-Aldrich, Steinheim, Germany) containing a protease inhibitor cocktail (cOmplete EDTA-free tablets; Roche Diagnostics, Mannheim, Germany) for 5 min at 0 °C. The cells were scraped from the wells and the lysate was centrifuged (8,000 x *g*, 4 °C) for 10 min. An adequate amount of the soluble fraction was diluted with SDS-PAGE buffer, shook for 5 min at 85 °C and 300 rpm and resolved by 17% SDS-PAGE. Proteins were electrophoretically transferred from the gel to a nitrocellulose membrane (supported nitrocellulose membrane 0.2 µm). The blot was blocked by incubation with TBT buffer for 1 h on a vibratory plate. The nitrocellulose membrane was incubated with the diluted primary antibody (ezrin mouse IgG1; BD Biosciences, Heidelberg, Germany; diluted to a concentration 500 ng/mL with TBT buffer) at 4 °C overnight. After washing the membrane with TBT buffer three times, it was incubated with the secondary antibody (horseradish peroxidase-conjugated goat anti-mouse IgG; Santa Cruz Biotechnology, Santa Cruz, USA; diluted to a concentration of 500 ng/mL with TBT buffer) at 4 °C for 1 h. Chemiluminescence was developed using Clarity™ Western ECL Substrate (Bio-Rad, Munich, Germany) and exposure to X-ray film.

4.8 Chemical Stimuli

4.8.1 Latrunculin A

Latrunculin A (Sigma-Aldrich, Steinheim, Germany) was dissolved in DMSO to prepare a stock solution with a drug concentration of 1 mM. For experimentation an appropriate amount of stock solution was diluted to a concentration of 1 µM with antibiotics and fungicide containing pre-warmed medium. The cells were incubated with the drug containing medium at 37 °C for the indicated period of time.

4.8.2 Jasplakinolide

Jasplakinolide (Enzo LifeSciences, New York, USA) was dissolved in DMSO to prepare a stock solution with a drug concentration of 1 mM. For experimentation an appropriate amount of stock solution was diluted to the desired concentration (0.5 µM or 1 µM) with antibiotics and fungicide containing pre-warmed medium. The cells were incubated with the drug containing medium at 37 °C for the indicated period of time.

4.8.3 NSC 668394

NSC 668394 (Merck Millipore, Molsheim, France) was dissolved in DMSO and diluted to a concentration of 250 µM with antibiotics and fungicide containing pre-warmed medium. The cells were incubated with the drug containing medium for 3 h at 37 °C.

4.8.4 Dynasore

Dynasore hydrate (Sigma-Aldrich, Steinheim, Germany) was dissolved in DMSO to prepare a stock solution with a dynasore concentration of 20 mM. For experimentation an appropriate amount of stock solution was diluted to a concentration of 100 µM with antibiotics and fungicide containing pre-warmed medium. The cells were incubated with the drug containing medium for 3 h at 37 °C.

4.8.5 Pitstop 2

Pitstop 2 (abcam, Cambridge, UK) was dissolved in DMSO to prepare a stock solution with a drug concentration of 30 mM. For experimentation an appropriate amount of stock solution was diluted to a concentration of 30 µM with antibiotics and fungicide containing pre-warmed medium. The cells were incubated with the drug containing medium for the indicated time at 37 °C.

4.8.6 DTT

1,4-Dithio-*D*-threitol (DTT; Sigma-Aldrich, Steinheim, Germany) was dissolved in cell culture medium to prepare a stock solution with a drug concentration of 1 M. For experimentation an appropriate amount of stock solution was diluted to a concentration of 10 mM with antibiotics and fungicide containing pre-warmed medium. The cells were incubated with the drug containing medium for the indicated time at 37 °C.

4.9 Gene Silencing

Cells were grown on Petri dished to 50% confluency. For ezrin silencing, pooled siRNA targeting ezrin sequences GCUVAAGAUAAUGCUAUGUU, GGCAACAGCUGGAAACAGAUU, GAAGAAGGCACCUGACUUUUU, and GAUCAGGUGGUAAAGACUAUU (siGENOME SMARTpool human EZR siRNA; Thermo Fisher Scientific, Lafayette, USA) were transfected using Lipofectamine® RNAiMAX transfection reagent (Life Technologies, Carlsbad, USA) according to the manufacturer's instructions. Measurements were performed 72 h after incubation with siRNA.

For tight junction protein 1 silencing, pooled siRNA targeting *zonula occludens-1* sequences GCAAAGACAUUGAUAGAAA, GAGAAGAAGUGACCAUAUU, CAAAAGAUCUGCAUCCUUA, and CCUGAACCAUGGUCGGAAA (siGENOME SMARTpool human EZR siRNA; GE Healthcare, Lafayette, USA) were transfected using Lipofectamine® RNAiMAX transfection reagent (Life Technologies, Carlsbad, USA) according to the manufacturer's instructions. Measurements were performed 72 h after incubation with siRNA.

For control measurements, non-targeting siRNA sequences UAAGGCUAU-GAAGAGAUAC, AUGUAUUGGCCUGUAUUAG, AUGAACGUGAAUUGCUCAA, UGGUUUACAUGUCGACUAA (siGENOME non-targeting siRNA Pool #2, GE Healthcare, Lafayette, USA) were applied using the same transfection reagent and time of incubation.

4.10 Plasmid Preparation

Plasmids were provided by Volker Gerke (ZMBE, University of Muenster, Germany). The sequence of either ARF6 wild type (ARF6-wt) or of a point-mutated ARF6 (ARF6-Q67L) was cloned into EcoRI and SalI sites of pEGFP-C1. The plasmid for the F-actin marker LifeAct (developed by Riedl *et al.* [137]) was provided by Volker Haucke (FMP, Berlin, Germany). One vial (100 µL) chemical competent *E. coli* cells (DH5α) were thawed on ice. A few microliters of the desired plasmid were added. The cells were incubated at 0 °C for 30 min. After heating the cells to 42 °C for 60 s, the suspension was incubated again at 0 °C for 5 min. 900 µL LB medium was added. The mixture was shaken (300 rpm) at 37 °C for 100 min followed by centrifugation (5,000 rpm, 45 s). After removing 600 µL of the supernatant, the remaining suspension was resuspended and scratched out on LB agar plates (50 µL each). The culture plates were incubated overnight at 37 °C.

For preparing a pre-culture a single colony was picked with a sterile pipet tip. The tip was added to 10 mL LB medium in a flask with baffles and shaken (250 rpm) overnight at 37 °C. For the main-culture 1 mL of the pre-culture was added to 100 mL LB medium in a flask with baffles and shaken (250 rpm) overnight at 37 °C. For plasmid isolation the NucleoBond Xtra Midi EF Kit (Macherey-Nagel, Dueren, Germany) was used, following the manufactures instructions. The resulting cDNA was verified by agarose gel electrophoresis and DNA sequencing.

4.11 Plasmid Transfection

In order to transfect cells with the desired plasmid, MDCK II cells were grown in cell culture flasks until approximately 75% confluence was reached. After releasing cells from culture flask and centrifugation, cells were resuspended in cold (4 °C) Opti-MEM reduced serum medium (Life Technologies, Carlsbad, USA) to a concentration of $2.5 \cdot 10^6$ cells/mL. 400 µL of this suspension were transferred into an ice-cold electroporation cuvette (gap: 4 mm). 5 µL of cDNA ($c \approx 50$ µg/mL) were added and mixed gently. The electroporation system consists out of a Gene Pulser Xcell (Bio-Rad Laboratories, Munich, Germany) including a ShockPod cuvette chamber (Bio-Rad Laboratories, Munich, Germany) and a CE module (Bio-Rad Laboratories, Munich, Germany) for electroporation of eukaryotic cells. Electroporation parameters: $U = 250$ V, $C = 950$ µF, $R = \infty$, exponential decay. Immediately after electroporation, cell suspension was transferred in an equal amount of pre-warmed complete cell culture medium containing 20% FCS and mixed gently. Cells were seeded onto Petri dishes and grown for 3 d to confluence in a humidified incubator set to 37 °C and 5% CO_2.

5 Results and Discussion

5.1 Mechanical Properties of MDCK II Cells

5.1.1 Introduction

Mechanical properties of cells can be described in a variety of ways [109]. In this section a brief introduction is given, how the mechanical behaviour of confluent epithelial cells is determined in the following chapters. AFM indentation followed by retraction of the indenter was used to analyse the mechanics of MDCK II cells. The mechanical response of the indented cell is reflected in force-indentation curves. A typical force-indentation cycle, recorded on a confluent MDCK II cell, is shown in Figure 3.2.

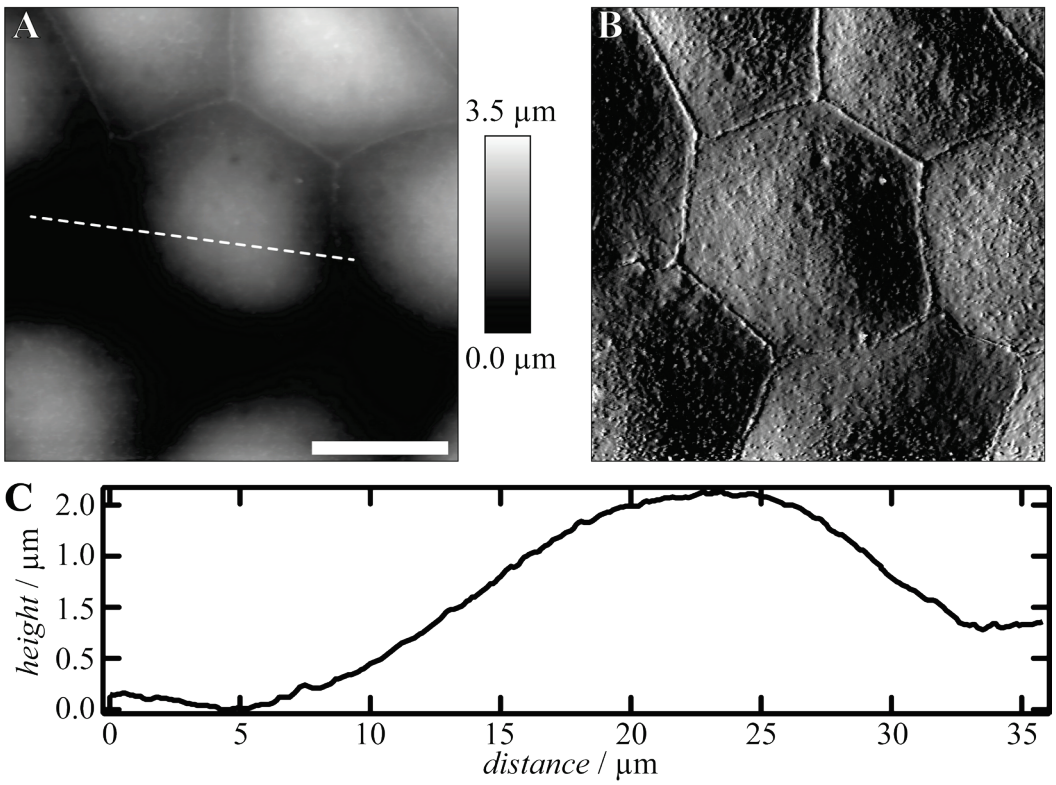

Figure 5.1: Topography of untreated MDCK II cells. A: AFM height image. B: Deflection image. C: Height profile along the white dotted line in A. Scale bar: 15 µm.

In order to quantify the mechanical properties of cells more precisely, the tension model, as described in section 3.2.2, was applied instead of Hertzian mechanics. This model highly relies on the geometry of the apical cell cap. Thus, untreated, fixed MDCK II cells were topographically mapped using AFM imaging in contact mode. Figure 5.1 shows a typical MDCK II cell. Additionally, the plasma membrane of a living MDCK II cell monolayer was fluorescently labelled. The apical cap was indented with an AFM tip at the centre and a confocal fluorescence image stack was recorded while the probe was indenting the cell (Figure 5.2).

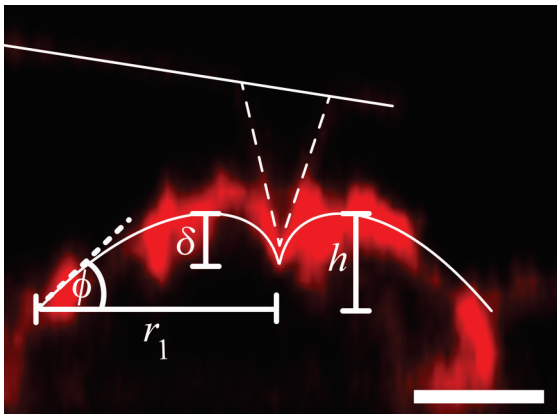

Figure 5.2: Confocal fluorescence image (*xz*-plane) of an indented MDCK II cell of a confluent cell monolayer. The plasma membrane is stained in red. The indenter is indicated by thin dashed lines. Important geometrical parameters are shown. *h*: Height of the apical cell cap. δ: Indentation depth. ϕ: spreading angle. r_1: base radius of the apical cap. Scale bar: 5 µm. Figure adapted from [32].

The base radius r_1 of the apical cap of untreated, confluent MDCK II cells was found to be approximately 13 µm. The height of this apex is approximately h = 2 µm.

According to

$$r_0 = \frac{r_1}{\sin(\phi)} \tag{5.1}$$

the base radius before spreading r_0 can be calculated from the base radius of the apical cell cap r_1. r_0 was determined to be 35 µm. To compute the apical cell cap during a virtual indentation, typical values of $t_0 = 0.3\,\text{mN/m}$ and $\tilde{K}_A = 0.2\,\text{N/m}$ were chosen. Different spreading angles ϕ were applied to the tension model in order to

simulate the apical cell cap. With a spreading angle of $\phi = 20°$ the shape of the simulated cap is in good agreement with the shape of the cell cap of MDCK II cells determined experimentally by AFM imaging. A cross section of a computed cell cap, indented by an AFM tip, is shown in Figure 5.3 A. Figure 5.3 B shows the calculated course of a force-indentation curve for the set of parameters mentioned above. Figure 5.3 C depicts a three-dimensional model of the indented cell cap. The results for computing the apical cap of MDCK II cells are in good agreement with the work of Pietuch *et al.* [12,13,18].

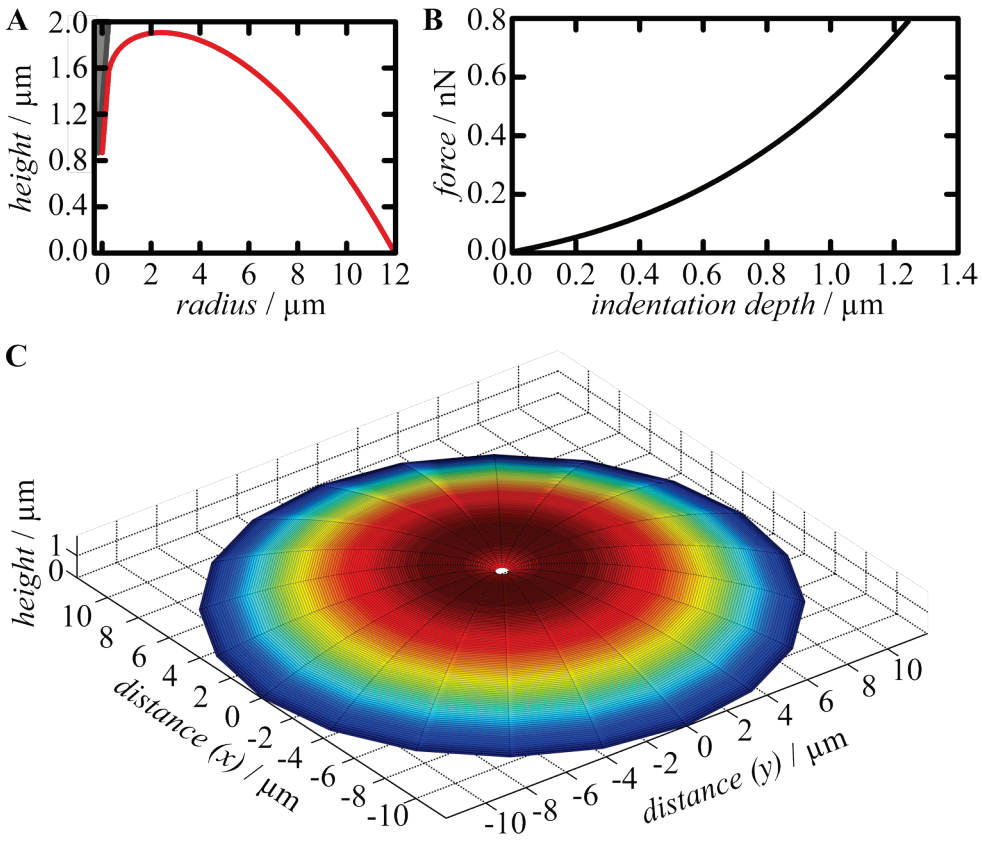

Figure 5.3: **Simulation of a cell cap based on the tension model. A: Cross section of the half of a cell (red), indented with an AFM probe (grey). B: Calculated force-indentation curve for a cell with an overall tension of 0.3 mN/m and an apparent area compressibility modulus of 0.2 N/m. C: Three-dimensional plot of the indented cell apex.**

5.1.2 Varying the Indenter Geometry – Proof of Principle for the Tension Model

Data processing was partly performed by Anna Pietuch. Results were published in Ref. [12]. Data and figures are reproduced or adapted from Ref. [12] with permission from The Royal Society of Chemistry.

The tension model was first described by Sen *et al.* [10]. Pietuch and co-workers developed the model and adapted it for epithelial cells [12]. Widely used and accepted models to describe the mechanical behaviour of cells often end up in only one parameter. As an example, calculation of the Young's modulus enables a quick comparison of the probed samples. However, the geometry of the cell and the active contractility of the shell-like architecture is usually ignored. Contact models provide a rather qualitative picture of cellular mechanics [115,138,139]. The Young's modulus, determined by the Hertzian contact model, might heavily rely on the geometry of the probe used for indentation [14]. Furthermore, the Hertz model is only valid for small indentation depths (up to a few hundred nanometres). Thus this model describes data recorded on biological cells insufficiently. It is known that the mechanical response to indentation is given by a pre-stress of the membrane and membrane area dilatation during deeper indentation.

In order to confirm the validity of the tension model and to demonstrate that this model captures the experimental data over the full indentation range independently from the indenter shape, two different indenter geometries, a pyramid (virtually indistinguishable from a cone) and a sphere with a size of 2 µm in diameter were indented into a cell. The centre of one and the same cell was indented with both probes. The resulting force distance curves are shown in Figure 5.4.

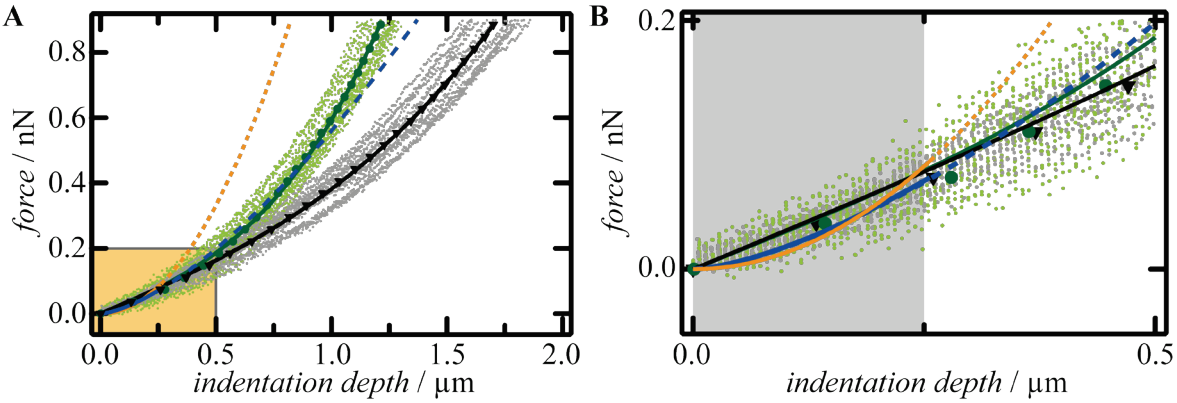

Figure 5.4: **Force-indentation curves recorded at the centre of a single MDCK II cell of a confluent cell monolayer. The cell was indented with either a pyramidal indenter (small grey dots) or a sphere (small green dots). The averaged curves are shown as black triangles (pyramid) or dark green circles (sphere). Averaged curves were subjected to the fitting procedure of the tension model (sphere: green line, pyramid: black line). The curve shape of the first 250 nm of indentation was either fitted by the Hertz model for the sphere (orange line) or the Sneddon model for the cone (blue line). A: Data for the full range of indentation. B: Zoom-in of the boxed region in A. The data used for the fitting of the Hertz or Sneddon model are highlighted in grey.**

The recorded curves were subjected to the fitting procedure of the tension model. For this purpose averaged indentation curves were calculated for both indenter shapes (Figure 5.4, cone: black triangles, sphere: green circles). The resulting fitted curves for the tension model are shown as solid black (pyramid) or solid green (sphere) lines. The averaged curves were also fitted using classical contact mechanics (Figure 5.4 B), according to eqs. (3.4), (5.2), and (5.3):

Cone:
$$F = \frac{2\tan\theta}{\pi}\frac{E}{(1-\nu)^2}\delta^2 \tag{5.2}$$

Sphere:
$$F = \frac{4}{3}\sqrt{r_{\text{sphere}}}\frac{E}{(1-\nu)^2}\delta^{3/2} \tag{5.3}$$

θ describes the half opening angle of the cone (θ = 17.5 °), which is virtually indistinguishable from a pyramid. δ is the indentation depth, the Poisson ratio ν was set to be 0.5, r_{sphere} describes the radius of the sphere (r_{sphere} = 1 µm), E is the

calculated Young's modulus. Here the fitting range was limited to a maximum indentation of 250 nm (Figure 5.4, blue curve (cone), orange curve (sphere)).

The best fitting curves of the applied models demonstrate that the classical approaches fail to satisfactorily describe the recorded curves. In the first 250 nm of indentation the model curve does not represent the measured force-indentation shape (Figure 5.4 B). In contrast, the tension model fits the curves over the full indention way very well. The mechanical parameters obtained from the two different theoretical approaches were calculated. The results are summarised in Table 5.1.

Table 5.1: Results (median ± SEM) of fitting Hertzian mechanics or the tension model to the averaged force-indentation curves shown in Figure 5.4.

Indenter	E / Pa	t_0 / mN/m	$\tilde{K}_A$ / N/m
Pyramid (cone)	1727.1 ± 66.8	0.37 ± 0.04	0.050 ± 0.001
Sphere	105.2 ± 2.0	0.14 ± 0.02	0.05 ± 0.01

The results of either applying the Hertz or the Sneddon model differ by one order of magnitude depending on the indenter geometry. The tension model delivers consistent data, almost independent of the geometry of the indenter. Only the overall tension is smaller by a factor of 2 for the sphere.

5.1.3 Discussion

In this section, the validity of the tension model was reviewed. The tension model is the basis for the analysis of all following indentation experiments. Here it was shown that the model reproduces the experimental data over the full indentation range. Moreover, it captures the intricate shell-like architecture of an epithelial cell and is almost independent of the indenter shape. Differences in the overall tension might be attributed to a stronger adhesion of the cell to the larger indenter due to a larger contact area or to insufficiently captured bending of the cortex. Upon deeper indentation, the mechanical behaviour described by the apparent area

compressibility modulus was found to be the same. Contact models, such as Hertz and Sneddon are incapable of reproducing the experimental data of a force-indentation cycle, especially at high strain. It is particularly alarming that variations of the Young's modulus were found, when the indenter geometry was altered. These models are appropriate to describe mechanics of semi-infinite elastic bodies at low indentation depths. They fail, however, for the interpretation of shell-like structures in cells, where the plasma membrane is connected to the underlying cell cortex. Bending of the order of a few $k_B T$ prevails at low strain in the absence of pre-stress, whereas area dilatation dominates the cellular response to higher indentation forces. Thus, the tension model, which captures low to high strain, is a better suited model to describe the mechanical behaviour of epithelial cells, at least for MDCK II cells.

5.2 The Impact of the Cytoskeleton

Experiments and data processing described in this section were partly performed by Mark Skamrahl during his Bachelor's thesis.

An intact cytoskeleton is essential for the mechanical integrity of cells. The interplay between F-actin and other proteins, such as membrane linker molecules of inner cellular compartments, is essential for the stability and fundamental functions of cells. In this study, the focus is set on the actin cytoskeleton. Depolymerisation on the one hand and an enhanced polymerisation on the other hand was achieved by administration of different drugs.

5.2.1 Destroying Cortical Integrity

In order to depolymerise F-actin bundles, Latrunculin A was used. This drug binds in a one-to-one stoichiometry to globular actin hindering the polymerisation process [140]. The depolymerisation process, however, remains unaffected. Thus, depolymerisation of the F-actin cytoskeleton is achieved within 1 h (Figure 5.5).

After treatment of MDCK II cells with 1µM Latrunculin A for 30 min, the F-actin distribution is already tremendously altered. On the apical side, small point-like structures representing microvilli disappear. They are replaced by bulky dots. The contractile ring is dissolved (Figure 5.5 A1, A2). After 60 min of incubation with the drug, no further significant alterations become visible. A coarser structure, interpreted as F-actin fragments can still be observed (Figure 5.5 A3). Co-localisation analysis of ezrin with actin still shows a strong correlation on the apical side of the cell. As soon as the drug interferes with the cytoskeleton, the ezrin distribution is impaired as well. Small but sharp and clearly distinguishable structures in the ezrin signal disappear. Already after 30 min of incubation only blurry structures can be observed (Figure 5.5 B1-B3).

For control cells in the central focal plane of a MDCK II cell monolayer, a strong F-actin belt is visible. After adding the drug, this belt is destroyed. A few bulky F-actin fragments remain. Even after 60 min of incubation these residues are still visible

(Figure 5.5 C1-C3). For control cells only a slight ezrin signal was found in this cellular region. Activated ezrin can only be found on the apical side, where the binding partner PIP_2 is present in the plasma membrane. Interestingly, however, after F-actin depolymerisation some ezrin was found in the central region of the cell (Figure 5.5 D1-D3).

In fully polarised epithelial cells, stress fibres are formed at the basal cell side. Latrunculin A not only destroys the F-actin located at the apical cell side and at the cell-cell contacts, but also depolymerises stress fibres at the basal side. Only a few small dots remain after Latrunculin A treatment. There is just a small difference between the signals recorded after 30 min and after 60 min of incubation (Figure 5.5 E1-E3). Remaining dots are smaller after 30 min of incubation compared to those found after an incubation time of 60 min. No ezrin can be found in control cells on the basal side. In contrast, after 60 min of drug treatment, there is a very small ezrin signal (Figure 5.5 F1-F3).

These findings are in good agreement with the results from AFM imaging experiments (Figure 5.6). For untreated cells, point-like structures are found on the apical cell side. These structures represent the microvilli, membrane protrusions filled with F-actin bundles, which appear in confocal fluorescence images of the apical cell side as sharp point-like structures. The cell-cell boundaries appear as a solid wall surrounding each cell (Figure 5.6 A). After incubation of the cells with 1 µM Latrunculin A for 30 min, the topographical properties are altered. As already found by fluorescence microscopy, the microvillar structures agglomerate into bigger clusters. The contractile ring supporting the cell-cell boundaries is fragmented (Figure 5.6 B). There is no significant difference between the topographical appearance of the cells after 30 min and 60 min of incubation, respectively.

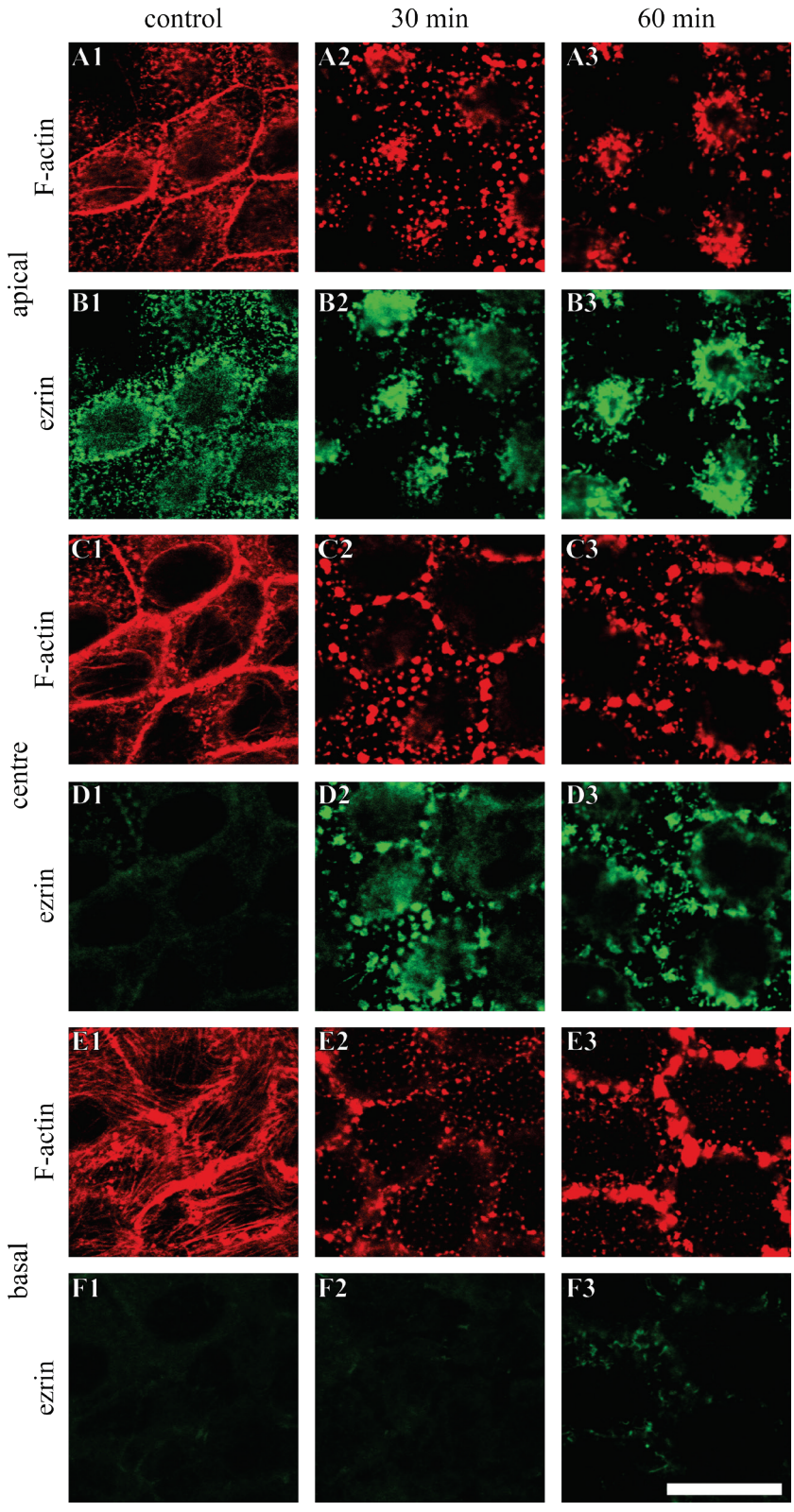

Figure 5.5: **The effect of Latrunculin A on MDCK II cells. Confocal micrographs show the F-actin distribution (A, C, E) and ezrin distribution (B, D, F) for control cells (1), after 30 min of exposure to 1 µM Latrunculin A (2), and after treatment for 60 min (3). The apical side is shown in (A) and (B), and centre in (C) and (D), while (E) and (F) depict the basal side. Scale bar: 20 µm.**

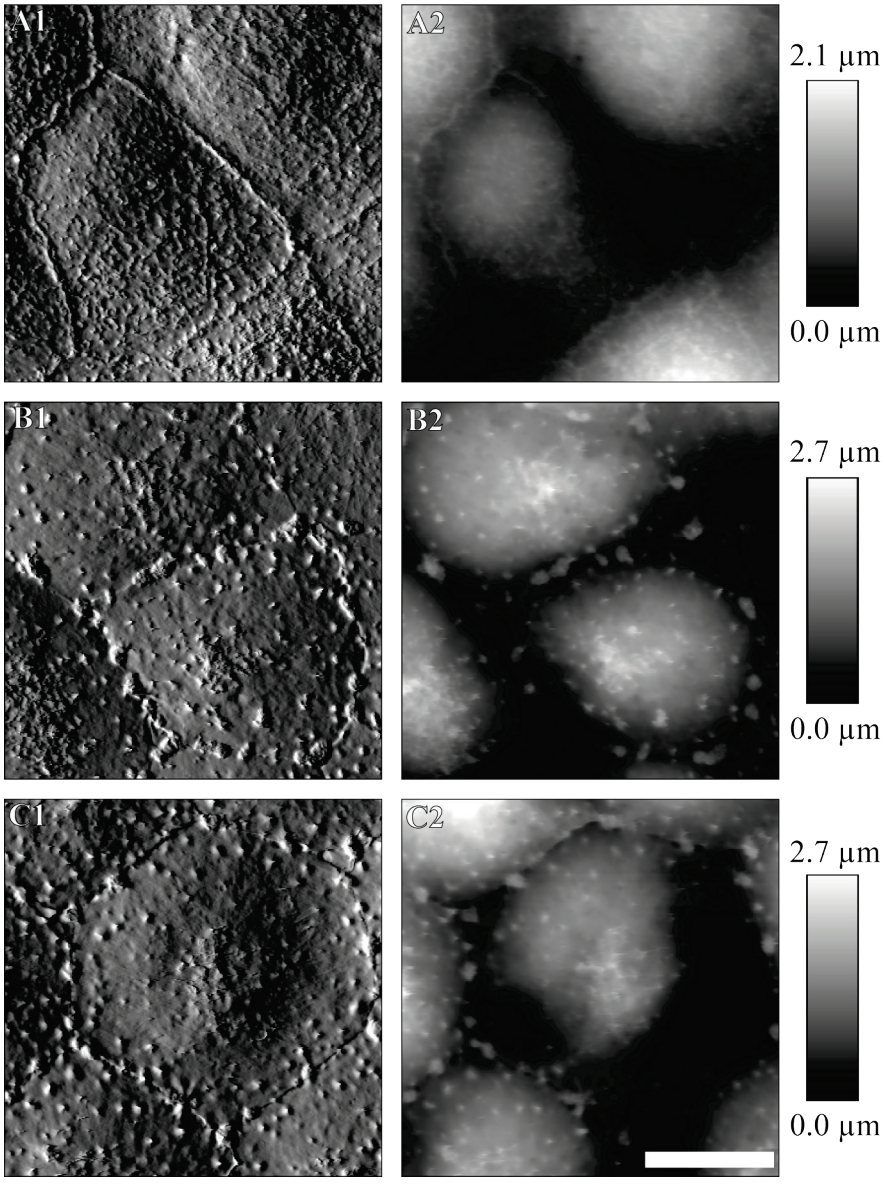

Figure 5.6: Topographical investigation of the effect of Latrunculin A on MDCK II cells. A: Untreated cells. B: Cells after 30 min of 1 µM Latrunculin A administration. C: Cells exposed to 1 µM Latrunculin A for 60 min. 1: AFM deflection images. 2: AFM height images. Cells were fixed with 2.5% GDA before imaging in contact mode. Scale bar: 10 µm.

In order to investigate changes of the cell-substrate distance, the membrane capacitance and the cell-cell junctions, electric cell-substrate impedance sensing (ECIS) was used to analyse the impact of Latrunculin A on MDCK II cells in real-time. The impedance signal shows a strong drop immediately after drug-addition (Figure 5.7 A, incubation time marked in grey). This drop ceased within 2 h after removing the drug from the cell culture medium. A drop in the membrane capacity

C_m (Figure 5.7 B) reveals a reduced membrane surface area during drug treatment, which can be largely restored within less than 30 min after removing the drug. The barrier resistance R_b is a measure of the binding strength between the cells in the monolayer, mainly given by tight junction formation. R_b also drops immediately after exposing MDCK II cells to Latrunculin A (Figure 5.7 C). It takes more than 6 h to restore the initial cell state of a confluent layer. The cell-substrate distance increases due to Latrunculin A treatment (lowered α, Figure 5.7 D). The full attachment can be restored within 4-5 h after drug removal.

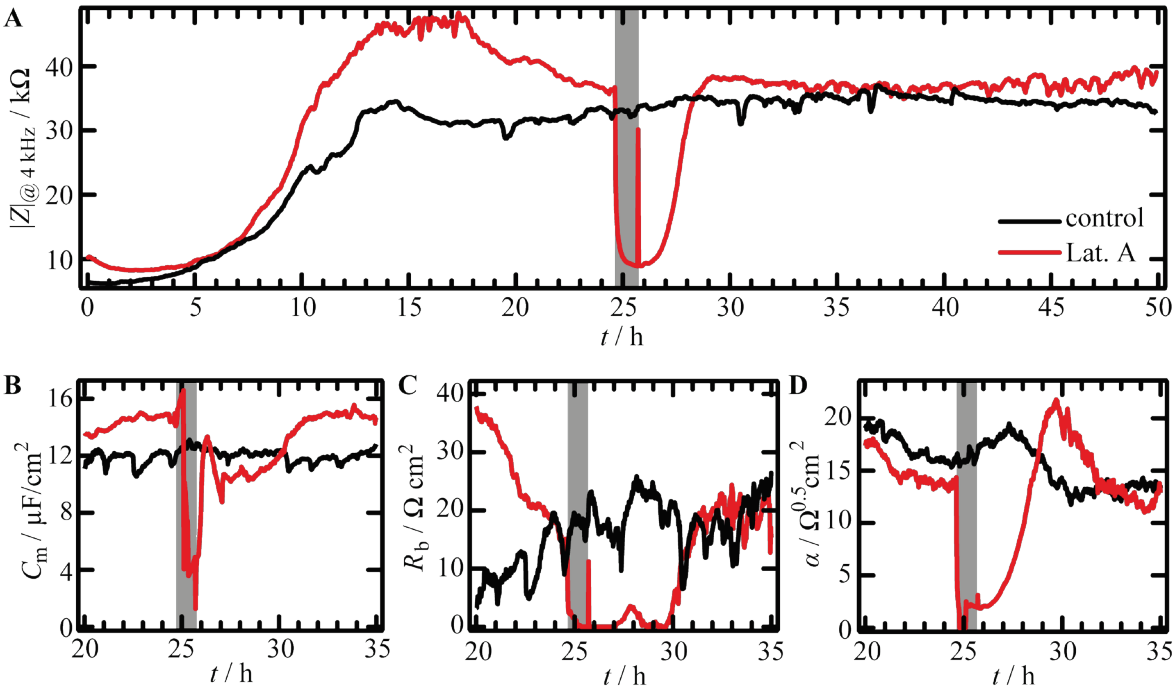

Figure 5.7: ECIS measurements of MDCK II cells treated with 1 µM Latrunculin A for 1 h. A: Impedance spectra recorded at 4,000 Hz. B: Membrane capacitance C_m. C: Barrier resistance R_b. D: Parameter α describing the cells-surface distance. Black spectra represent untreated cells; red ones show the behaviour of cells treated with 1 µM Latrunculin A. The incubation time starting 25 h after seeding the cells on the electrode is highlighted in grey (1 h).

After interfering with the cortical integrity, the cells substantially soften. This can already be observed in the curve shape of recorded force-indentation curves. The slope is weaker for cells treated with 1 µM Latrunculin A for 30 min. After 60 min of incubation the effect is even more pronounced (Figure 5.8).

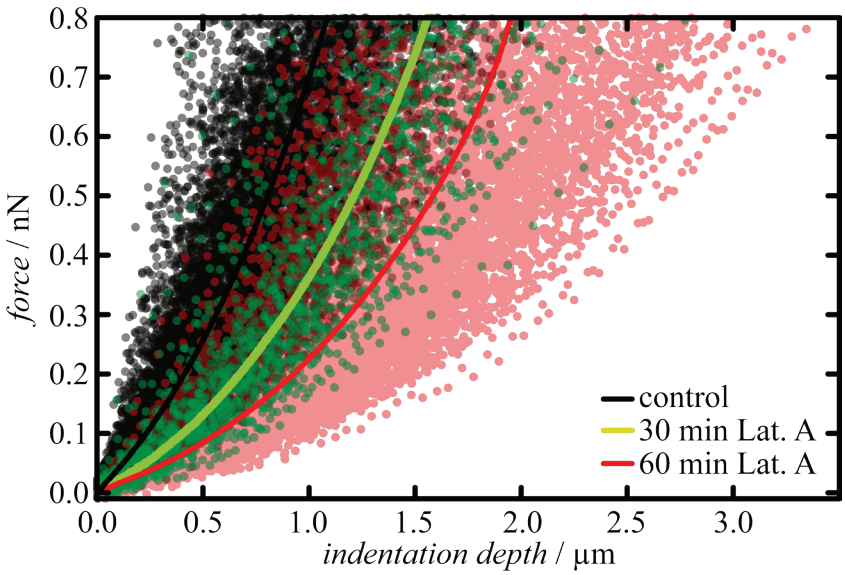

Figure 5.8: **Force-indentation curves recorded on MDCK II cells. The averaged curve is shown for untreated cells in black, for cells treated with 1 µm Latrunculin A for 30 min in green and for an incubation time of 60 min in red. The semi-transparent dots in corresponding colour represent the original data recorded on cells with different treatments.**

The overall tension drops from $t_0 = (0.60 \pm 0.02)$ mN/m (control; median ± SEM) to $t_0 = (0.28 \pm 0.02)$ mN/m after 30 min of Latrunculin A administration. After 60 min of drug treatment, the overall tension is even lower ($t_0 = (0.175 \pm 0.004)$ mN/m). The distribution becomes narrower (Figure 5.9 A). The apparent area compressibility modulus, which is inversely proportional to the excess membrane surface, was found to be $\tilde{K}_A = (0.157 \pm 0.007)$ N/m for untreated cells. After treatment with 1 µM Latrunculin A for 30 min $\tilde{K}_A$ drops to (0.09 ± 0.01) N/m. After additional 30 min of incubation it was found to be $\tilde{K}_A = (0.051 \pm 0.003)$ N/m (Figure 5.9 B).

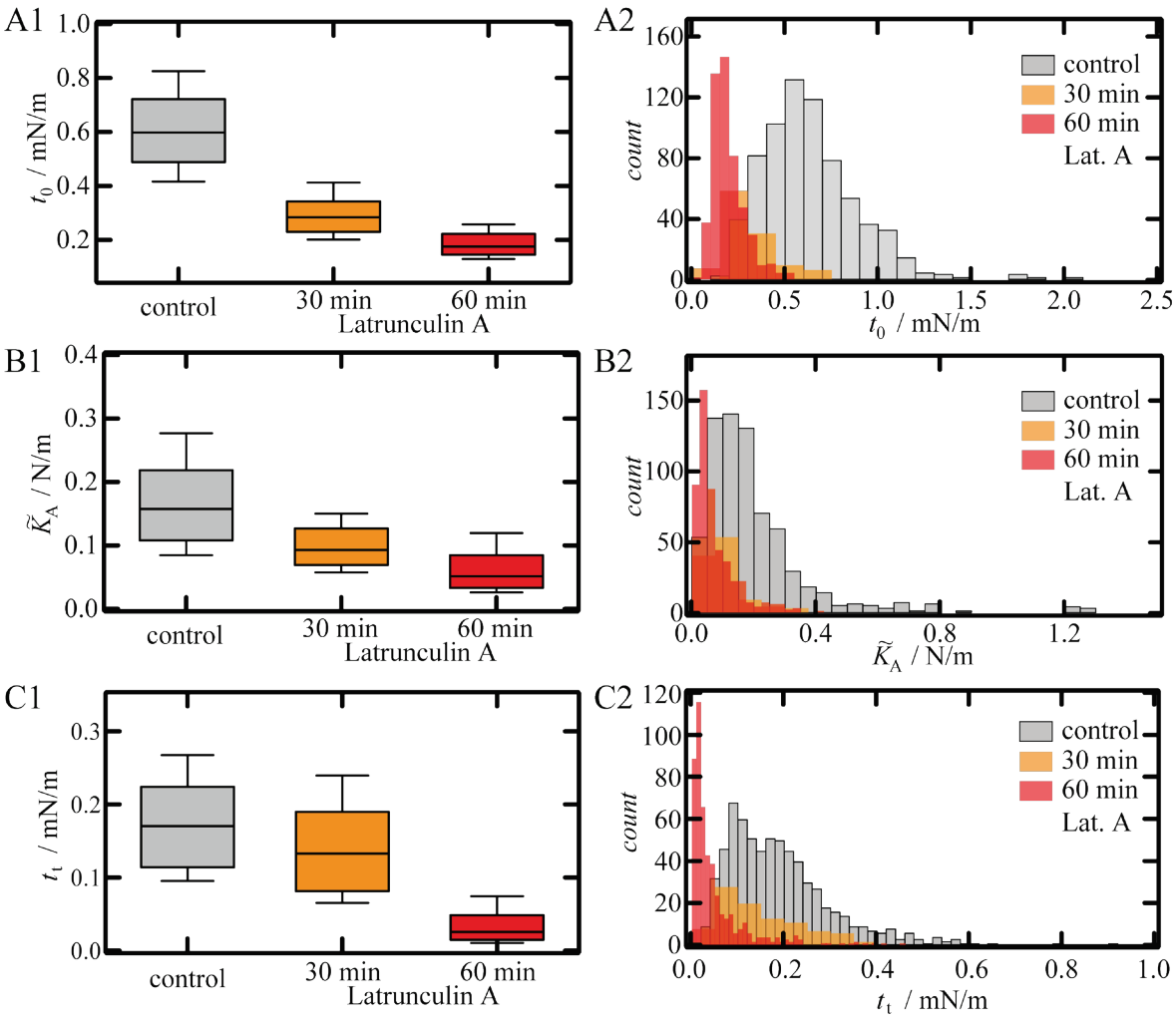

Figure 5.9: **Mechanical properties of MDCK II cells exposed to 1 µM Latrunculin A. A1: Box plot for the overall tension t_0. A2: Corresponding histogram. B1: Box plot showing the apparent area compressibility modulus $\tilde{K}_A$. B2: Histogram corresponding to B1. C1: Box plot for membrane tension t_t. C2: Histogram corresponding to C1. Grey boxes and bars represent values for untreated cells, orange ones after 30 min, red ones after 60 min of 1 µM Latrunculin A administration. Box plots extend from the 30th to the 70th percentile, whiskers from the 20th to the 80th. A: $n = 720$ (control), 118 (30 min Lat. A), 515 (60 min Lat. A) analysed force-indentation curves. B: $n = 713$ (control), 118 (30 min Lat. A), 512 (60 min Lat. A) analysed force-indentation curves. C: $n = 668$ (control), 95 (30 min Lat. A), 497 (60 min Lat. A) force-retraction curves.**

The membrane tension, a measure of membrane-cytoskeleton attachment according to eq. (3.8), drops from $t_t = (0.170 \pm 0.005)$ mN/m (control) to $t_t = (0.133 \pm 0.009)$ mN/m after 30 min of drug treatment. After 60 min Latrunculin A administration t_t is further reduced ($t_t = (0.025 \pm 0.002)$ mN/m).

Apart from membrane tension, a part of the overall tension originates from the active contraction of the cortex. Referring to eq. (3.6), t_{act} drops from $t_{act} = 0.43\,\text{mN/m}$ to 0.15 mN/m within 30 min of Latrunculin A administration. Further incubation with the drug has no impact on this tension. It was found to be $t_{act} = 0.15\,\text{mN/m}$ after 60 min of exposure of the cells to Latrunculin A.

5.2.2 Reinforcement of the Actin Cytoskeleton

After the investigation of the impact of a destroyed F-actin cytoskeleton on the mechanical behaviour of MDCK II cells, the reverse effect was studied. To induce actin filament nucleation and to stabilise F-actin bundles, Jasplakinolide, a drug found in the marine sponge *Jaspis johnstoni*, was used [141,142]. As a first approach, MDCK II cells expressing GFP-tagged actin were used to study the impact of Jasplakinolide in real-time (Figure 5.10). Here, confocal fluorescence microscopy was combined with phase contrast microscopy. Untreated GFP-tagged actin expressing cells show a normal actin distribution, as known from fluorescence experiments using non-transfected MDCK II cells stained with fluorescently labelled phalloidin. After incubation for 30 min with 1 µM Jasplakinolide, the cells start to round off (Figure 5.10 B1). The actin distribution is altered and small dots found in the fluorescence images before drug treatment, which represent microvillis on the surface, appear as bigger dots (Figure 5.10 B2). After an exposure time of 45 min to the drug, the cells are rounded off even more and gaps between cells become visible (Figure 5.10 C1). The actin cytoskeleton forms a ring-like structure surrounding the cell nucleus (Figure 5.10 C2). These effects become more and more pronounced over time. After an incubation time of 300 min, the formerly spread and contact inhibited confluent cells exist only as spheres surrounded by an actin shell (Figure 5.10 F).

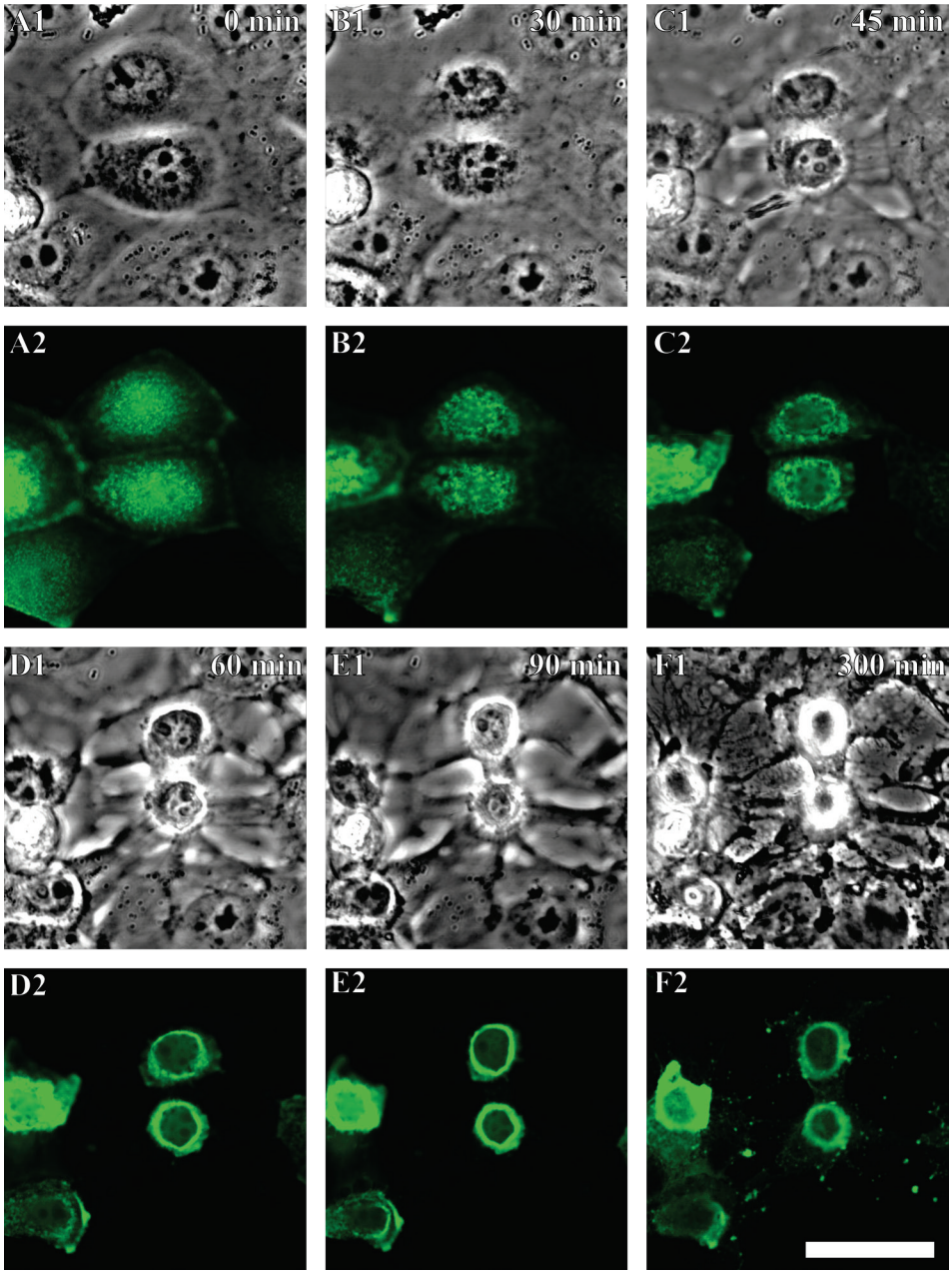

Figure 5.10: Jasplakinolide alters the morphology and F-actin distribution of MDCK II cells. 1: Phase contrast images. 2: Confocal fluorescence images of GFP-tagged F-actin expressing cells corresponding to the region shown in 1. The pictures were taken before (A) and after 30 min (B), 45 min (C), 60 min (D), 90 min (E), and 300 min (F) of incubation of the cells with 1 µM Jasplakinolide. Scale bar: 30 µm.

However, genetic manipulations of cells prior to drug stimuli can interfere with the drugs applied. To avoid this crosstalk, non-transfected MDCK II cells were exposed to Jasplakinolide, fixed with PFA solution after several periods of incubation and stained for fluorescence microscopy afterwards (Figure 5.11). Here the effect of

Jasplakinolide was not as strong as found for GFP-tagged actin expressing cells. After 30 min of incubation with 1 µM Jasplakinolide of non-transfected cells, small dots representing microvillis on the apical cell side vanish (Figure 5.11 A2). More clustered F-actin formations were found. The F-actin shell fencing the cell in the central focal plane becomes impaired (Figure 5.11 C2). Stress fibres on the basal side seem to be unaffected at this time (Figure 5.11 E2). Ezrin is only slightly affected by the drug treatment (Figure 5.11 B2, D2, F2). A small amount of ezrin becomes visible on the basal side. When the cells were incubated for 60 min, F-actin formed a solid cap on the apical side. Moreover, the ezrin distribution is more clustered. In the central focal plane, the actin ring is impaired. A solid surrounding disappears. On the basal side, there are still some stress fibres. However, the overall amount is reduced compared to untreated cells. Ezrin cannot be found in the central and basal plane (Figure 5.11 A3-F3).

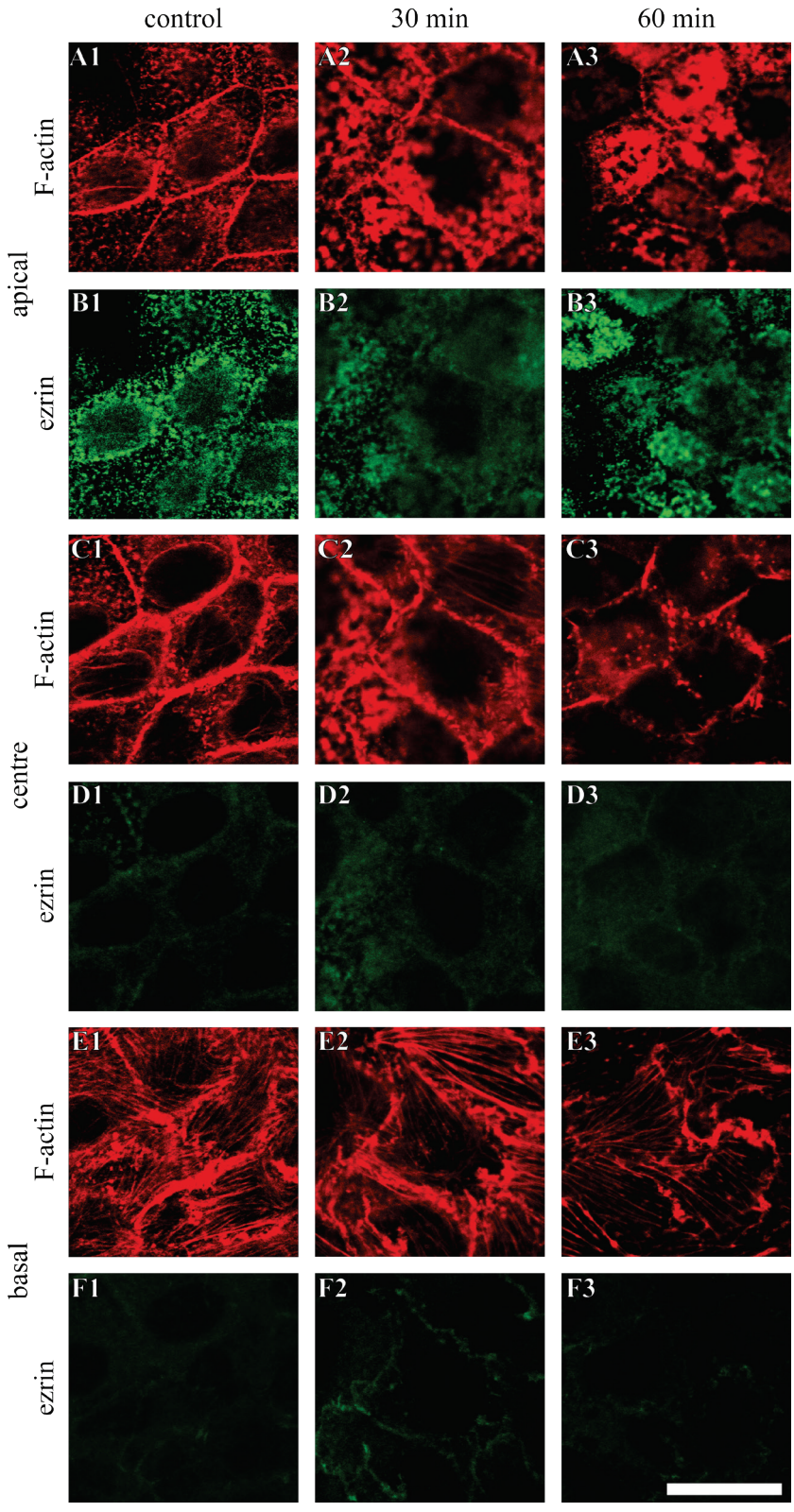

Figure 5.11: **The impact of Jasplakinolide on MDCK II cells. Confocal micrographs show the F-actin distribution (A, C, E) and ezrin distribution (B, D, F) for control cells (1), after 30 min of exposure to 1 µM Jasplakinolide (2), and after drug treatment for 60 min (3). The apical side is shown in (A) and (B), and the centre in (C) and (D). (E) and (F) depict the basal side. Scale bar: 20 µm.**

As a result, it appeared increasingly likely that F-actin is diminished at the bottom of the cell and concentrates at the upper cell side. To get a deeper insight of the actin distribution, three-dimensional confocal images were recorded (Figure 5.12). It became clear that F-actin is enriched at the apical side of the cell. Moreover, the cells seem to be contracted and the apical cap has a reduced height.

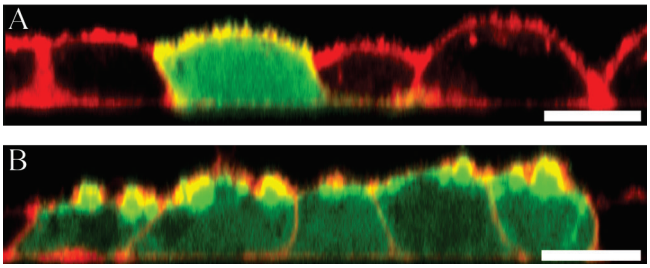

Figure 5.12: Confocal fluorescence micrographs (*xz*-plane) of confluent MDCK II cells. Some cells express GFP-tagged actin (green). The plasma membrane was stained with cell mask™ orange (red). A: Control cells. B: Cells exposed to 0.5 µM Jasplakinolide for 1 h prior to fixation. Scale bar: 10 µm.

The topographical properties of the cells were examined using AFM imaging of GDA fixed cells in contact mode. Already after 30 min of Jasplakinolide treatment, the contractile ring surrounding the cells disappears. Instead of microvilli there are bigger buckles on the cell surface (Figure 5.13 A, B). This might be attributed to the bigger actin agglomerates on the apical side found in fluorescence micrographs. After another 30 min of exposure time, the buckles have further increased in size. The rest of the cell surface is flattened (Figure 5.13 C).

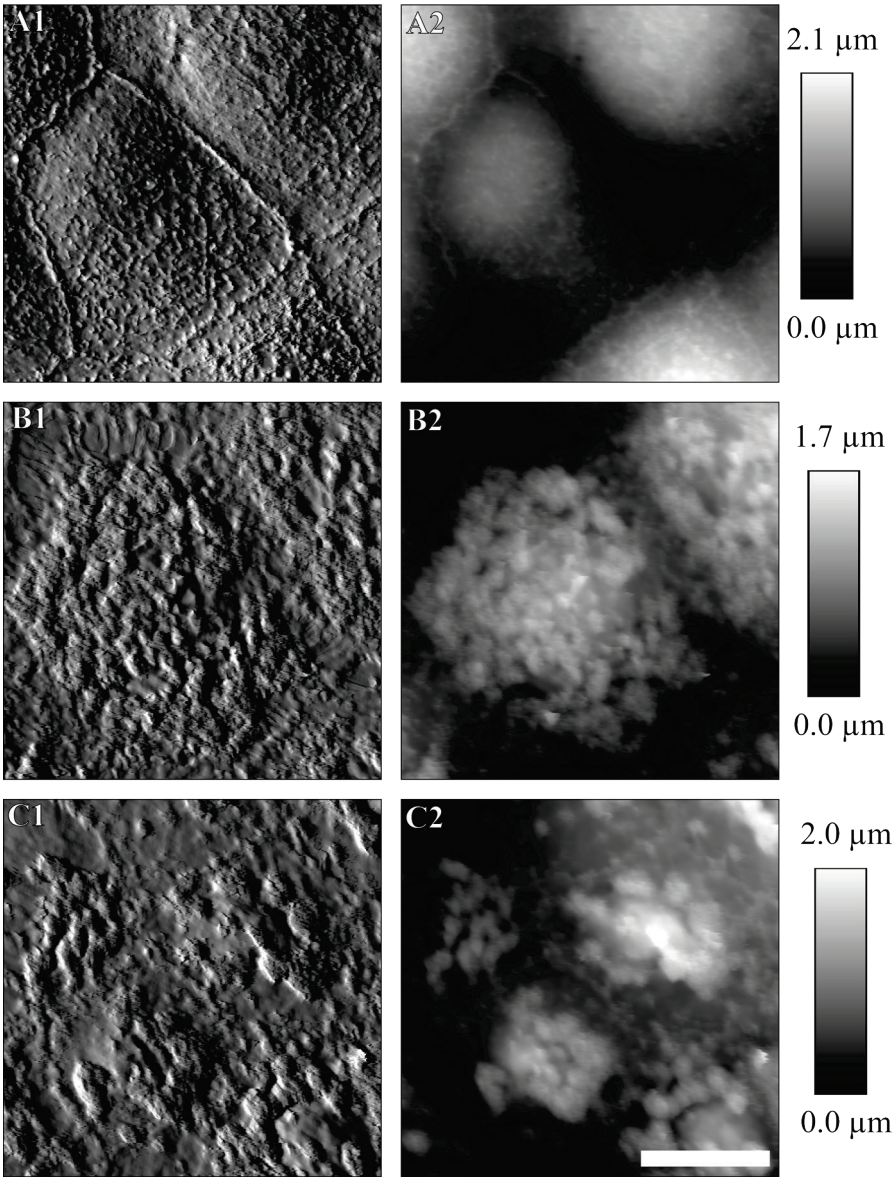

Figure 5.13: Topographical investigation of the effect of Jasplakinolide on MDCK II cells. A: Untreated cells. B: Cells after 30 min of Jasplakinolide administration (1 µM). C: Cells exposed to Jasplakinolide (1 µM) for 60 min. 1: Deflection images. 2: Height images. Cells were fixed with 2.5% GDA before imaging in contact mode. Scale bar: 10 µm.

ECIS experiments revealed that the effect of Jasplakinolide on MDCK II cells occurs with a delay of more than 30 min compared to the sudden onset of Latrunculin A treatment. A significant drop in the impedance signal at 4 kHz becomes apparent when the drug is already removed from the cell culture medium (Figure 5.14 A). The membrane capacitance decreases just after removing the drug. After approximately 10 h C_m nearly returns to its initial value (Figure 5.14 B). Interestingly, however, the

impact of Jasplakinolide on the barrier resistance and cell-substrate distance becomes already visible after 30 min of drug treatment. Both parameters drop down. Recovery occurs within approximately 8 h (Figure 5.14 C-D).

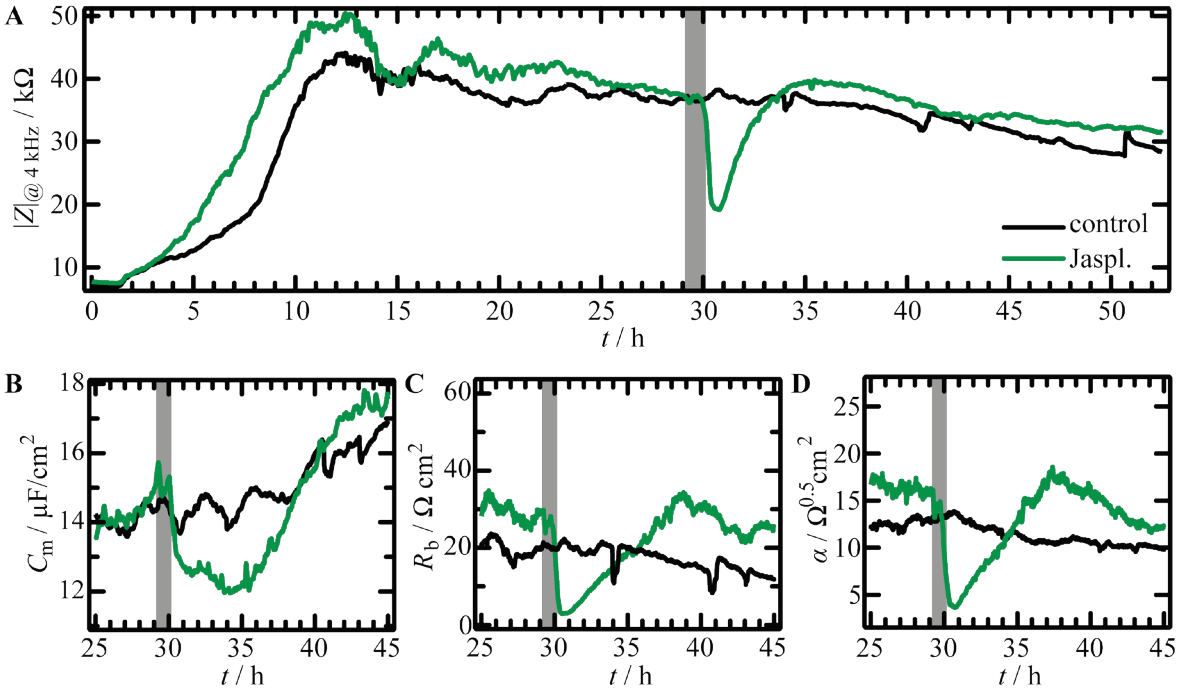

Figure 5.14: ECIS measurements of MDCK II cells treated with 1µM Jasplakinolide for 1 h. A: Impedance spectra recorded at 4,000 Hz. B: Membrane capacitance C_m. C: Barrier resistance R_b. D: Parameter α describing the cells-surface distance. Black curves represent untreated cells; green ones show Jasplakinolide (1 µM) treated cells. The incubation time, starting approximately 29 h after seeding the cells on the electrode, is highlighted in grey (1 h).

The mechanical properties of Jasplakinolide treated MDCK II cells were investigated by AFM indentation experiments followed by tether pulling. Without applying any model for quantitative calculations, the mechanical response of the cells due to indentation is already reflected in the shape of the force-indentation curves (Figure 5.15). After 30 min exposure of the cells to the drug (Figure 5.15, green curves), the slope of the force-indentation curves is significantly steeper compared to those recorded on untreated cells. After further 30 min of drug treatment, the averaged curve (Figure 5.15, red) is closer to the one found for untreated cells again. The distribution is much broader covering the full range of curves for untreated cells and cells after an incubation time of 30 min.

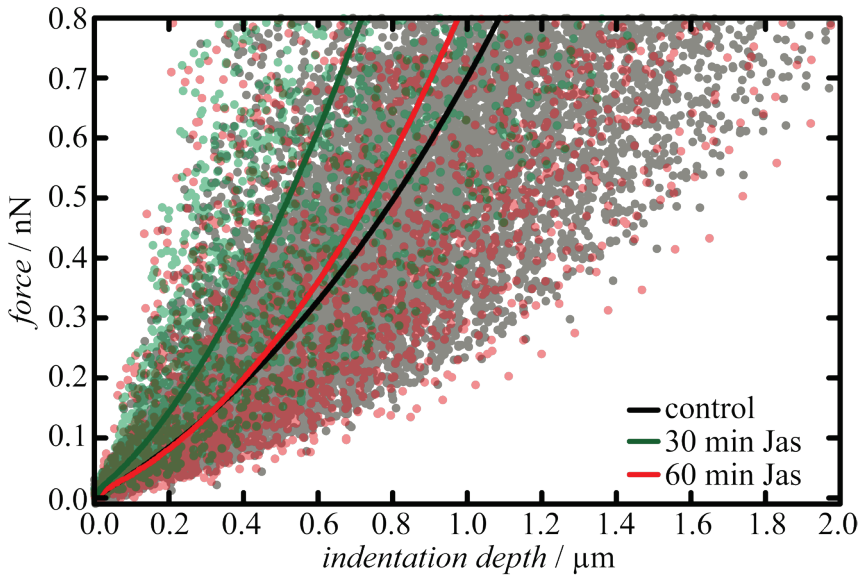

Figure 5.15: Force-indentation curves recorded on MDCK II cells exposed to different stimuli. The averaged curve for untreated cells is shown in black, for cells treated for 30 min with 1 µM Jasplakinolide in green and for an incubation time of 60 min in red. The semi-transparent dots in corresponding colour represent the original data recorded on cells with different treatments.

After reinforcement of the F-actin cytoskeleton on the apical side, cells behave stiffer compared to control cells within 30 min. The overall tension increases from $t_0 = (0.60 \pm 0.02)$ mN/m (untreated cells) to (0.95 ± 0.07) mN/m. After additional 30 min of incubation t_0 drops back to (0.54 ± 0.06) mN/m (Figure 5.16 A). The same trend can be found for the apparent area compressibility modulus. After 30 min Jasplakinolide administration, $\tilde{K}_A$ increases to (0.41 ± 0.05) N/m (control: $\tilde{K}_A = (0.157 \pm 0.007)$ N/m). After 60 min $\tilde{K}_A$ is regulated down to (0.28 ± 0.05) N/m (Figure 5.16 B). The membrane tension is only slightly affected by Jasplakinolide treatment of the cells. It slightly increases from $t_t = (0.170 \pm 0.005)$ mN/m to (0.18 ± 0.01) mN/m within 30 min. After 60 min t_t was found to be (0.15 ± 0.01) mN/m (Figure 5.16 C). The histograms for t_0 and $\tilde{K}_A$ show two populations after 30 min of incubation. Interestingly, according to eq. (3.6), tension generated by active contraction of the cortex is nearly doubled after 30 min Jasplakinolide administration ($t_{act} = 0.78$ mN/m, control: $t_{act} = 0.43$ mN/m). After 60 min the initial value is mainly restored ($t_{act} = 0.39$ mN/m).

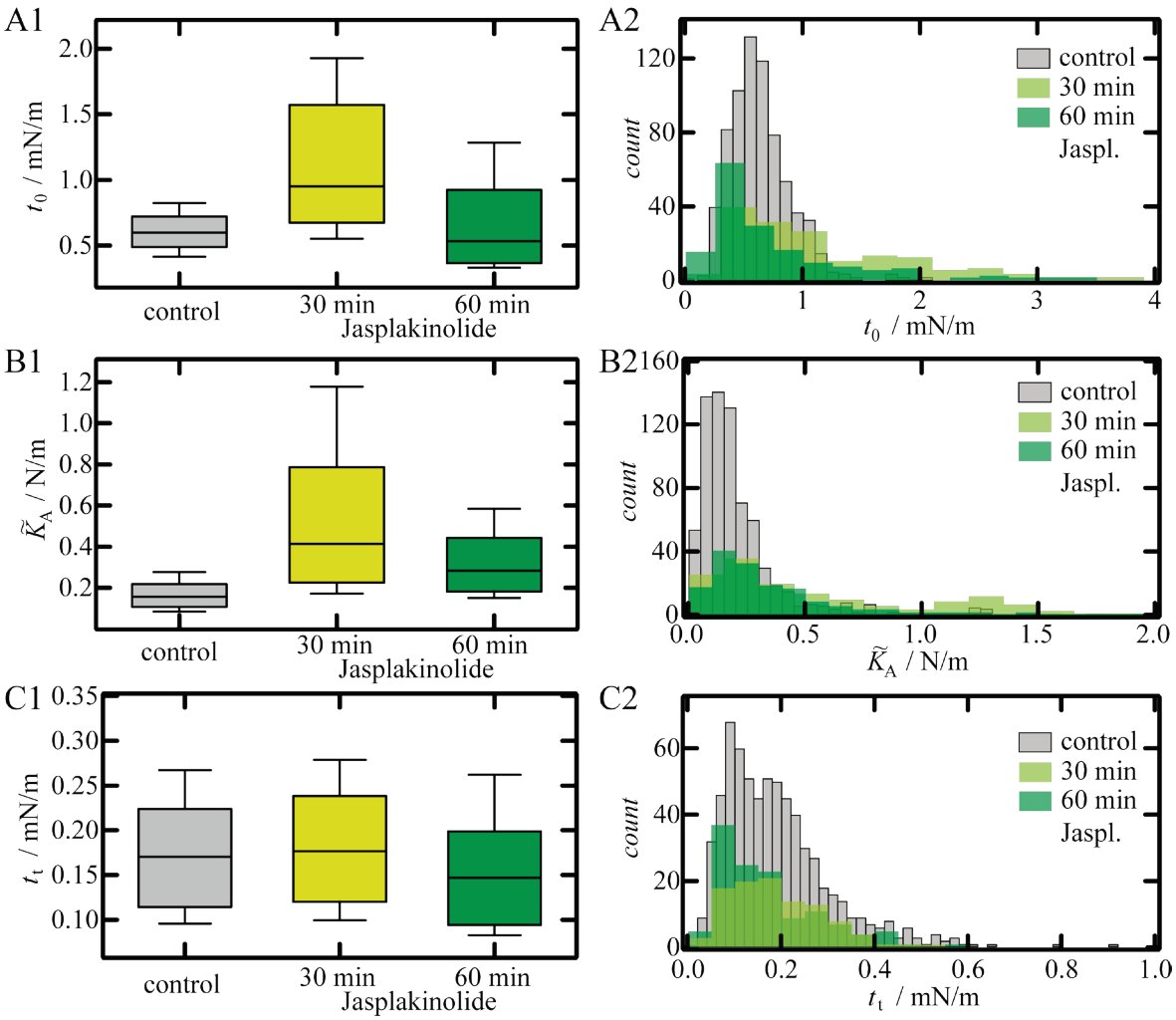

Figure 5.16: **Mechanical properties of MDCK II cells after exposure to Jasplakinolide. A1: Box plot for the overall tension t_0. A2: Corresponding histogram. B1: Box plot showing the apparent area compressibility modulus $\tilde{K}_A$. B2: Histogram corresponding to B1. C1: Box plot for membrane tension t_t. C2: Histogram corresponding to C1. Grey boxes and bars represent values for untreated cells, light green ones after 30 min 1 µM Jasplakinolide administration, dark green ones after 60 min. Box plots extend from the 30th to the 70th percentile, whiskers from the 20th to the 80th. A: n = 720 (control), 166 (30 min Jaspl.), 173 (60 min Jaspl.) analysed force-indentation curves. B: n = 713 (control), 154 (30 min Jaspl.), 170 (60 min Jaspl.) analysed force-indentation curves. C: n = 668 (control), 104 (30 min Jaspl.), 128 (60 min Jaspl.) force-retraction curves.**

5.2.3 Discussion

Interference with the actin cytoskeleton has a major impact on the mechanical behaviour of the cell. By applying two different drugs, consequences of a destroyed cytoskeleton as well as of a reinforced F-actin cortex on the apical side were studied.

Degradation of F-actin was achieved by Latrunculin A, a substance capping monomeric actin. The success was confirmed by fluorescence microscopy. Former filigree structures on the apical cell side are turned into bigger actin agglomerates just beneath the plasma membrane. AFM images confirmed these findings. How strongly these structural changes influence the mechanical behaviour was shown in AFM force-indentation experiments. The overall tension is reduced by more than a factor of two within 30 min and was found to be more than three times lower after 60 min of Latrunculin A administration. Since one binding partner of ezrin is destroyed and consequently membrane tethers can be formed easier, the rupture force and thus t_t is lowered because γ_{ad} is diminished (eq. (3.8)). Both the overall tension and the apparent area compressibility modulus drop over time, whereas the tension generated by the active contraction of the cytoskeleton, t_{act}, is reduced after 30 min of incubation and remains on this level even after longer times of incubation with the drug. This demonstrates the importance of an intact actin architecture for active tension generation. Noireaux *et al.* found that the stiffness (elastic modulus E) of a branched actin network is correlated to its mesh size ξ by an expression of the form of $E \sim 1/\xi^4$ (power 4!) [143], demonstrating that degradation of the actin cortex inevitably results in softening of cells.

Although the plasma membrane appears to be more smooth, a drop in $\tilde{K}_A$ was found. Combining the results from $\tilde{K}_A$ with the results of AFM imaging, the lowered compressibility modulus may be better explained by a weaker connection between membrane and cytoskeleton than by an enhanced membrane area. The membrane is free-standing, only stabilised by the osmotic pressure, and consequently easier to indent. Membrane material can be recruited from a virtually larger reservoir to react to the deformation, reflected in a decreasing apparent area compressibility modulus. Additionally, in ECIS experiments evidence for a decreasing cell surface indicated by a decreasing membrane capacitance during drug treatment was found. Cell-cell junctions cannot be supported by F-actin in the central focal plane anymore.

The contractile ring is impaired. Thus, the barrier resistance drops. Furthermore, ECIS experiments showed that depolymerisation of F-actin on the basal side (stress fibre destruction) resulted in a greater cell-substrate distance, which is reflected in a decrease of α. For fibroblasts Rotsch and Radmacher found a decrease in the Young's modulus due to exposure to depolymerising drugs, such as Cytochalasin B, Cytochalasin D and Latrunculin A [144]. Pietuch *et al*. reported a drop in t_0, $\tilde{K}_A$ and t_t on shorter timescales after Cytochalasin D administration to MDCK II cells [12]. These findings are in good agreement with the results described here.

Quite the opposite effect on the cytoskeleton was achieved by Jasplakinolide treatment of the cells. The reinforcement of the actin cytoskeleton was shown by fluorescence microscopy. Observation of GFP-tagged actin expressing cells demonstrated the great impact of Jasplakinolide on the actin cytoskeleton. The effect of the drug was confirmed by a second approach. Phalloidin staining of non-transfected MDCK II cells revealed the same trend, but the effect of the drug was found to be less pronounced. Visualisation of drug treated cells by Phalloidin staining, however, does not yield reliable results, since phalloidin competes with Jasplakinolide for the same binding site of F-actin [141], although it is still in use [145]. The findings about actin reinforcement were supported by Shurety and co-workers [146]. In their study a bunching of the apical cell side was reported, which could be confirmed with our study by AFM imaging. Shurety *et al.* also found thicker stress fibres on the basal cell side, whereas our study demonstrates the opposite. Furthermore, Zhang and co-workers reported the assembly of actin clouds in endothelial cells due to Jasplakinolide treatment [145]. Reinforcement of F-actin on the apical side leads to an increase in the overall tension and the apparent area compressibility modulus within 30 min. Interestingly, the membrane tension is not affected by a thicker cortex. The connection between plasma membrane and cytoskeleton seems to be still intact. The initial overall tension is mostly restored after an incubation time of 60 min, whereas $\tilde{K}_A$ is only slightly downregulated. An enhanced apparent area compressibility modulus might be better explained by probing the actin cortex than by a reduction of excess membrane area. ECIS experiments demonstrated a constant or even a slightly enhanced membrane capacitance during drug treatment. Only a slight drop in membrane tension was found after 60 min of Jasplakinolide administration. These findings are at odds with

results obtained by Rotsch *et al*. for fibroblasts treated with the same drug. In their study a decrease in the elastic modulus was found after Jasplakinolide administration. They further reported persistent stress fibres. In our study, a significantly reduced amount of stress fibres was found. ECIS experiments support the idea that the attachment to the substrate is weakened, which is indicated by a decreasing α. Furthermore, cellular contraction was confirmed by a significant drop of the barrier resistance R_b, reflecting an opening of cell-cell contacts. Interestingly, changes in the mechanical behaviour were found after 30 min of drug incubation. This is the point where ECIS parameters start to change. After 60 min all ECIS parameters are significantly lowered, whereas the mechanical parameters t_0 and $\tilde{K}_A$ are mainly affected within the first 30 min and under control again within 60 min of incubation. A possible explanation of the recovery of the mechanical behaviour can also be a disruption of long stable actin bundles due to a high drug concentration. G-actin is depleted by Jasplakinolide and the normal F-actin turnover is impaired [147]. The elastic behaviour of cells is not only defined by the amount of actin bundles. There is ample evidence in the literature that the connection between single actin filaments has a great impact on the mechanical behaviour of those networks [148,149]. One possible explanation of the regulation of the overall tension within 60 min could be a loosening of the actin network. The membrane tension t_t remains nearly constant in the first 30 min of actin reinforcement. Later, a drop in t_t contributes to homeostasis of the overall tension t_0. However, the recovery of the impedance signal after both drug treatments provides evidence that the cells survive both challenging situations.

With the experiments described in this chapter, a deeper understanding of how epithelial cells behave after interfering with cortical integrity was gained. However, strong alterations of the cellular topography together with significant softening of the cells (Latrunculin A) bring the tension model to a limit. As described in sections 3.2.2 and 5.1, the geometry of the cell is essential to compute the apical cell cap. Since the model only includes this cellular apex to calculate the mechanical parameters, the indentation depth δ of the tip theoretically cannot be deeper as the height of the cap h. When this constraint ($h > \delta$) is violated, the model fails to describe the recorded force-indentation curves (Figure 5.17).

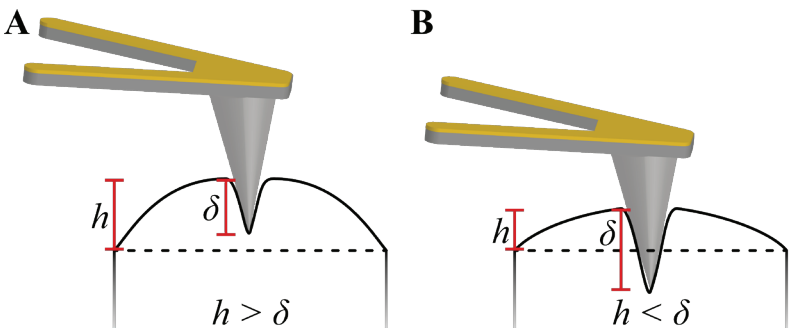

Figure 5.17: The tension model is only applicable if the height *h* of the apical cap is greater than the indentation depth δ (A). When the indentation depth exceeds the height of the apex (B), the model cannot be applied.

This problem occurs for Latrunculin A treated cells. However, to get an idea of the overall tension and apparent area compressibility modulus, it was decided to apply the parameters used for untreated cells also for those exposed to both kinds of drugs. Thus, flattening of the apical cap was neglected by adjusting ϕ. Thereby it was possible to apply the tension model to the recorded AFM curves to investigate the impact of mechanics in addition to evaluating the course of the force-indentation curves. Numerical values, however, should only be seen as a tendency.

5.3 The Impact of the Membrane-Cytoskeleton Attachment

Parts of experiments and data processing described in this section were performed by Stefan Nehls during his Master's thesis. The research was originally published in [32] or in The Journal of Biological Chemistry. Julia A. Braunger, Bastian R. Brückner, Stefan Nehls, Anna Pietuch, Volker Gerke, Ingo Mey, Andreas Janshoff and Claudia Steinem. Phosphatidylinositol 4,5-Bisphosphate Alters the Number of Attachment Sites between Ezrin and Actin Filaments A COLLOIDAL PROBE STUDY. The Journal of Biological Chemistry. *2014; 289: 9833-3843. © the American Society for Biochemistry and Molecular Biology. Figures were reproduced or adapted from these references.*

In previous studies it was found that an enhanced membrane-cytoskeleton interaction alters the mechanical behaviour of cells tremendously [23,32]. The question arises, how a weaker connection between these two binding partners contributes to cellular behaviour in terms of morphology and mechanics. Two different approaches were applied. First, the ezrin mediated connection was disrupted by a chemical. In a second step, ezrin was depleted in MDCK II cells by RNA interference.

5.3.1 Weakening of the Plasma Membrane-Cytoskeleton Attachment by NSC 668394

In a first approach the ezrin mediated membrane-cytoskeleton attachment was weakened by the chemical compound NSC 668394. This small molecule inhibits the phosphorylation of the conserved threonine residue Thr-567 [150]. Phosphorylation of this site is essential for switching ezrin from its dormant into an activated state.

Cells were incubated with 250 µM NSC 668394 for three hours. As a result, significant changes in the ezrin distribution were found by confocal microscopy (Figure 5.18). Ezrin no longer appears as small dots on the apical side. It shows a more disperse arrangement after NSC 668394 administration. The actin distribution

is also changed. The microvilli representing small dots now appear blurred (Figure 5.18 A1, B1). In the central focal plane a certain amount of ezrin is localised at the cell-cell boundaries after incubation of the cells with the drug (Figure 5.18 A2). F-actin surrounding the cells at the lateral side is more pronounced as well (Figure 5.18 B2). At the basal side there is little ezrin at the cell-cell boundaries. F-actin stress fibres, which are characteristic for polarised epithelial cells, vanish after incubation with NSC 668394 (Figure 5.18 B3).

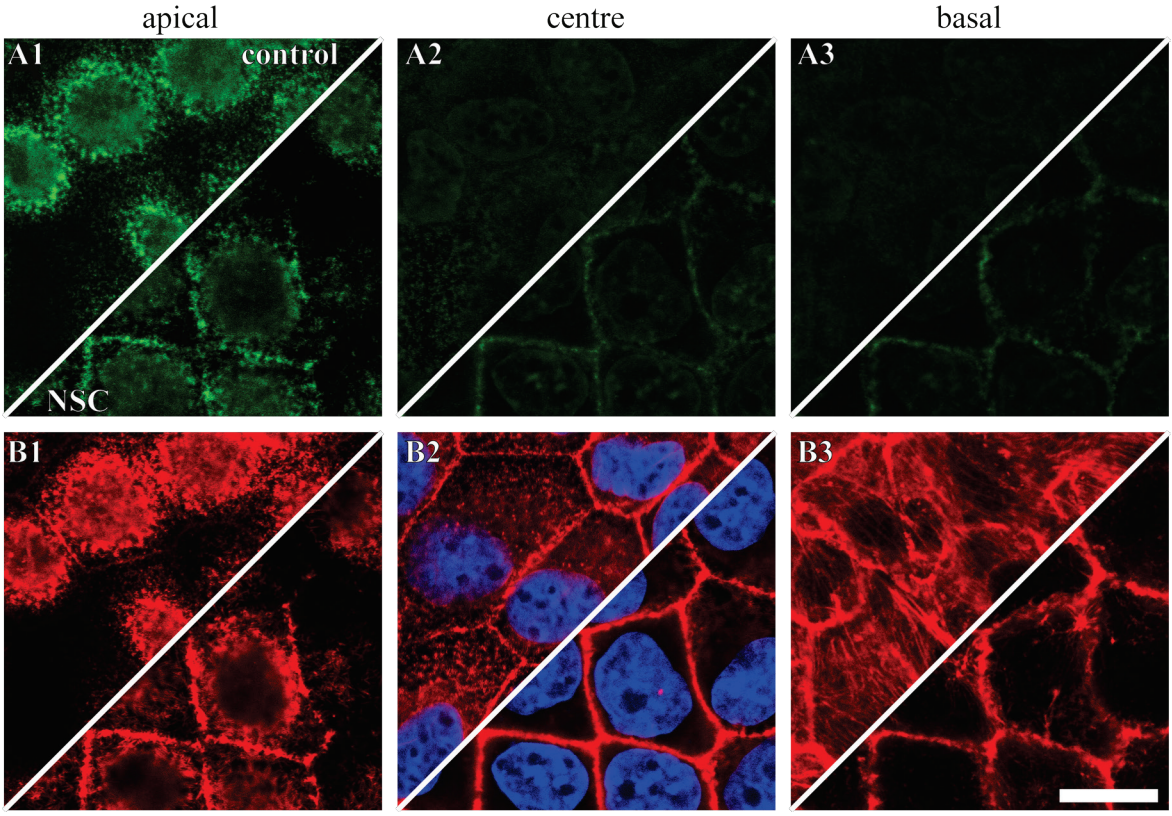

Figure 5.18: Confocal fluorescence images of MDCK II cells after exposure to NSC 668394. A: Fluorescence staining for ezrin. B: Actin stained with fluorescently marked Phalloidin. 1: Apical side. 2: Central focal plane. 3: Basal side. Untreated cells are shown on the upper left side, cells treated for 3 h with 250 µm NSC 668394 are depicted on the lower right side. Scale bar: 15 µm.

The impact of the small molecule NSC 668394 on the topological behaviour of MDCK II cells was analysed by AFM imaging of GDA fixed cells in contact mode. The contractile ring at the cell-cell boundaries is much more pronounced for drug treated cells compared to control cells. Microvillar structures are still present at the

cell surface (Figure 5.19 A). The height of the apical cap is reduced compared to untreated cells (Figure 5.19 B).

Taken together, it might be reasonable to assume that alterations in the protein distributions, as well as the morphological changes, both caused by drug treatment and found by fluorescence microscopy and AFM imaging, lead to substantial changes in the mechanical behaviour of the epithelial cells. Again force-indentation cycles were recorded. Ezrin is the linker molecule between plasma membrane and cytoskeleton. Thus, the focus was set first on tether pulling experiments, since t_t is dominated by a term describing this connection (eq. (3.8)).

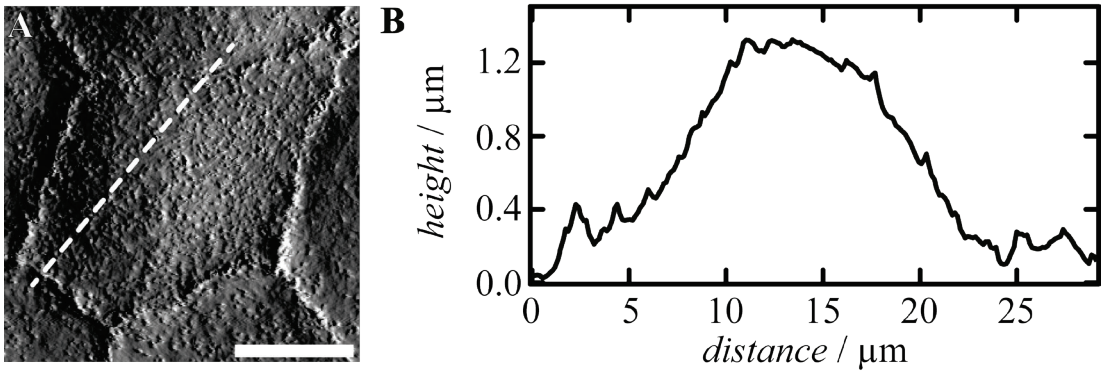

Figure 5.19: Topographical investigation of MDCK II cells exposed to NSC 668394. A: AFM deflection image, recorded in contact mode after 3 h exposure to the drug and fixation with 2.5% GDA. B: Height profile along the white dotted line in A. Scale bar: 10 µm.

After NSC 668394 administration, t_t is significantly lowered. Within 3 h it was found to be $t_t = (0.08 \pm 0.01)$ mN/m , which is less than half of the membrane tension found for untreated cells (control: $t_t = (0.162 \pm 0.006)$ mN/m) (Figure 5.20 A).

Evaluation of force-indentation curves reveals an mechanical response to indentation. To account for the altered cell geometry of drug treated cells, an average base radius of r_1 = 10 µm and a spreading angle of ϕ = 12 ° was used for modelling the force-indentation curves recorded on NSC 668394 treated cells. For control cells, the overall tension is $t_0 = (0.49 \pm 0.01)$ mN/m . Within 3 h of incubation with the small inhibitor molecule, t_0 was found to be (0.91 ± 0.03) mN/m. The area compressibility modulus increased from $\tilde{K}_A = (0.13 \pm 0.01)$N/m to (0.31 ± 0.02)N/m , which is 2.5 times higher than the initial value.

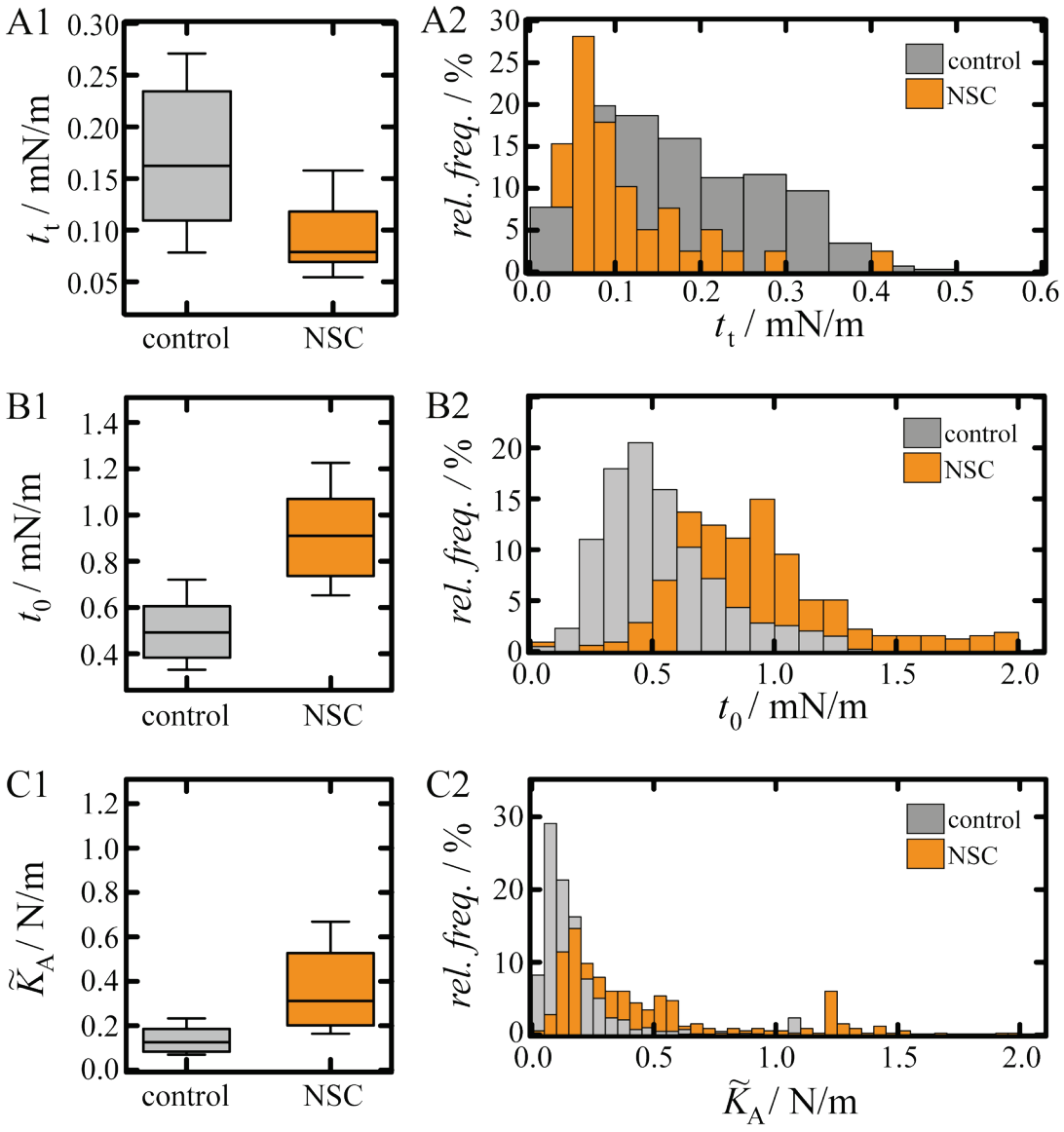

Figure 5.20: The mechanical behaviour of MDCK II cells exposed to 250 µM NSC 668394. A1: Box plot for the membrane tension t_t. A2: Corresponding histogram. B1: Box plot for overall tension t_0. B2: Histogram corresponding to B1. C1: Box plot showing the apparent area compressibility modulus $\tilde{K}_A$. C2: Histogram corresponding to C1. Grey boxes and bars represent values for untreated cells, orange ones after 3 h 250 µM NSC 668394 administration. Box plots extend from the 30th to the 70th percentile, whiskers from the 20th to the 80th. A: n = 256 (control), 39 (3 h NSC 668394) analysed force-retraction curves. B: n = 389 (control), 317 (3 h NSC 668394) analysed force-indentation curves. C: n = 374 (control), 313 (3 h NSC 668394) force-indentation curves.

An increase of the apparent area compressibility modulus can be interpreted as stiffening of the cells at higher strain. In terms of excess membrane area, this can be attributed to a loss of lipid bilayer material. ECIS experiments were performed to

proof this hypothesis. Loss of excess surface material would lead to a decrease in membrane capacitance C_m. Cells were seeded on ultra-small microelectrodes. After reaching confluence, which is indicated by a plateau in the impedance at approximately 4 kHz, NSC 668394 was added (Figure 5.21 A). The cells were incubated for three hours. After administration of the drug, a decrease of the membrane capacity of approximately 16% was found (Figure 5.21 B).

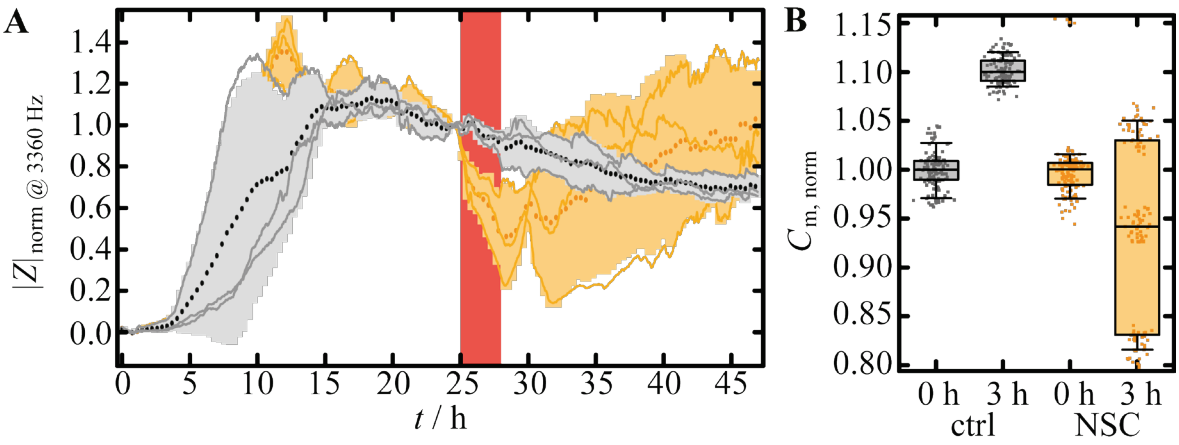

Figure 5.21: ECIS measurements of NSC 668394 treated MDCK II cells. A: Normalised impedance spectra at 3360 Hz over time. Grey curves represent the impedance of untreated cells (solid lines). Dots show the averaged spectrum. Orange curves show the spectra of NSC 668394 treated cells (solid lines) and the corresponding averaged spectrum (dots). The incubation time is highlighted in red. B: Box plots showing normalized membrane capacitance C_m. Electrode response for control measurements are shown in grey, electrodes for NSC treatment in orange. 0 h samples indicate values obtained from the impedance spectra recorded over a time period of 1 h before addition of NSC, 3 h samples represent values obtained 2-3 h after NSC administration.

DMSO can have an impact on MDCK II cells. However, NSC 668394 is only highly soluble in DMSO. In cell medium with low DMSO concentration it can precipitate. Thus, the cells are not only exposed to the drug during experimentation, but also to a certain amount of the solvent. To exclude possible effects of DMSO on the mechanical behaviour of the cells, control experiments were performed. The cells were exposed to the same amount of DMSO as used for NSC 668394 experiments, but without the drug. No significant changes in all of the three values describing the mechanical behaviour were found (Figure 5.22). The membrane tension was found to be $t_t = (0.181 \pm 0.005)$ mN/m (control: $t_t = (0.162 \pm 0.006)$ mN/m). t_0 drops very

slightly from (0.49 ± 0.01) mN/m to (0.45 ± 0.02) mN/m. The apparent area compressibility modulus drops down to (0.06 ± 0.02) N/m (control: $\tilde{K}_A = (0.13 \pm 0.01)$N/m).

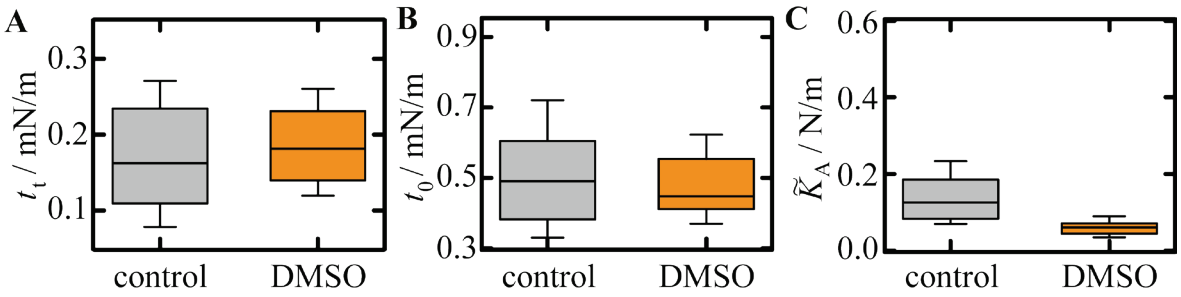

Figure 5.22: The impact of the solvent DMSO on the mechanics of MDCK II cells. A: Membrane tension t_t. B: Overall tension t_0. C: Apparent area compressibility modulus $\tilde{K}_A$. Box plots extend from the 30th to the 70th percentile, whiskers from the 20th to the 80th. A: *n* = 256 (control), 228 (DMSO) analysed force-retraction curves. B: *n* = 389 (control), 62 (DMSO) analysed force-indentation curves. C: *n* = 374 (control), 61 (DMSO) force-indentation curves.

These experiments demonstrate that DMSO in this concentration has only a slight effect on the mechanical behaviour of MDCK II cells. The apparent area compressibility modulus is slightly lowered. This tendency stays in contrast to results found for NSC 668394 treated cells. Thus, the effect of the drug might be slightly underestimated for $\tilde{K}_A$.

5.3.2 Blocking of the Ezrin Expression in MDCK II Cells by siRNA

Albeit the experiments using NSC 668394 for weakening of the plasma membrane-cytoskeleton attachment give a deep insight into the impact of this interface on cellular mechanics, a second, more reliable approach was chosen to interfere with ezrin. siRNA was applied to block the ezrin expression with a minimum of side effects. Sub-confluent cells were incubated with siRNA for three days. Within this period of time, full confluence was reached. The success of the blocking experiments was confirmed by western blotting and fluorescence staining (Figure 5.23). The western blot shows a significantly lower signal for ezrin for cells treated with siRNA compared to untreated ones. Fluorescence images show that ezrin can

be blocked in a sufficient amount of cells by RNA interference. The F-actin distribution was also analysed by fluorescence microscopy. In contrast to NSC 668394 experiments, in this case no significant changes were found.

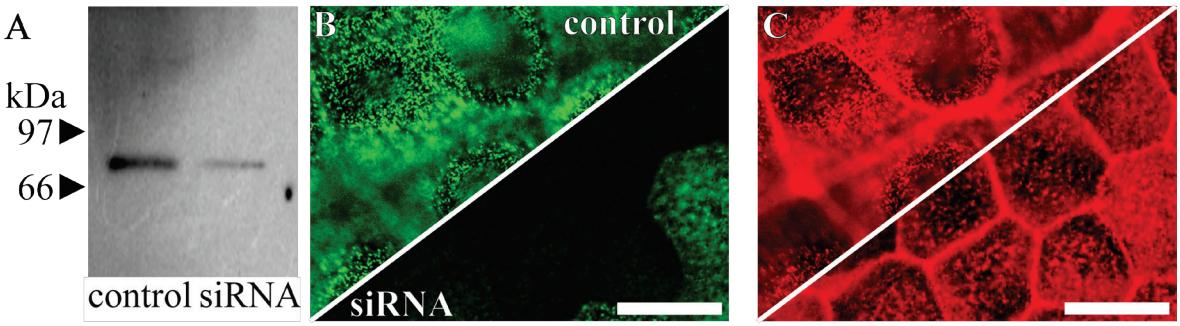

Figure 5.23: Gene silencing of ezrin in MDCK II cells. A: Western blot for ezrin of untreated (control) cells and cells exposed to ezrin siRNA. B: Fluorescence images of ezrin-labelled cells. C: Fluorescence micrographs showing F-actin corresponding to the same region shown in B. Upper left side: untreated cells, lower right side: Cells incubated with siRNA. The focus was set on the apical cell side. Scale bar: 20 µm.

In NSC experiments, a flattening of the cells was found as a consequence of a weaker connection between plasma membrane and cytoskeleton. To check if RNA interference has the same effect, different experiments were performed (Figure 5.24). Confocal fluorescence images show a flattening of successfully transfected cells. In Figure 5.24 B-E a spot of the sample was chosen, where successfully transfected cells coexist with barely transfected ones. This illustrates the impact of the ezrin knock-down on the cell morphology in a single image. The apical cap of ezrin knock-down cells is substantially flattened, with a height of approximately 0.8 µm (Figure 5.24 F). The tension generating contractile ring is still present (Figure 5.24 D).

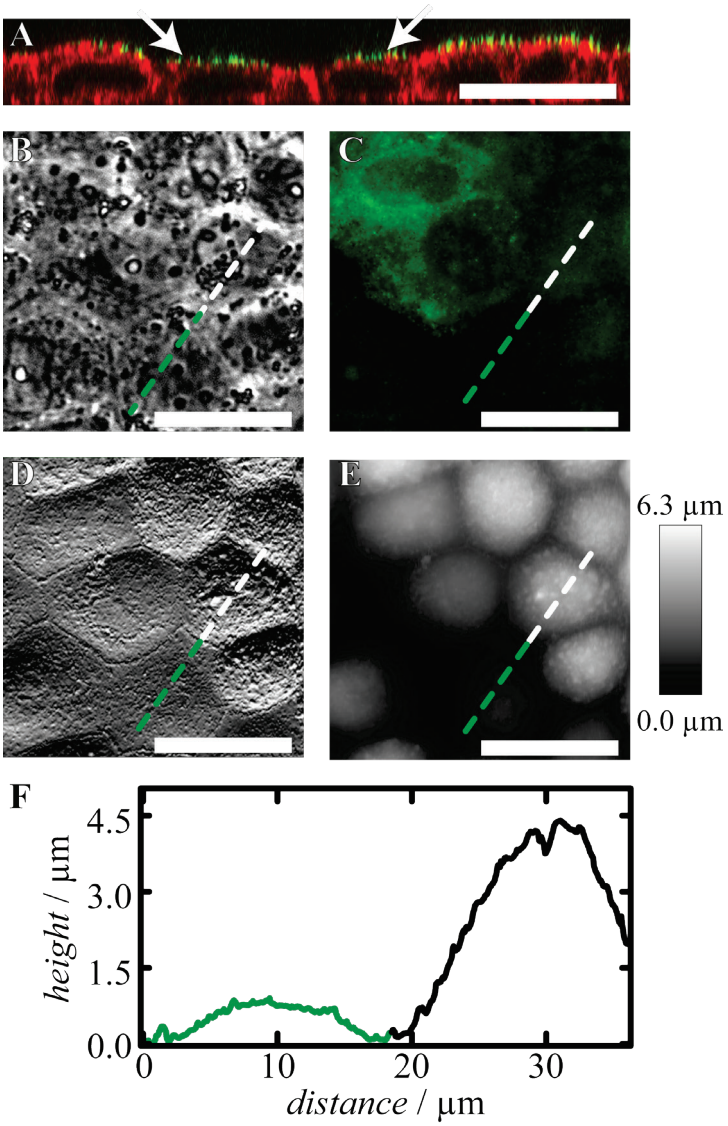

Figure 5.24: Topographical investigation of MDCK II cells after ezrin interference with siRNA. A: Confocal fluorescence image (*xz*-plane) of a confluent cell layer. The plasma membrane is stained in green, actin is marked in red. Successfully transfected cells are highlighted by an arrow. B: Phase contrast image. C: Corresponding fluorescence micrograph showing the ezrin distribution. D: AFM deflection image. E: AFM height image. F: Height profile along the green/white dotted line. Scale bar: 20 µm.

To analyse the mechanical behaviour of ezrin knock-down cells, force-indentation cycles were recorded by AFM. To ensure that measurements were only performed on successfully transfected cells, fluorescence experiments were performed afterwards (data not shown).

The analysation of force-retraction curves revealed a lowered membrane tension of $t_t = (0.084 \pm 0.007)$ mN/m for ezrin knock-down cells (control: $t_t = (0.162 \pm 0.006)$ mN/m) (Figure 5.25 A). Force-indentation curves were subjected to the fitting procedure of the tension model. The same geometrical parameters used for curves recorded on NSC 668394 treated cells were applied. Thereby, the altered geometry of the apical cap was taken into account. Ezrin knock-down causes an increase of the overall tension to (0.72 ± 0.04) mN/m (control: $t_0 = (0.49 \pm 0.01)$ mN/m) (Figure 5.25 B). The apparent area compressibility modulus shows the same tendency. $\tilde{K}_A$ increases from (0.13 ± 0.01) N/m to (0.31 ± 0.04) N/m after the ezrin knock-down by RNA interference (Figure 5.25 C).

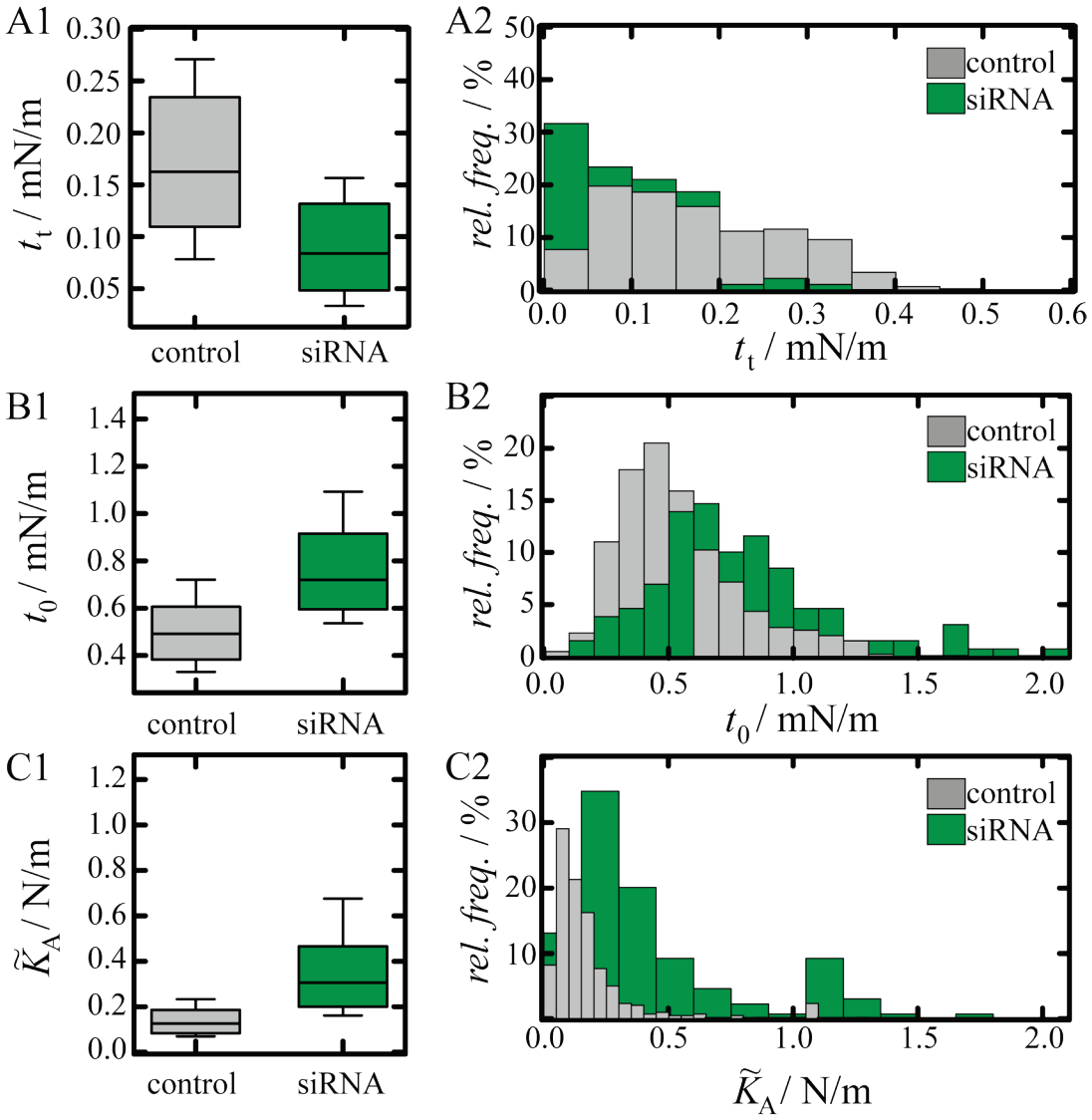

Figure 5.25: The mechanical behaviour of MDCK II cells lacking ezrin provoked by RNA interference. A1: Box plot for the membrane tension t_t. A2: Corresponding histogram. B1: Box plot for overall tension t_0. B2: Histogram corresponding to B1. C1: Box plot showing the apparent area compressibility modulus $\tilde{K}_A$. C2: Histogram corresponding to C1. Grey boxes and bars represent values for untreated cells, green ones values for ezrin depleted cells. Box plots extend from the 30th to the 70th percentile, whiskers from the 20th to the 80th. A: *n* = 256 (control), 85 (siRNA) analysed force-retraction curves. B: *n* = 389 (control), 129 (siRNA) analysed force-indentation curves. C: *n* = 374 (control), 129 (siRNA) force-indentation curves.

Since siRNA interferes with the protein expression machinery, there are a few side effects possible. To ensure that the alterations in the mechanical behaviour of the cells originate from the lacking ezrin or *ZO-1* (see chapter 5.4.1), and not from the transfection procedure, non-targeting siRNA was applied as a proof of principle

(Figure 5.26). In this experiment only a slight drop of the membrane tension from $t_t = (0.162 \pm 0.006)$ mN/m down to (0.125 ± 0.007) mN/m was found. The overall tension stays nearly constant (non-targeting siRNA: $t_0 = (0.48 \pm 0.01)$ mN/m, control: $t_0 = (0.49 \pm 0.01)$ mN/m). In contrast to ezrin and *ZO-1* siRNA, for non-targeting siRNA a drop in the apparent area compressibility modulus from $\tilde{K}_A = (0.13 \pm 0.01)$ N/m down to (0.050 ± 0.009) N/m was found.

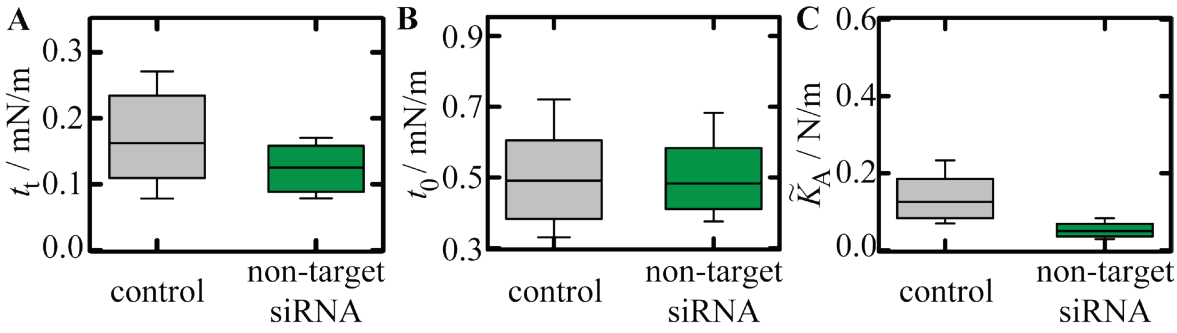

Figure 5.26: The impact of the transfection procedure on the mechanics of MDCK II cells tested by non-targeting siRNA. A: Membrane tension t_t. B: Overall tension t_0. C: Apparent area compressibility modulus $\tilde{K}_A$. Box plots extend from the 30th to the 70th percentile, whiskers from the 20th to the 80th. A: *n* = 257 (control), 218 (non-target siRNA) analysed force-retraction curves. B: *n* = 389 (control), 317 (non-target siRNA) analysed force-indentation curves. C: *n* = 374 (control), 264 (non-target siRNA) force-indentation curves.

These control measurements with non-interfering siRNA clearly indicate that the impact of the transfection procedure on the mechanical behaviour of MDCK II cells is rather small. Only a slight drop in the apparent area compressibility modulus is notable. One possible explanation could be that the cells are not as tight packed as in control samples and a full polarisation was not reached after 3 d of incubation.

5.3.3 Discussion

In this section the interface formed between the plasma membrane and the actin cortex was investigated. The linker molecule ezrin was blocked in two ways. In a first approach, phosphorylation of the conserved threonine residue Thr-567 was blocked by the small molecule NSC 668394 [150]. As a consequence, dormant ezrin

cannot switch between its closed and opened conformations. C- and N-terminal regions are associated with each other. Neither binding to F-actin, nor to PIP_2 in the plasma membrane is possible. This impairing is strongly reflected in the membrane tension t_t, since this value is dominated by the connection between plasma membrane and cytoskeleton (eq. (3.8)). The membrane tension drops significantly after phosphorylation of Thr-567 is blocked by NSC 668394. Furthermore, an enhanced overall tension was found. Even the apparent area compressibility modulus increased to a 2.5 times higher value. The second approach, ezrin knock-down by RNA interference confirmed all these findings. Interestingly, both techniques have different time-scales (hours *vs.* days) to achieve the depletion effect. In both cases a reduction of the height of the apical cap was found and after both treatments a comparable mechanical behaviour was found. Previous studies analysed the mechanical behaviour of single cells lacking ezrin in the context of a confluent monolayer. Here, the apical cap was found to be reduced in height as well. The tether rupture force, which is proportional to the square root of membrane tension, decreased. Overall tension and apparent area compressibility modulus are enhanced [32]. Surprisingly, Hayashi *et al.* found no changes in the cell morphology of epithelial cells after ezrin depletion by siRNA [151]. Here, a clear impact on the cell morphology, namely the flattening of the apical cap, was verified by two different approaches. Pietuch found the same changes in cell morphology for single ezrin depleted cells provoked by neomycin microinjection [13,32].

Other previous studies provoked the contrary effect in MDCK II cells. A higher plasma membrane-cytoskeleton attachment was achieved by microinjection of PIP_2 in single cells of a confluent monolayer. The enhanced connection was reflected in higher membrane tension [23]. Interestingly, it was found that cells become stiffer after PIP_2 microinjection. The overall tension increased over time. Afterwards a down-regulation occurred. The same tendency was found for the apparent area compressibility modulus. In these studies the increase was attributed to the fact that a higher connection leads to a reduction of locally available membrane material, resulting in higher apparent area compressibility moduli [32]. However, in the present study an increase in t_0 and $\tilde{K}_A$ after weakening of the plasma membrane-cytoskeleton attachment was found. This result can be attributed to the changes in cell height. A reduction of the apical cap height of approximately 1-2 µm was found

regardless of the technique chosen for ezrin depletion. This effect might be due to a loss of cell polarity and a higher contraction of the overall morphology. An increasing overall tension accompanied by a dropping membrane tension can only be explained by an increase of t_{act} (eq. (3.6)). The loss of excess surface material was confirmed by ECIS measurements. This effect largely explains the increase of the apparent area compressibility modulus. Furthermore, previous studies demonstrated that ezrin depletion in MDCK cells leads to a reduction of microvillar structures by scanning and transmission electron microscopy. The remaining microvilli appear thicker [151]. This also explains an enhanced $\tilde{K}_A$ found in our study. Taken together with former results, it is save to conclude from the results of this study that epithelial cells regulate their membrane tension through the interface between the plasma membrane and cytoskeleton. This interface is formed by the protein ezrin. If the connection is impaired, contract forces of the cortex might lead to a collapse of the cells.

5.4 The Impact of Cell-Cell Contacts

Cell-cell contacts are important to build up a tight cellular network, which protects subjacent cells. Forming these barriers is one of the main functions of epithelial cells. In order to address the question of how cell-cell connections influence the mechanical behaviour of single cells two cell-cell contact forming proteins are scrutinised. First, the tight junction mediated cell-cell connection was investigated. *Zonula occludens-1* was depleted by RNA interference. Second, adherens junctions formed by E-cadherin-E-cadherin interaction were impaired by drug treatment of the cells. Thus, we could shine light on the role of the cell-cell connections for tension homeostasis of epithelial cells.

5.4.1 The Tight Junction Protein Mediated Cell-Cell Connection

Tight junctions are the uppermost cell-cell connections of epithelial cells. They are formed by occludin together with the tight junction protein 1, *zonula occludens-1* (*ZO-1*) [74]. To elucidate the role of this connection for the mechanical behaviour of epithelial cells, short interference RNA was applied to block *ZO-1* expression in MDCK II cells.

The optical appearance of a confluent MDCK II cell monolayer is shown in Figure 5.27 A. The tight junction protein 1 builds up a perfect mesh surrounding each cell (Figure 5.27 C). Cells lacking *zonula occludens-1* show defects in the cell monolayer (Figure 5.27 B) and appear separated from each other. Fluorescence microscopy of cells with fluorescently labelled *ZO-1* (immunostaining) provides evidence that the applied siRNA blocks *ZO-1* expression with high efficiency (Figure 5.27 D).

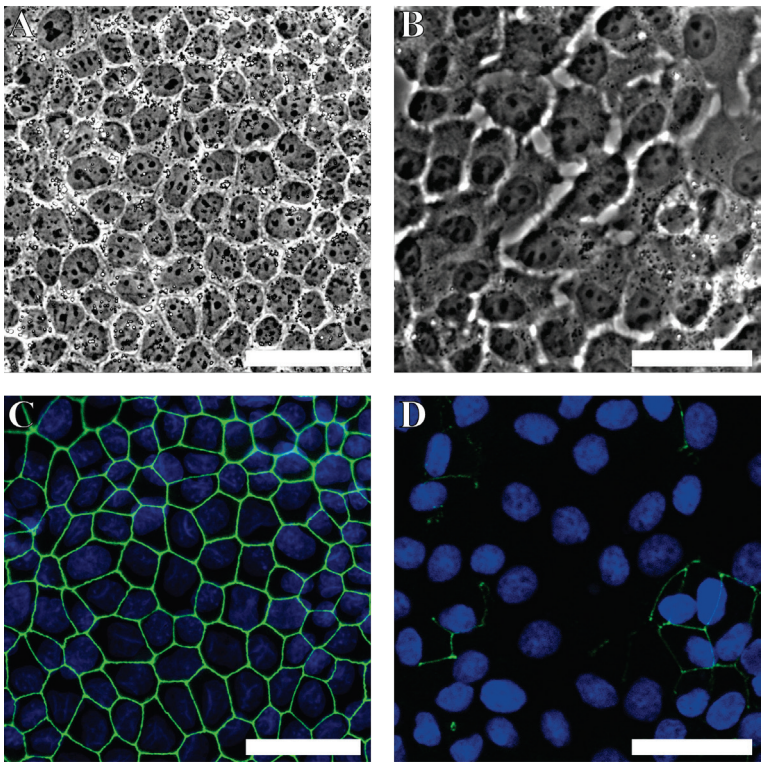

Figure 5.27: Short interference RNA depletes the expression of the tight junction protein 1, *zonula occludens-1*. A, B: Phase contrast images of an untreated MDCK II cell monolayer (A) and MDCK II cells treated for 3 d with siRNA against *ZO-1* (B). C, D: Fluorescence micrographs showing *zonula occludens-1* (green) and nuclei (blue). Untreated cells (C) show a dense *ZO-1* network, whereas the protein expression of the tight junction protein 1 is effectively blocked in cells exposed to siRNA (D). Scale bar: 40 µm.

Since *zonula occuldens-1* is connected to the F-actin cytoskeleton (see chapter 2.6.1 and Figure 2.4), the actin distribution was also investigated. Small disperse F-actin points, representing the microvilli on the apical cell side (Figure 5.28 A), are altered in cells lacking *ZO-1*. The structures appear more clustered. It may be the case that the amount of actin is slightly increased. Clearly defined F-actin bundles on the basal side (stress fibres, Figure 5.28 C) disappear in the absence of a *ZO-1*-mediated cell-cell connection (Figure 5.28 D). At some cell borders the cells seem to be separated over the full lateral side.

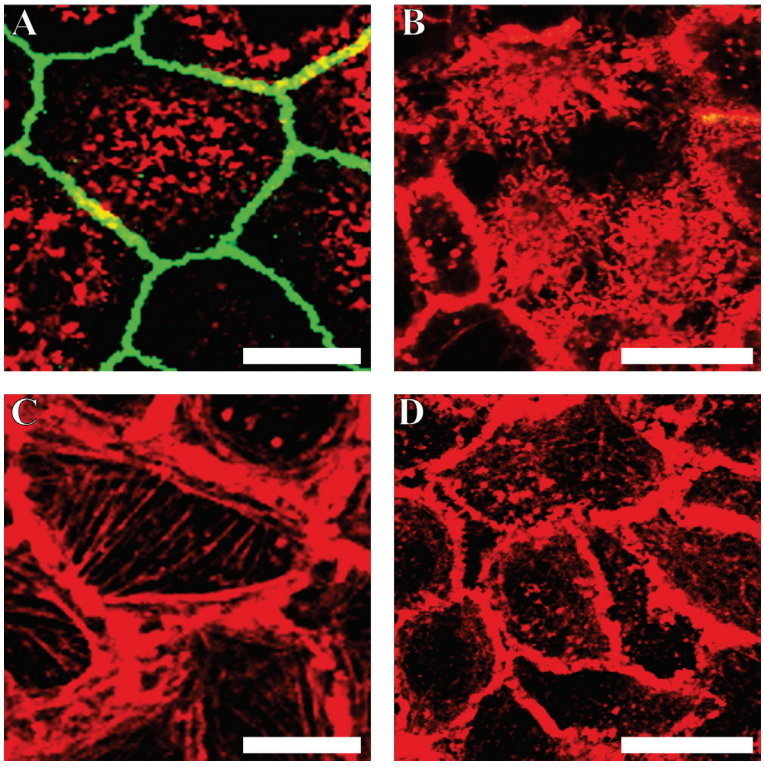

Figure 5.28: The impact of *ZO-1* depletion on the F-actin distribution of MDCK II cells shown by confocal fluorescence microscopy. F-actin is stained in red, *zonula occludens-1* in green. The focus was set to the apical (A, B) and basal (C, D) cell side. A and C depict untreated cells, *ZO-1* depleted cells are shown in B and D. Scale bar: A, C: 10 µm, B, D: 20 µm.

The topographical properties of *ZO-1* depleted cells are mapped by AFM imaging in contact mode (Figure 5.29). Cell-cell boundaries with cell boarders appearing brighter in phase contrast images do not contain the tight junction protein 1 (Figure 5.29 A, B). It was found that these successfully transfected cells are separated from each other and rounded off. Small point-like features at the apical cell side are replaced by a rough surface with bigger features (Figure 5.29 C-E). It is reasonable to assume that these altered membrane properties originate from the altered underlying cortex structure, which is also found to be more coarse (Figure 5.28 B).

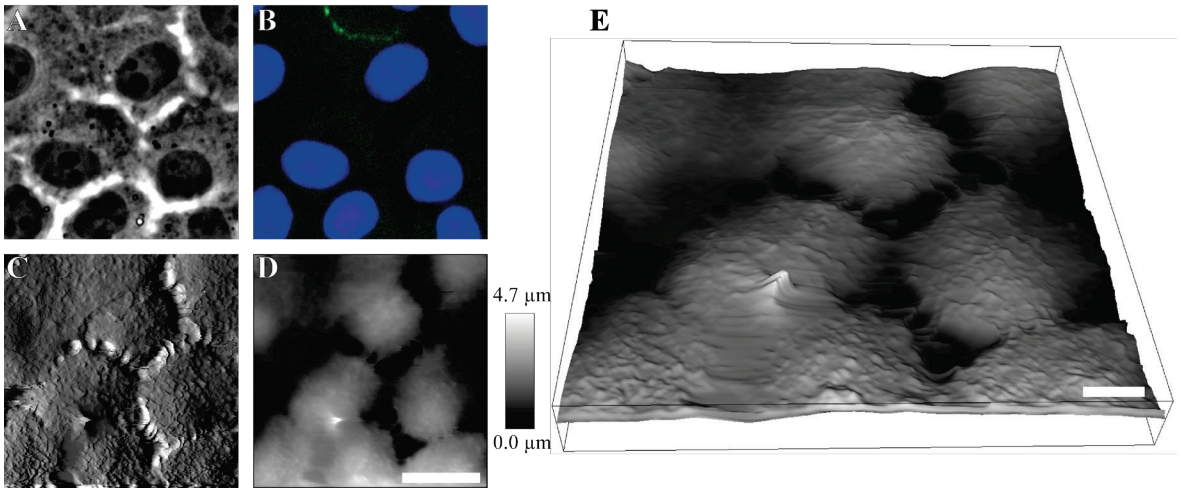

Figure 5.29: Topographical investigation of cells lacking the tight junction protein 1. A: Phase contrast image. B: Corresponding fluorescence micrograph for *ZO-1* stained in green. The nuclei are stained in blue. C: Corresponding AFM deflection image. D: AFM height image of the corresponding region shown in A and B. E: Three dimensional height image of the same region. Scale bar: A-D: 15 µm, E: 5 µm. Box height: 7 µm.

Apart from mechanical models, the cellular response to indentation with an AFM tip is reflected in the measured force-indentation curve without any distortion. Only force-distance curves measured far away from the cell boarders were used for the analysis in this section, since gaps between the cells were observed after RNA interference (Figure 5.29). However, it was found that the impact of the separation of cells from each other by *ZO-1* depletion is rather small compared to other manipulations investigated in this study, such as membrane-cytoskeleton uncoupling (section 5.3). The averaged force-indentation curves show nearly the same course, regardless of whether the tight junction protein 1-mediated cell-cell connection is intact or not (Figure 5.30). For curves recorded on successfully transfected cells, the slope is slightly steeper compared to those recorded on the centre of cells with intact cell-cell connections.

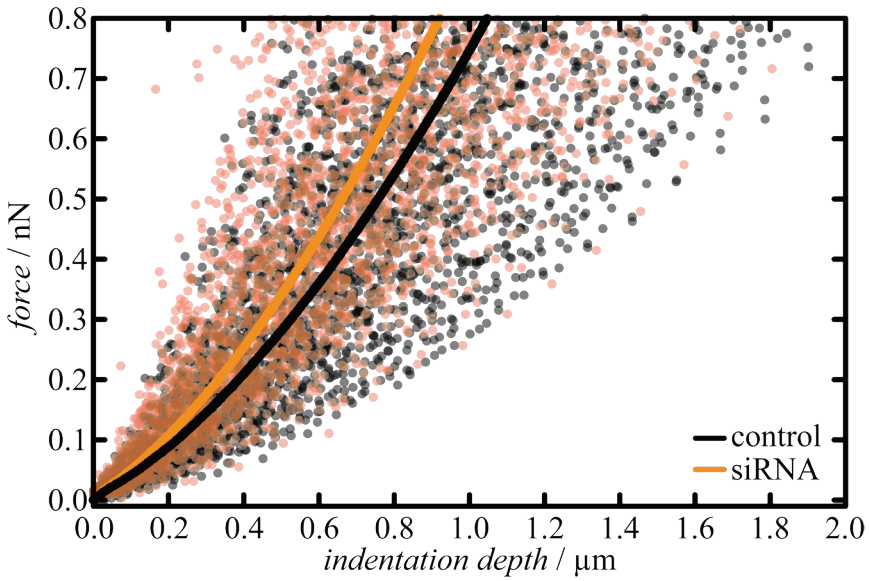

Figure 5.30: Force-indentation curves recorded on MDCK II cells. The averaged curve of experiments performed on untreated cells is shown in black, on cells exposed to siRNA for *ZO-1* in orange. The semi-transparent dots in the corresponding colours represent the original recorded data for the differently treated cells.

The tension model applied to the force-indentation curves takes the geometrical properties of cells into account (chapter 3.2.2). In principle, it is questionable whether this model is applicable to force-indentation curves recorded on cells with this tremendously altered cell geometry. Cells show no clear apical cell cap when *ZO-1* is depleted. For this reason, the geometrical parameters corresponding to the cell shape of untreated cells without any adaption was applied to compute the overall tension and the apparent area compressibility modulus for *zonula occludens-1* depleted cells (Figure 5.31). It was found that both values are barely affected by depletion of this junctional protein. The overall tension slightly increases from $t_0 = (0.756 \pm 0.002)\,\mathrm{mN/m}$ to $(0.862 \pm 0.003)\,\mathrm{mN/m}$. The histogram shows nearly the same distribution for siRNA treated and untreated cells. A broader tail towards higher values becomes obvious for *ZO-1* depleted cells (Figure 5.31 A). The apparent area compressibility modulus shows the same tendency. $\tilde{K}_A$ increases from $(0.18 \pm 0.02)\,\mathrm{N/m}$ to $(0.24 \pm 0.03)\,\mathrm{N/m}$ for cells lacking the tight junction protein 1. A few values found for *ZO-1* depleted cells deviate from those found for control cells. Thus the median is shifted to a slightly higher value (Figure 5.31 B).

The membrane tension, calculated from force-retraction curves, was found to be (0.164 ± 0.004) mN/m (control: $t_t = (0.137 \pm 0.003)$ mN/m. Two dominating peaks were found for siRNA treated cells, one in the range of the main peak for control cells and a second, shifted to a slightly higher value ($t_t \approx 0.18$ mN/m, Figure 5.31 C).

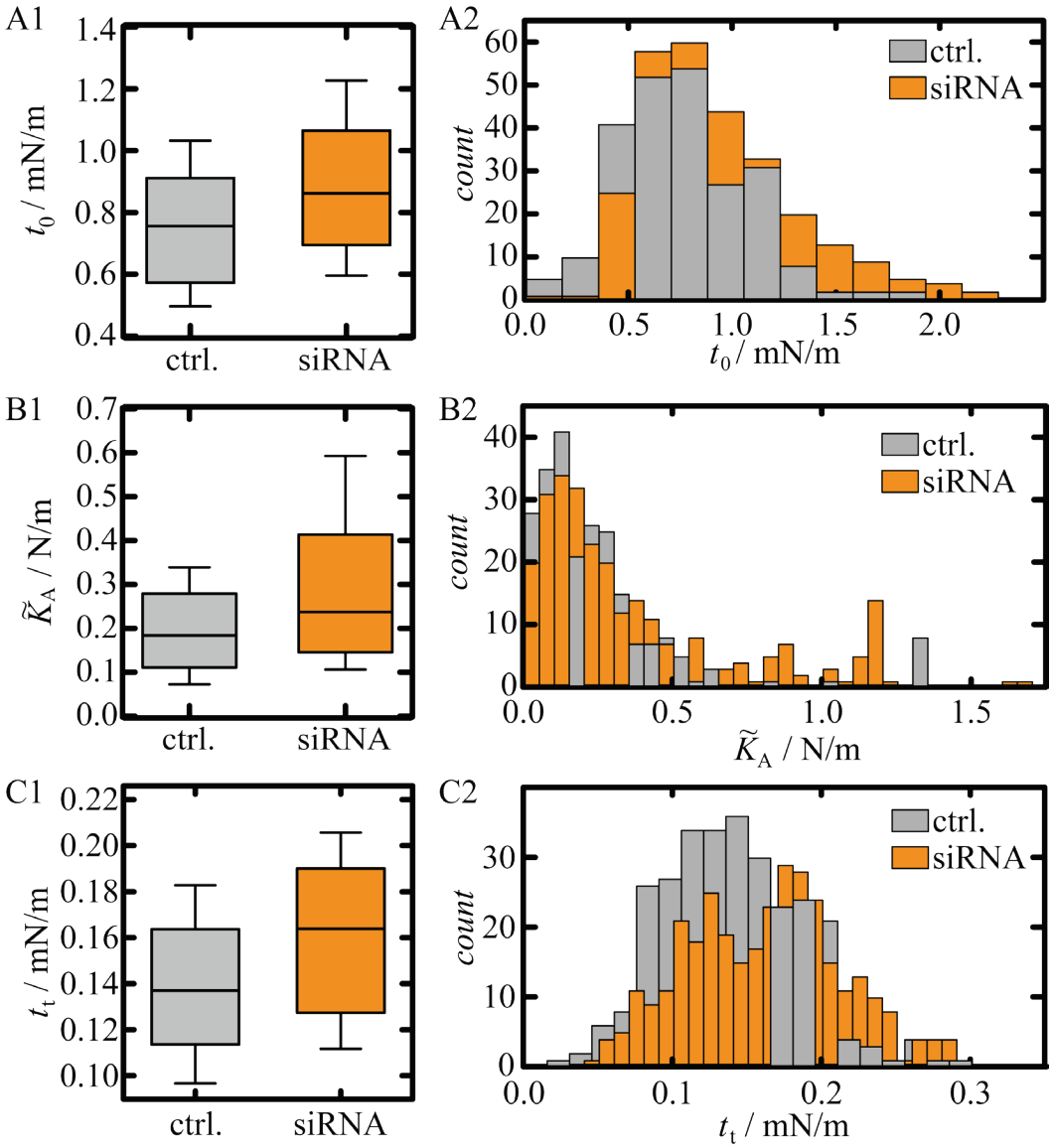

Figure 5.31: Mechanical investigation of *zonula occludens-1* lacking MDCK II cells. A: Overall tension t_0. B: Apparent area compressibility modulus $\tilde{K}_A$. C: Membrane tension t_t. 1: Box plots. 2: Corresponding histograms. Grey boxes and bars represent values for untreated cells, orange ones show values for cells exposed to *ZO-1* siRNA for 3 d. Box plots extend from the 30th to the 70th percentile, whiskers from the 20th to the 80th. A: *n* = 234 (control), 278 (siRNA) analysed force-indentation curves. B: *n* = 232 (control), 269 (siRNA) analysed force-indentation curves. C: *n* = 286 (control), 337 (siRNA) force-retraction curves.

5.4.2 The E-cadherin Mediated Cell-Cell Connection

The E-cadherin mediated cell-cell association is placed just beneath the tight junctional complex (see section 2.6.2). In order to cleave this connection, confluent MDCK II cells were exposed to 1,4-dithio-*D*-threitol (DTT) for 3 h. DTT induces structural changes in the extracellular domain of E-cadherin by reducing disulphide bonds. As a consequence, cells start to separate from each other [152].

In phase contrast images no changes in the cellular structure were found due to exposition of the cells to 10 mM DTT for 3 h (Figure 5.32 A). Fluorescence imaging, however, shows the success of the drug treatment. In the central focal plane a clear E-cadherin signal is found for control cells at the cell-cell boundaries (Figure 5.32 B1). After 3 h of drug treatment, the E-cadherin mediated connection is largely destroyed (Figure 5.32 B2). Three hours after exchanging the drug containing medium with fresh cell culture medium, a slight E-cadherin recovery was found. However, the protein distribution is still impaired. A diffuse, cloudy E-cadherin signal is found inside the cells. The protein has not yet returned to the cell-cell boundaries (Figure 5.32 B3). After further 3 h of recovery (6 h in total), E-cadherin is clearly concentrated at the cell-cell boundaries. The signal is even sharper than for untreated cells. Nevertheless, a certain amount of E-cadherin remains dispersed in the whole cell (Figure 5.32 B4).

The cytoplasmic E-cadherin side is connected to F-actin via α- and β-catenins (Figure 2.4). Thus, the impact of a destructed E-cadherin-E-cadherin connection on the E-cadherin-F-actin linker protein β-catenin is investigated by fluorescence microscopy. As expected, β-catenin is enriched at the cell-cell boundaries for control cells (Figure 5.32 C1). After disruption of the E-cadherin mediated connection, also the β-catenin distribution becomes impaired. There is still a certain amount of this protein near the cellular plasma membrane. However, the signal becomes blurry (Figure 5.32 C2). After a recovery time of 3 h, cells appear to be enriched with β-catenin. The protein distribution remains still blurry within the whole cell (Figure 5.32 C3). After the cells are allowed to recover for 6 h, the observed protein distribution is again comparable to those found in untreated cells (Figure 5.32 C4).

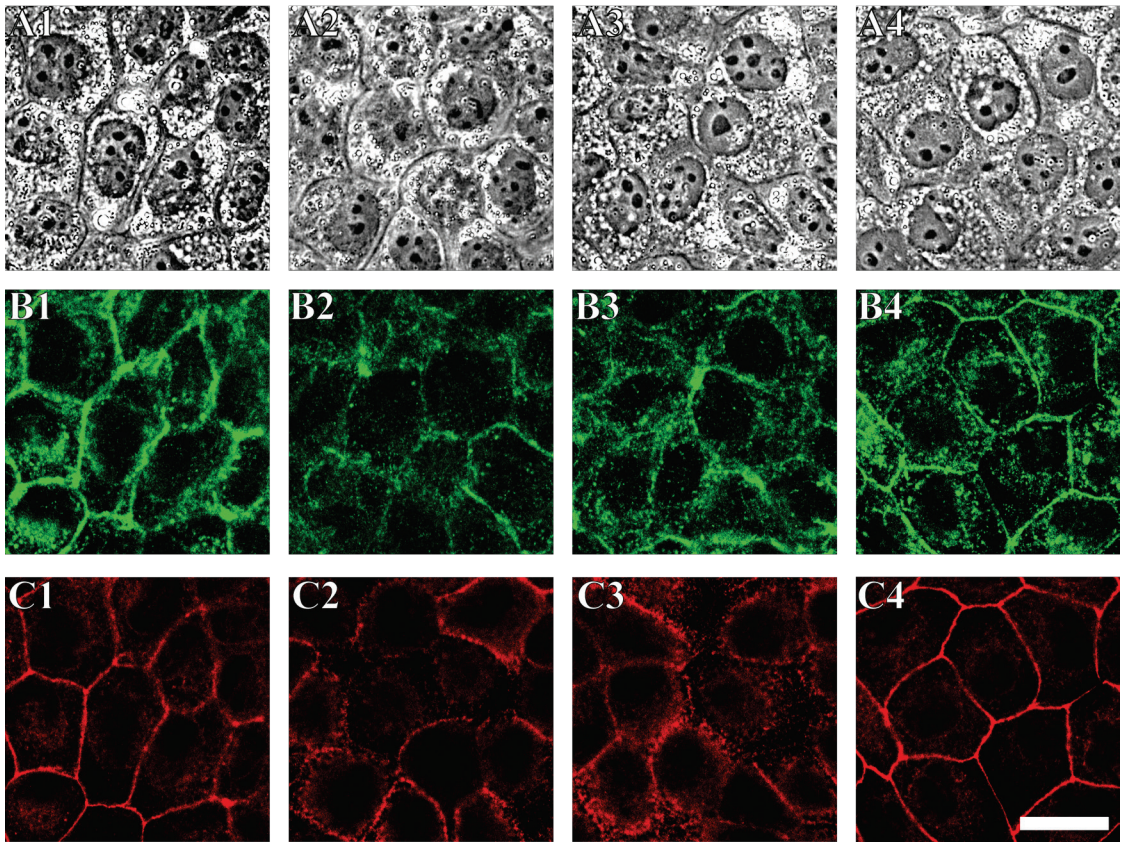

Figure 5.32: DTT destroys the E-cadherin mediated cell-cell connection. A: Phase contrast images. B, C: Fluorescence images for E-cadherin (B) and β-catenin (C). 1: Untreated cells. 2: Cells after exposure to 10 mM DTT for 3 h. 3: Cells observed 3 h after drug removal. 4: Cells observed after a recovery time of 6 h. The focus was set to the central focal plane. Scale bar: 20 µm.

E-cadherin is not only found in the central focal plane, but also on the upper cell side. A certain amount of the protein is aggregated on the apical cap in untreated cells (Figure 5.33 A1). After drug administration, there is less E-cadherin at the apical cell side (Figure 5.33 A2). A significant recovery occurs within 3 h. After 6 h the original state is mostly restored (Figure 5.33 A3, A4). β-catenin, only weakly present on the apical side in control cells, becomes enriched after 3 h exposition of MDCK II cells to 10 mM DTT. Clear structures cannot be found. The same results are observed even after 3 h of recovery of the cells (Figure 5.33 B2, B3). 6 h after the drug is removed, a sharp β-catenin signal returns at the cell-cell boundaries (Figure 5.33 B4).

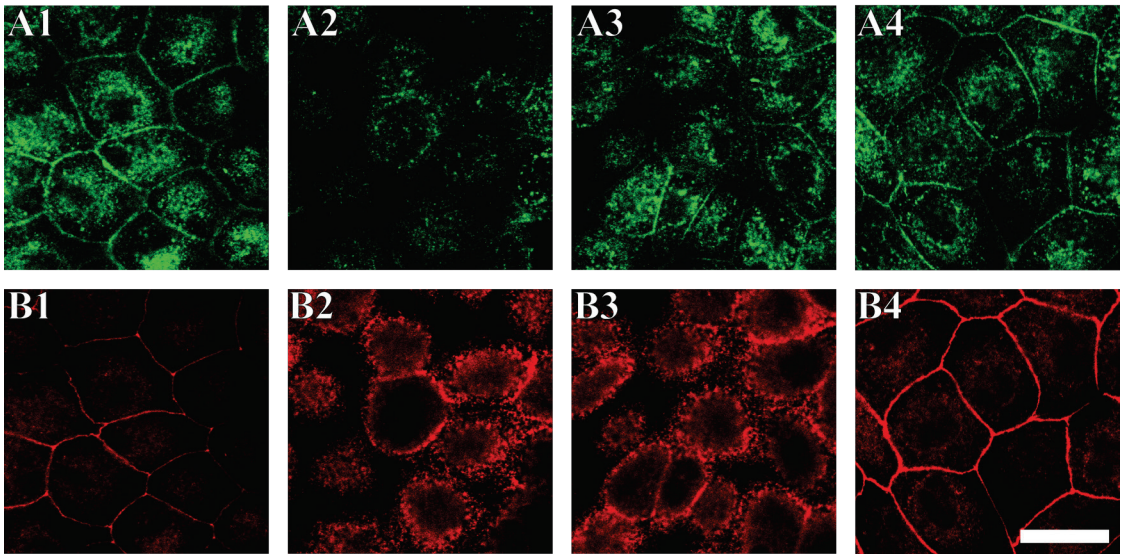

Figure 5.33: DTT alters the distribution of cell-cell connecting proteins on the apical cell side. A, B: Fluorescence images for E-cadherin (A) and *β*-catenin (B). 1: Untreated cells. 2: Cells after exposure to 10 mM DTT for 3 h. 3: Cells observed 3 h after drug removal. 4: Cells after a recovery time of 6 h. Scale bar: 20 µm.

The cells show no separation from each other in phase contrast images during the whole DTT treatment and recovery period. This is a strong hint that some kind of cell-connections remain intact during the whole procedure. In order to confirm this hypothesis, *ZO-1* was stained to check whether tight junctions would remain unharmed. When E-cadherin is highly impaired (after 3 h of DTT incubation), the tight junction mediated cell-cell connection on the apical side is still intact (Figure 5.34 B1, C1). Interestingly, *ZO-1* appears to be slightly impaired, even when the drug is already removed from the cells for 3 h and the E-cadherin recovery has already started (Figure 5.34 B2, C2).

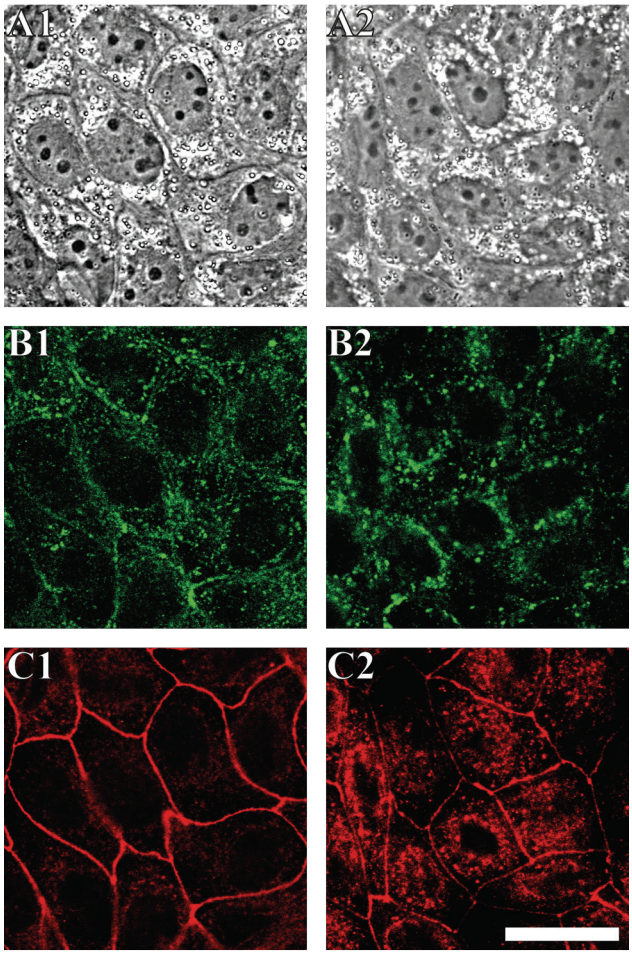

Figure 5.34: DTT slightly affects the tight junction protein *ZO-1*. A: Phase contrast images. B, C: Fluorescence images for E-cadherin (B) and *zonula occludens-1* (C). 1: Cells measured after 3 h of incubation with 10 mM DTT. 2: Cells observed after a recovery time of 3 h after drug treatment. Scale bar: 20 µm.

It was possible to show that the treatment of MDCK II cells with DTT alters the protein distribution of these cells tremendously. Already in confocal fluorescence images it became clear that the height of the cells is altered by the drug treatment (data not shown). In order to quantify this effect, cells were treated with the drug and imaged with an AFM in contact mode. It has to be kept in mind that cells were fixed in this series of experiments using PFA instead of GDA. Thus, fluorescence staining was possible after the topographical investigation, but the quality of the topographical images is lower. However, to get an idea of the geometrical and topological properties of the cells, the image quality is sufficient.

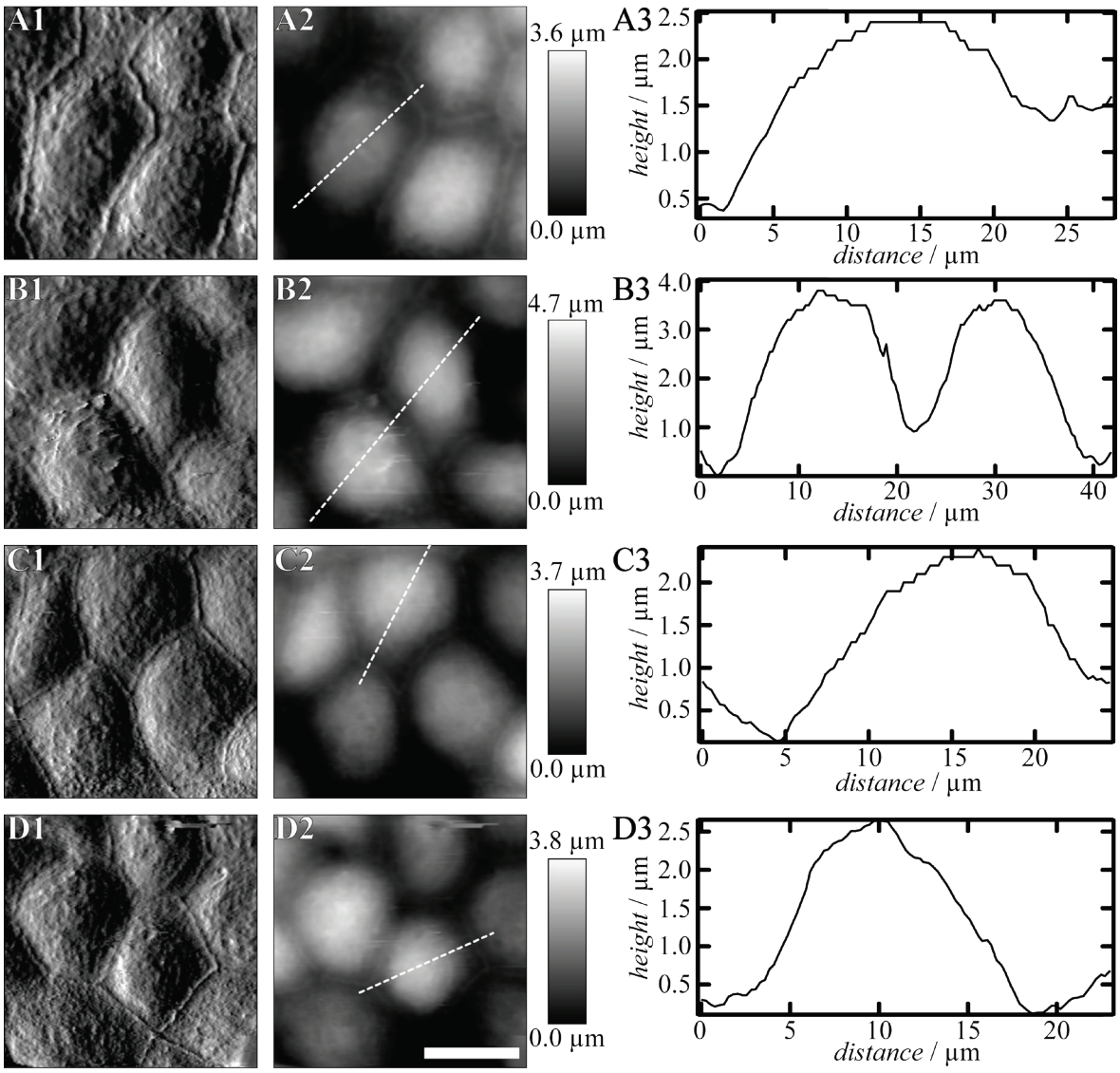

Figure 5.35: The impact of DTT on the cell morphology of MDCK II cells. A: Untreated cells. B: Cells imaged after 3 h exposure to 10 mM DTT. C: Cells 3 h after drug removal. D: Cells after a recovery time of 6 h. 1: Deflection images. 2: Height images. 3: Height profiles along the white dotted lines in 2. Cells were fixed with 4 % PFA solution prior imaging in contact mode. Scale bar: 15 µm.

Untreated cells show a strong wall at the cell-cell boundaries. This can be attributed to a contractile actomyosin ring, which vanishes after adding F-actin depolymerising drugs (see section 5.2.1 and Ref. [12]). For untreated PFA fixed cells microvilli appear not as sharp as found in images of GDA fixed cells. The average height of untreated cells was again found to be approximately (2.00 ± 0.07) µm confirming previous results (chapter 5.1). After 3 h of 10 mM DTT treatment, cells are rounded

off and the height of the apical cap increases to (2.8 ± 0.2) µm (Figure 5.35 B). Again the height is slightly reduced 3 h after the drug is removed from the cells (average height: (2.5 ± 0.2) µm, Figure 5.35 C). After 6 h of recovery the height of the apex is fully recovered to (2.0 ± 0.2) µm (Figure 5.35 D). Interestingly, the contractile ring remains unaffected during the whole procedure (Figure 5.35 column 1).

In order to investigate the influence of impaired E-cadherin mediated cell-cell connections, force distance curves were recorded on cells treated with 10 mM DTT. The strongly altered geometry of the cell apices was taken into account. Different theoretical cell cap shapes were assumed. They are described by the base radius before spreading r_0 and the spreading angle ϕ. Table 5.2 summarises the values that were used.

Table 5.2: Geometrical parameters for computing the apical cap of MDCK II cells exposed to DTT.

Cell Treatment	r_0 / µm	ϕ / °
Untreated cells	35	20
3 h 10 mM DTT	30	26
3 h recovery	32	23
6 h recovery	35	20

After the E-cadherin mediated cell-cell connection is impaired, a significant drop of the overall tension to $t_0 = (0.35 \pm 0.01)$ mN/m (control: (0.59 ± 0.02) mN/m) can be observed. During a recovery time of 3 h, t_0 increases again to (0.73 ± 0.04) mN/m. After further 3 h cells resume an overall tension comparable to those found for untreated cells (6 h recovery: $t_0 = (0.55 \pm 0.04)$ mN/m) (Figure 5.36 A).

The apparent area compressibility modulus is not affected by the drug during the treatment. For control cells it was found to be $\tilde{K}_A = (0.119 \pm 0.006)$ N/m. After 3 h of incubation with DTT, $\tilde{K}_A$ was found to be (0.11 ± 0.01) N/m. Interestingly, when the drug is already removed from the cells for 3 h, the apparent area compressibility modulus is significantly higher ($\tilde{K}_A = (0.19 \pm 0.03)$ N/m). The cells maintain an

increased $\tilde{K}_A$ even after the drug is removed for 6 h. $\tilde{K}_A$ was found to be (0.20 ± 0.08) N/m (Figure 5.36 B).

At the same time, DTT treatment leads to a drop of the membrane tension from $t_t = (0.191 \pm 0.005)$ mN/m to (0.12 ± 0.04) mN/m within 3 h. 3 h after the drug was removed, an increase up to $t_t = (0.23 \pm 0.01)$ mN/m was found. Within the next 3 h a homeostasis occurred and membrane tension dropped down to (0.188 ± 0.006) mN/m (Figure 5.36 C).

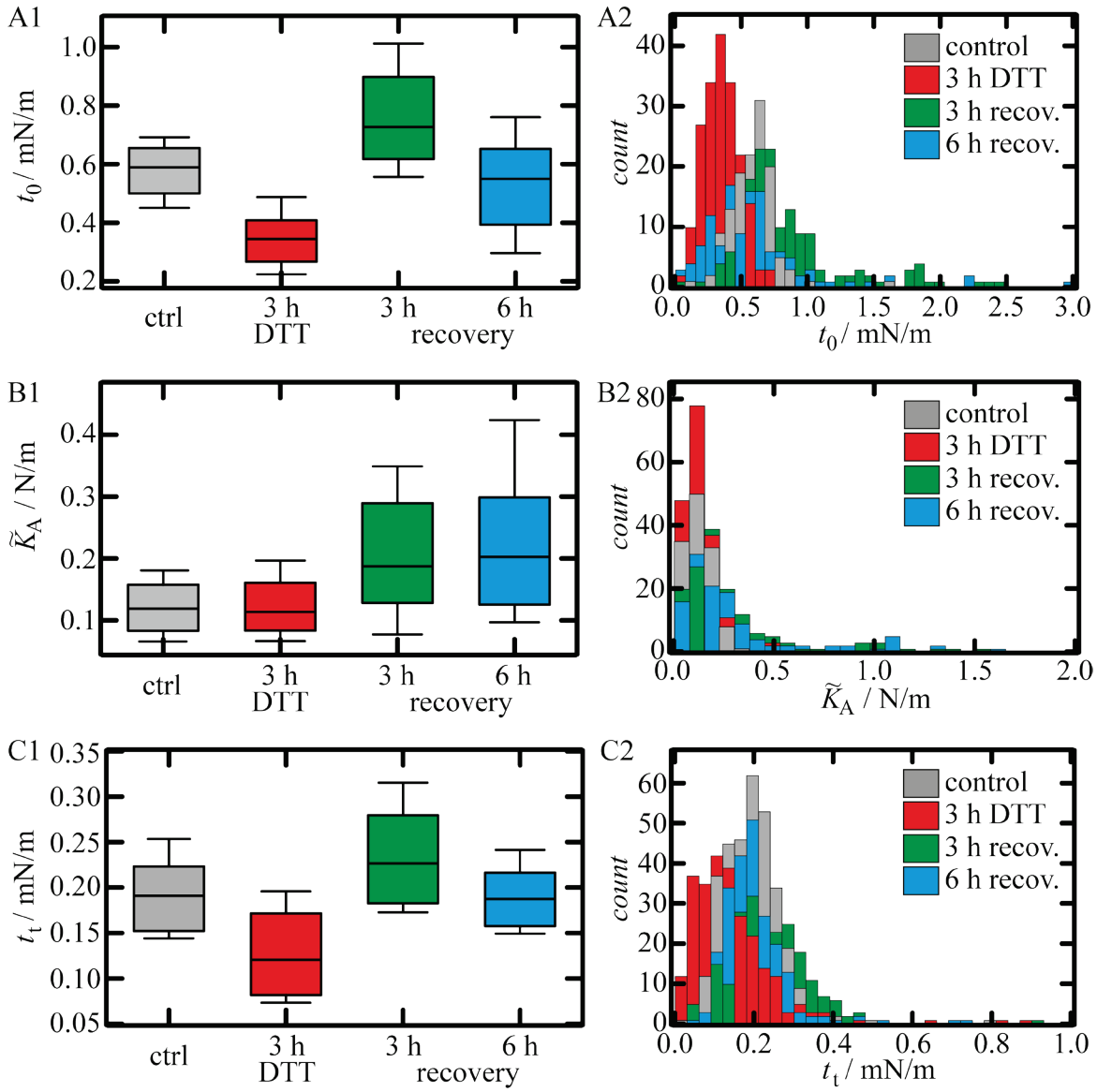

Figure 5.36: **Mechanical investigation of DTT treated cells. A1: Box plot for overall tension t_0. A2: Corresponding histogram. B1: Box plot showing the apparent area compressibility modulus $\tilde{K}_A$. B2: Histogram corresponding to B1. C1: Box plot for the membrane tension t_t. C2: Histogram corresponding to C1. Grey boxes and bars represent values for untreated cells, red ones are calculated from experiments performed 3 h after exposure of the cells to 10 mM DTT. Green boxes and bars represent values recorded 3 h after removal of the drug, blue ones after 6 h. Box plots extend from the 30th to the 70th percentile, whiskers from the 20th to the 80th. A: n = 128 (control), 194 (3 h DTT), 153 (3 h recovery), 123 (6 h recovery) analysed force-indentation curves. B: n = 128 (control), 194 (3 h DTT), 153 (3 h recovery), 122 (6 h recovery) analysed force-indentation curves. C: n = 332 (control), 259 (3 h DTT), 219 (3 h recovery), 222 (6 h recovery) analysed force-retraction curves.**

5.4.3 Discussion

In this section the role of cell-cell contacts for tension homeostasis was investigated. In particular, the proteins responsible for forming tight junctions and adherens junctions were considered. The most apical cell-cell contact is mediated by tight junction proteins, including *zonula occludens-1*. The expression of this protein was blocked by RNA interference. No *ZO-1* was found in transfected cells. As a consequence, cells are divided from each other. A confluent cell monolayer with a tight cellular network could not be formed. A variety of studies confirm structural changes of cells due to *ZO-1* RNA interference [86,153]. Although the impact on the topographical properties of the whole cell layer is tremendous, the influence on the mechanical behaviour is only marginal. These findings were already revealed by a comparison of the recorded force distance curves. Computing the mechanical parameters shows the same tendency. However, application of the tension model should be taken with a grain of salt, since the cell morphology is tremendously altered. The slight stiffening of the cells might be attributed to the slightly increased amount of F-actin at the apical cell side. This may also lead to a higher $\tilde{K}_A$ value. The plasma membrane-cytoskeleton attachment is also very slightly enhanced.

Since *ZO-1* depleted cells are separated from each other, it is reasonable to compare their mechanical behaviour with the mechanics of single cells. Pietuch and Janshoff found that trypsinated MDCK II cells behave very stiffly shortly after attachment to a surface. Regulation of the tension occurs only after a longer period of time, when the adhesion area increases [21]. Schneider and Janshoff investigated the mechanical properties of NMuMG cells during epithelial-to-mesenchymal transition (EMT), a process in which confluent cells lose their cell-cell contacts. NMuMG cells become stiffer over time after inducing EMT accompanied by structural changes of the F-actin cytoskeleton [154]. Our experiments with siRNA treated cells evoke unpolarised cells a short time after seeding onto a Petri dish or cells during EMT. However, the changes found in this study are small compared to the results of Pietuch and Janshoff, and Schneider and Janshoff. As long as the F-actin distribution is mainly intact and unaffected, the mechanical behaviour of the apical cell side remains on a stable level.

The role of cadherin mediated cell-cell contacts for tissue homeostasis and diseases is well studied [155-157]. Here, its role for tension homeostasis was investigated. Consequences of an impaired E-cadherin-E-cadherin interaction are more serious in terms of cellular mechanics although the alterations of the cellular topography are smaller compared to the alterations found for *ZO-1* depleted cells. When E-cadherin mediated cell-cell contacts are impaired, the whole confluent cell layer remains intact. The apical *ZO-1* mediated cell-cell contacts remain mainly unaffected after DTT treatment. Cells round off. Losing the E-cadherin mediated connection is reflected in a decreasing overall tension, whereas the apparent area compressibility modulus is not affected. Membrane tension cannot be maintained when adherens junctions are destroyed. There is evidence that cadherin-actin interactions are responsible for the apical cell morphology [158] and cadherin mechanotransduction influences actomyosin organisation [159,160]. Thus, the drop in overall tension can be explained by a loss of traction force, when the β-catenin mediated E-cadherin-actin connection is impaired. The drop in t_0 is dominated by a loss of tension generated by active contraction of the cortex t_{act}. The drop in t_t also contributes to the lower overall tension, but membrane tension is of minor importance here. Martin *et al.* reported that full intact adherens junctions are necessary in epithelia for tension generation [161]. Further studies demonstrated that a cadherin-mediated cell-cell connection is responsible for force generation in *Drosophila* [162,163]. Adherens junctions produce forces in single cells that can extend to the whole tissue [80,161]. Interestingly, already after 3 h of recovery, tension is restored. A slight overshoot was observed, which ceases after additional 3 h of recovery. The cell seems to use additional membrane material (reflected in an increased apparent area compressibility modulus) for tension homeostasis.

Altogether, a differentiated picture of how cell-cell contacts influence the mechanical behaviour of cells can be drawn. An intact cell monolayer does not seem to play a pivotal role for the mechanical behaviour of cells. The E-cadherin mediated connection between cells is more important than the *ZO-1* supported one. However, it remains unclear, whether E-cadherin mediated cell-cell junctions or the F-actin-E-cadherin connections are responsible for the results described above.

5.5 The Impact of Clathrin-Mediated Endocytosis

Results concerning Dynasore experiments were published in Ref. [12]. Data and figures are reproduced or adapted from Ref. [12] with permission from The Royal Society of Chemistry.

It is known from the literature that cells use membrane reservoirs, which are destined for endocytosis processes, to buffer membrane tension changes [164,165]. Caveolae, another pit formation for endocytosis besides clathrin coated pits, are used by cells to react to external stresses. However, they exist only on the basolateral side in MDCK II cells and, for this reason, do not have to be considered here [166,167]. In contrast, clathrin coated pits represent an effective and active membrane reservoir on the apical side of MDCK II cells. The interaction with the actin cortex is essential for the functions of these membrane invaginations. In this section, the impact of an enhanced clathrin-mediated endocytosis on the one hand and of a blocked clathrin-mediated endocytosis on the other hand will be discussed. In order to enhance the endocytosis rate, MDCK II cells were genetically modified to express a GTPase-defective mutant of ARF6 (ARF6-Q67L). Altschuler *et al.* found a significantly increased pit formation for cells expressing ARF6-Q67L [99].

Cells stably expressing ARF6-Q67L can be identified by fluorescence microscopy since they also express GFP (Figure 5.37 B). To check the enhanced endocytosis rate, a transferrin uptake test was performed. Cells stably expressing the ARF6 mutant showed a significantly enhanced fluorescence signal for fluorescently marked transferrin (Figure 5.37).

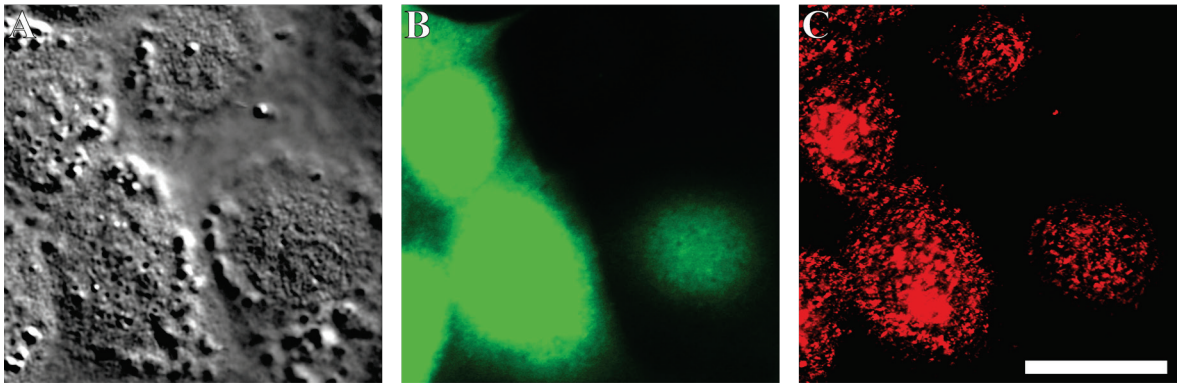

Figure 5.37: ARF6-Q67L expressing MDCK II cells show an enhanced endocytosis rate. A: DIC image. B: Fluorescence image for GFP. C: Fluorescence image for fluorescently labelled transferrin. Scale bar: 15 µm.

Since F-actin is involved in the last step of endocytosis, the scission and internalisation of the mature pit, the F-actin distribution of transfected cells was analysed (Figure 5.38). Cells transfected with a vector encoding the wild type of ARF6 (ARF6-wt) together with GFP is compared to cells transfected with the same vector encoding the mutant (ARF6-Q67L). Thus, a possible influence of the transfection procedure can be excluded. ARF6-wt expressing cells show no differences in the actin distribution compared to untreated cells on the apical as well as on the basal side (Figure 5.38 column 1). For successfully ARF6-Q67L transfected cells (Figure 5.38 column 2) no differences in the actin cytoskeleton were found in comparison to wild type cells. On the apical side the same filigree actin structures originating from microvilli are present. The stress fibre formation on the basal side is unaffected by the genetic manipulation (Figure 5.38 B, C).

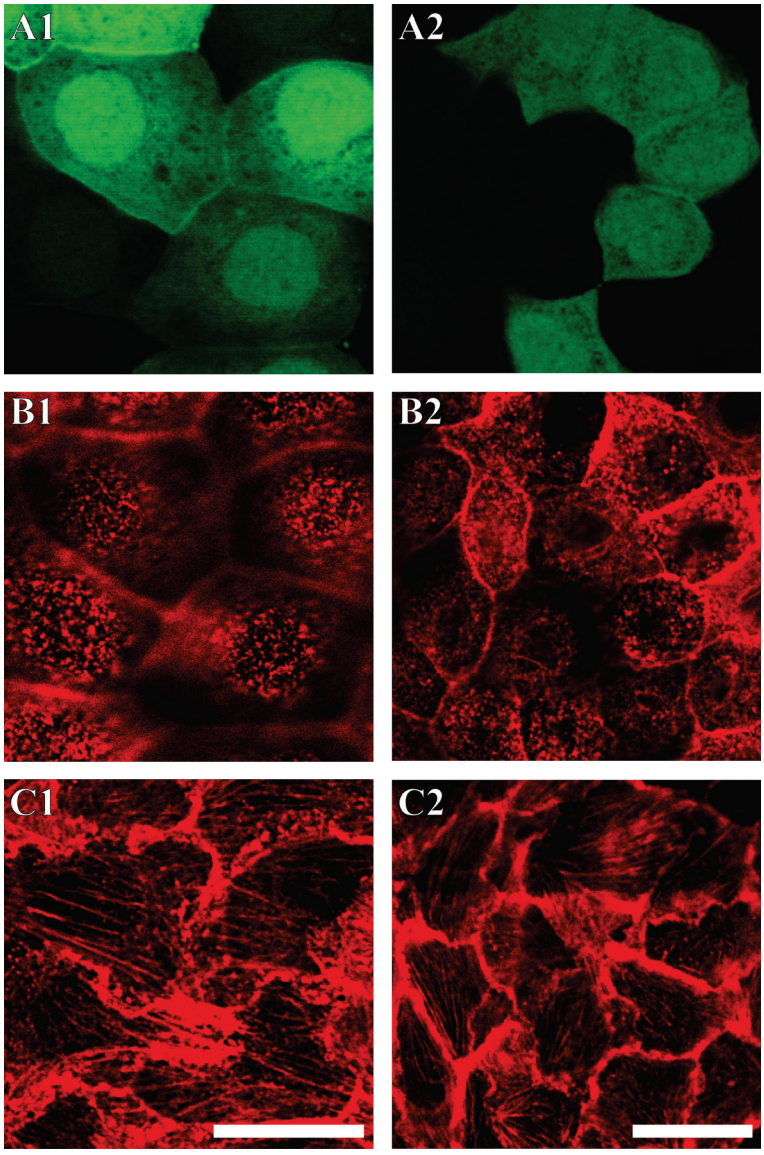

Figure 5.38: Fluorescence images showing the influence of the genetic manipulation on the actin cytoskeleton of MDCK II cells. A: Images for GFP showing successfully transfected cells. B, C: Micrographs for F-actin. The focus was set to the apical (B) and basal (C) side, respectively. 1: Cells expressing ARF6-wt. 2: Cells expressing ARF6-Q67L. Scale Bar: 20 µm

The impact on the topographical properties was analysed by AFM imaging of GDA fixed cells in contact mode. Imaging of a region of the sample, where cells expressing GFP co-exist with cells showing no GFP signal, enables a direct comparison of genetically manipulated cells with cells without any distortion. Cells expressing the ARF6 mutant (Figure 5.39, upper part of the images) show no big difference compared to non-transfected ones (Figure 5.39, lower part of the images). The microvilli distribution is nearly the same as described in section 5.1.

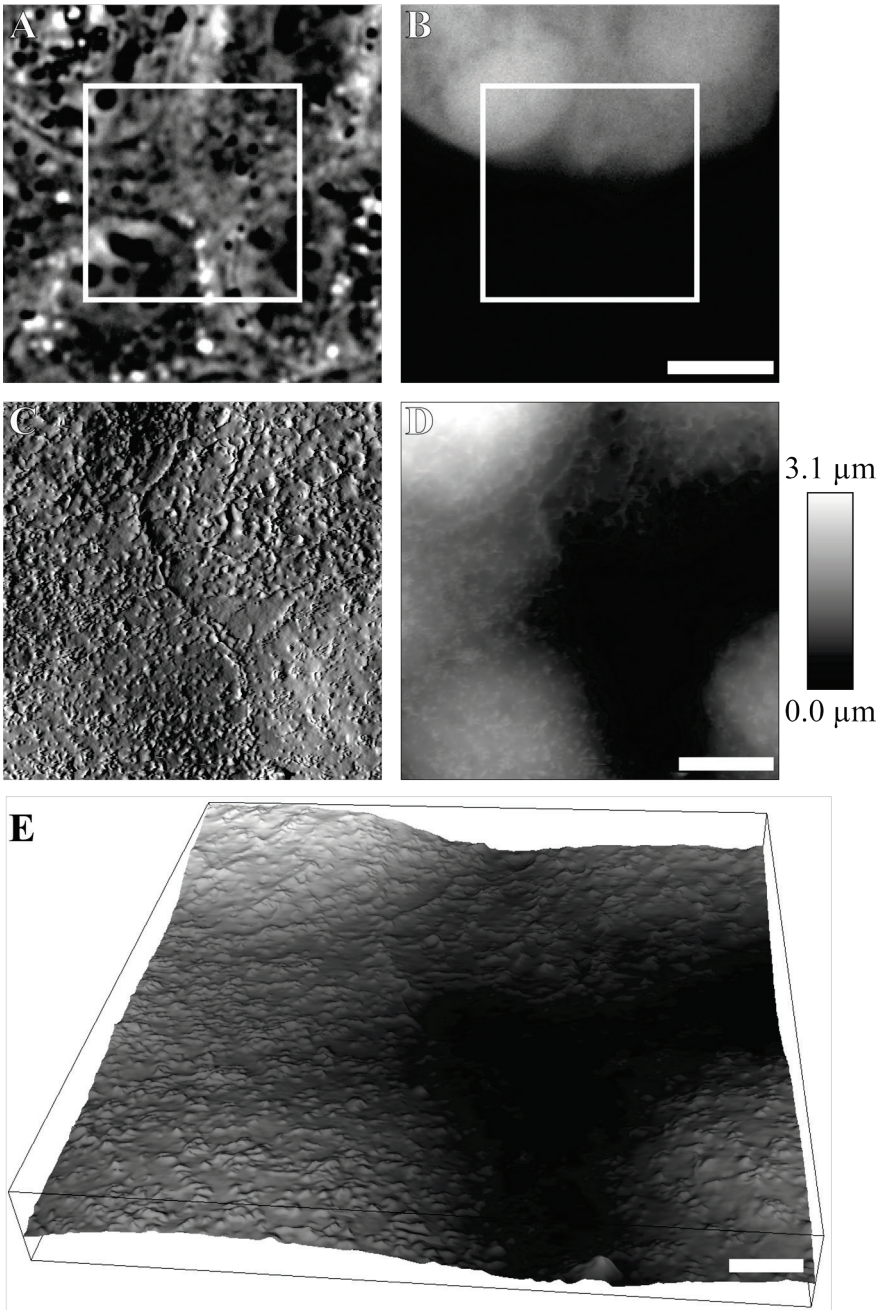

Figure 5.39: Topographical investigation of ARF6-Q67L expressing cells. A: Phase contrast image. B: Fluorescence image for GFP. C: AFM deflection image of the boxed region in A and B. D: AFM height image of the boxed region in A and B. E: Three dimensional AFM image of the region shown in C and D. Scale bar: A, B: 10 µm, C, D: 5 µm, E: 2 µm, box height: 3.5 µm.

Manipulation of the cells for ARF6-Q67L expression provokes no changes in the F-actin distribution and in the topographical properties of MDCK II cells. Thus, there are no reasons to expect that the mechanical properties of ARF6-Q67L expressing cells are significantly altered. Analysis of force-indentation curves revealed that cells

with an enhanced endocytosis rate (ARF6-Q67L) have a lowered tension ($t_0 = (0.396 \pm 0.013)$ mN/m) compared to untreated cells (control: $t_0 = (0.468 \pm 0.013)$ mN/m). The overall tension of cells transfected with the wild type vector was found to be (0.516 ± 0.024) mN/m. The apparent area compressibility modulus drops down from (0.086 ± 0.009) N/m for untreated cells to (0.051 ± 0.009) N/m for cells stably expressing ARF6-Q67L. Compared to control and ARF6-Q67L expressing cells a much lower value was found for cells transfected with the wild type vector ((0.025 ± 0.008) N/m). The membrane tension, a measure of the membrane-cytoskeleton connection, is lowered if the endocytosis rate is enhanced ($t_t = (0.089 \pm 0.005)$ mN/m, control: $t_t = (0.270 \pm 0.007)$ mN/m). For ARF6-wt transfected cells a value of (0.013 ± 0.007) mN/m was found.

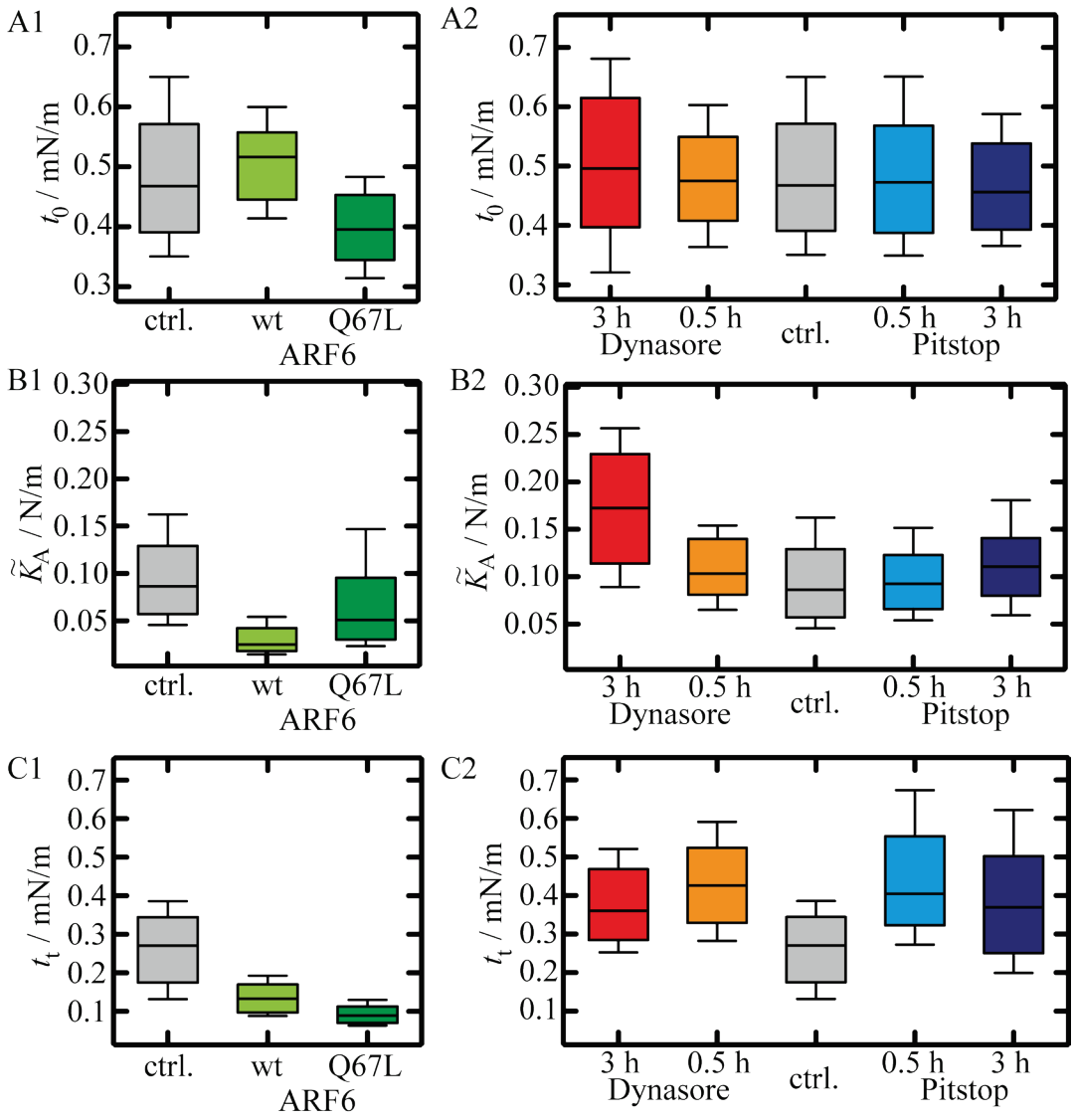

Figure 5.40: **Mechanical investigation of MDCK II cells with altered endocytosis rates. A: Overall tension t_0. B: Apparent area compressibility modulus $\tilde{K}_A$. C: Membrane tension t_t. 1: Box plots for genetically modified cells either co-expressing GFP with ARF6-wt or with ARF6-Q67L in comparison to untreated cells. 2: Box plots for cells treated with Dynasore or Pitstop for different incubation times in comparison to untreated cells. Box plots extend from the 30th to the 70th percentile, whiskers from the 20th to the 80th. A: $n = 367$ (control), 52 (ARF6-wt), 110 (ARF6-Q67L), 103 (3 h Dynasore), 106 (0.5 h Dynasore), 164 (0.5 h Pitstop), 169 (3 h Pitstop) analysed force-indentation curves. B: $n = 364$ (control), 50 (ARF6-wt), 105 (ARF6-Q67L), 97 (3 h Dynasore), 104 (0.5 h Dynasore), 164 (0.5 h Pitstop), 169 (3 h Pitstop) analysed force-indentation curves. C: $n = 520$ (control), 56 (ARF6-wt), 91 (ARF6-Q67L), 182 (3 h Dynasore), 165 (0.5 h Dynasore), 205 (0.5 h Pitstop), 206 (3 h Pitstop) analysed force-retraction curves.**

In order to provoke the opposite effect, i.e. blocking the endocytosis machinery, MDCK II cells were exposed to two different drugs. Dynasore blocks dynamin and arrests clathrin coated pit formation in later states of pit formation [103]. Pitstop interferes with the clathrin terminal domain and thus causes inhibition of endocytosis [104]. The impact of both ways of interference was quantified in a time-resolved way. Generally, the changes in the mechanical behaviour after drug administration are rather small. The overall tension is nearly unaffected by both chemicals. The apparent area compressibility modulus is gradually enhanced during exposition of the cells to Dynasore. After 3 h $\tilde{K}_A$ is nearly doubled. The impact of Pitstop is smaller. After 3 h of drug treatment the apparent area compressibility modulus is only slightly increased. A fast but moderate increase of the membrane tension t_t was found. After 3 h of incubating the cells with either Dynasore or Pitstop, the membrane tension has already dropped down but is still higher than for untreated cells. All mechanical parameters are summarised in Table 5.3.

Table 5.3: Results of force-indentation and force-retraction experiments on MDCK II cells exposed to different drugs according to Figure 5.40. Data shown as median ± SEM.

Stimulus	t_0 / mN/m	$\tilde{K}_A$ / N/m	t_t / mN/m
3 h Dynasore	0.496 ± 0.022	0.172 ± 0.016	0.360 ± 0.016
0.5 h Dynasore	0.475 ± 0.014	0.103 ± 0.008	0.426 ± 0.016
untreated cells	0.468 ± 0.013	0.086 ± 0.009	0.270 ± 0.007
0.5 h Pitstop	0.496 ± 0.022	0.093 ± 0.006	0.404 ± 0.020
3 h Pitstop	0.456 ± 0.011	0.111 ± 0.012	0.369 ± 0.017

5.5.1 Discussion

In this section, the impact of the clathrin-mediated endocytosis on the mechanical behaviour of epithelial cells was investigated. An enhanced endocytosis rate was achieved by a genetic manipulation of MDCK II cells. Cells expressing ARF6-Q67L showed an increased endocytosis rate confirmed by a transferrin uptake test. These results agree with results reported in the literature [99]. No visible impact on the F-actin distribution was found. The cellular topography is unaffected by the genetic modification. The overall tension drops slightly if the endocytosis rate is enhanced. Taken together with the lowered membrane tension, one can assume that a fast rearrangement of the F-actin and a weaker plasma membrane-cytoskeleton attachment is necessary to internalise a greater number of mature pits. F-actin is necessary in this last step of endocytosis. Thus, a more dynamic cytoskeleton is probably the reason for the lowered tension values found here. It has to be kept in mind, however, that the membrane tension for cells transfected with ARF6-wt is also lowered. Therefore, the effect of an enhanced endocytosis should not be overestimated. On the other hand, an enhanced endocytosis rate is accompanied by more membrane invaginations at the apical membrane surface. These structures are not supported by any membrane-cytoskeleton connection during the first endocytosis steps. The membrane is therefore looser and membrane reservoirs can be recruited with less energy penalty. The apparent area compressibility modulus for ARF6-wt as well as for ARF6-Q67L transfected cells was found to be lower than for untreated cells. This does not allow for any reliable conclusion to be drawn. However, lower $\tilde{K}_A$ values show an enhanced excess surface area in general.

Interestingly, after provoking the opposite effect, i.e. a blocked clathrin-mediated endocytosis, the cells do not show the opposite tendency in all mechanical parameters. Contrary to ARF6-Q67L expressing cells the overall tension is not influenced by Dynasore and Pitstop. In contrast, the membrane tension is enhanced regardless of applying Dynasore or Pitstop. The effect becomes apparent very fast. According to eq. (3.8) it might be reasonable to assume that both drugs block endocytosis in a state where F-actin is already assembled to the pit. Von Kleist *et al*. reported that Pitstop interferes with the clathrin terminal domain and thus arrests the endocytosis machinery at different stages [104]. Our results support their conclusion that some part of the pits are arrested, when F-actin is already

assembled to the pit. Another hint for the existence of this connection is the increased apparent area compressibility modulus due to drug treatments with Dynasore or Pitstop. When the pit is trapped by F-actin, it is more costly to use this excess membrane material to buffer deeper indentation with an external probe. Mayor and Sinha *et al.* reported that cells buffer changes in tension by caveolae disassembly [164,165]. Our study shows that cells cannot use clathrin-coated pits to buffer indentation with an AFM tip if the endocytosis is blocked. It can therefore be concluded that clathrin-coated pits play to a certain extent the same role in MDCK II cells as caveolae in other types of cells.

6 Summary

The aim of this study was to quantitatively understand how tension homeostasis is realised in epithelial cells by surface area regulation. To answer this question, the study focussed on different cellular compartments and proteins. In a first approach the role of the important structural protein actin as well as the membrane-cytoskeleton interface were investigated. Furthermore, the impact of cell-cell contacts on the mechanical behaviour was elucidated. In a last step, a possible impact of the clathrin-mediated endocytosis on tension homeostasis was scrutinised. This is a process in which excess membrane area, the cytoskeleton, and rearrangement of the membrane-cytoskeleton attachment are involved.

It could be clearly shown that an intact cytoskeleton is of paramount importance for the mechanical behaviour of epithelial cells. Both degradation and reinforcement lead to substantial changes of the cellular topography and the mechanical behaviour in response to indentation with an external probe.

Furthermore, this study demonstrated that an intact plasma membrane-cytoskeleton attachment is inevitable for tension maintenance of MDCK II cells. Interference with the linker molecule of this interface on the apical cell side, namely ezrin, and with the catenin-cadherin mediated connection on the lateral cell side lead to substantial changes, not only in the morphology of the cell but also in the mechanical behaviour. In addition, interference with the clathrin-mediated endocytosis pathway changes the mechanical behaviour of epithelial cells. However, the impact on cellular mechanics is rather small.

Interfering with the integrity of a cell monolayer by *ZO-1* depletion demonstrated that intercellular connections play only a minor role for tension generation and maintenance.

In summary this study provides evidence that the cytoskeleton and the membrane-cytoskeleton attachment are the major regulators of the mechanical behaviour of the apical cell side in epithelial cells.

7 References

[1] Jaalouk, D.E. and Lammerding, J. (2009): *Mechanotransduction gone awry.* Nat. Rev. Mol. Cell Biol., **10** *(1)*, 63-73.

[2] Suresh, S. (2007): *Biomechanics and biophysics of cancer cells.* Acta Biomater., **3** *(4)*, 413-438.

[3] Hoffman, B.D. and Crocker, J.C. (2009): *Cell mechanics: dissecting the physical responses of cells to force.* Annu. Rev. Biomed. Eng., **11**, 259-288.

[4] Mitchison, J.M. and Swann, M.M. (1954): *The Mechanical Properties of the Cell Surface.* I. The Cell Elastimeter, **31** *(3)*, 443-460.

[5] Rand, R.P. and Burton, A.C. (1964): *Mechanical Properties of the Red Cell Membrane: I. Membrane Stiffness and Intracellular Pressure.* Biophys. J., **4** *(2)*, 115-135.

[6] Rand, R.P. (1964): *Mechanical Properties of the Red Cell Membrane: II. Viscoelastic Breakdown of the Membrane.* Biophys. J., **4** *(4)*, 303-316.

[7] Hochmuth, R.M. (2000): *Micropipette aspiration of living cells.* J. Biomech., **33** *(1)*, 15-22.

[8] Butt, H.J., Cappella, B., and Kappl, M. (2005): *Force measurements with the atomic force microscope: Technique, interpretation and applications.* Surf. Sci. Rep., **59** *(1-6)*, 1-152.

[9] Santos, N.C. and Castanho, M.A.R.B. (2004): *An overview of the biophysical applications of atomic force microscopy.* Biophys. Chem., **107** *(2)*, 133-149.

[10] Sen, S., Subramanian, S., and Discher, D.E. (2005): *Indentation and adhesive probing of a cell membrane with AFM: theoretical model and experiments.* Biophys. J., **89** *(5)*, 3203-3213.

[11] Rosenbluth, M.J., Lam, W.A., and Fletcher, D.A. (2006): *Force microscopy of nonadherent cells: a comparison of leukemia cell deformability.* Biophys. J., **90** *(8)*, 2994-3003.

[12] Pietuch, A., Brückner, B.R., Fine, T., Mey, I., and Janshoff, A. (2013): *Elastic properties of cells in the context of confluent cell monolayers: impact of tension and surface area regulation.* Soft Matter, **9** *(48)*, 11490-11502.

[13] Pietuch, A.: *Membrane mechanics governs cell mechanics in epithelial cell: how surface area regulation ensures tension homeostasis*. Ph.D. Thesis, Georg-August-University, Göttingen, Germany, 2012.

[14] Carl, P. and Schillers, H. (2008): *Elasticity measurement of living cells with an atomic force microscope: data acquisition and processing.* Pflugers Arch., **457** *(2)*, 551-559.

[15] Sheetz, M.P. and Dai, J. (1996): *Modulation of membrane dynamics and cell motility by membrane tension.* Trends Cell Biol., **6** *(3)*, 85-89.

[16] Houk, A.R., Jilkine, A., Mejean, C.O. *et al.* (2012): *Membrane tension maintains cell polarity by confining signals to the leading edge during neutrophil migration.* Cell, **148** *(1-2)*, 175-188.

[17] Togo, T., Krasieva, T.B., and Steinhardt, R.A. (2000): *A decrease in membrane tension precedes successful cell-membrane repair.* Mol. Biol. Cell, **11** *(12)*, 4339-4346.

[18] Pietuch, A., Brückner, B.R., and Janshoff, A. (2013): *Membrane tension homeostasis of epithelial cells through surface area regulation in response to osmotic stress.* Biochim. Biophys. Acta, **1833** *(3)*, 712-722.

[19] Gauthier, N.C., Fardin, M.A., Roca-Cusachs, P., and Sheetz, M.P. (2011): *Temporary increase in plasma membrane tension coordinates the activation of exocytosis and contraction during cell spreading.* Proc. Natl. Acad. Sci. USA, **108** *(35)*, 14467-14472.

[20] Raucher, D. and Sheetz, M.P. (2000): *Cell spreading and lamellipodial extension rate is regulated by membrane tension.* J. Cell Biol., **148** *(1)*, 127-136.

[21] Pietuch, A. and Janshoff, A. (2013): *Mechanics of spreading cells probed by atomic force microscopy.* Open Biol., **3** *(7)*, 130084.

[22] Zhu, L., Crothers, J., Jr., Zhou, R., and Forte, J.G. (2010): *A possible mechanism for ezrin to establish epithelial cell polarity.* Am. J. Physiol. Cell Physiol., **299** *(2)*, C431-443.

[23] Braunger, J.A., Brückner, B.R., Nehls, S. *et al.* (2014): *Phosphatidylinositol 4,5-Bisphosphate Alters the Number of Attachment Sites between Ezrin and Actin Filaments: A COLLOIDAL PROBE STUDY.* J. Biol. Chem., **289** *(14)*, 9833-9843.

[24] Diz-Munoz, A., Krieg, M., Bergert, M. *et al.* (2010): *Control of directed cell migration in vivo by membrane-to-cortex attachment.* PLoS Biol., **8** *(11)*, e1000544.

[25] Nambiar, R., McConnell, R.E., and Tyska, M.J. (2009): *Control of cell membrane tension by myosin-I.* Proc. Natl. Acad. Sci. USA, **106** *(29)*, 11972-11977.

[26] Liu, Y., Belkina, N.V., Park, C. *et al.* (2012): *Constitutively active ezrin increases membrane tension, slows migration, and impedes endothelial transmigration of lymphocytes in vivo in mice.* Blood, **119** *(2)*, 445-453.

[27] Morris, C.E. and Homann, U. (2001): *Cell Surface Area Regulation and Membrane Tension.* J. Membr. Biol., **179** *(2)*, 79-102.

[28] Dai, J., Ting-Beall, H.P., and Sheetz, M.P. (1997): *The secretion-coupled endocytosis correlates with membrane tension changes in RBL 2H3 cells.* J. Gen. Physiol., **110** *(1)*, 1-10.

[29] Dai, J. and Sheetz, M.P. (1995): *Regulation of endocytosis, exocytosis, and shape by membrane tension.* Cold Spring Harb. Symp. Quant. Biol., **60**, 567-571.

[30] Dai, J. and Sheetz, M.P. (1999): *Membrane tether formation from blebbing cells.* Biophys. J., **77** *(6)*, 3363-3370.

[31] Gauthier, N.C., Masters, T.A., and Sheetz, M.P. (2012): *Mechanical feedback between membrane tension and dynamics.* Trends Cell Biol., **22** *(10)*, 527-535.

[32] Brückner, B.R., Pietuch, A., Nehls, S., Rother, J., and Janshoff, A. (2015): *Ezrin is a Major Regulator of Membrane Tension in Epithelial Cells.* Sci. Rep., **5**, 14700.

[33] Dukes, J.D., Fish, L., Richardson, J.D. *et al.* (2011): *Functional ESCRT machinery is required for constitutive recycling of claudin-1 and maintenance of polarity in vertebrate epithelial cells.* Mol. Biol. Cell, **22** *(17)*, 3192-3205.

[34] Public Health England, European Collection of Authenticated Cell Cultures (ECACC), available from: https://www.phe-culturecollections.org.uk/collections/ecacc.aspx, access date: 22.03.2016.

[35] American Type Culture Collection, ATCC, available from: www.lgcstandards-atcc.org/, access date: 22.03.2016.

[36] Madin, S.H. and Darby, N.B., Jr. (1958): *Established kidney cell lines of normal adult bovine and ovine origin.* Proc. Soc. Exp. Biol. Med., **98** *(3)*, 574-576.

[37] Gaush, C.R., Hard, W.L., and Smith, T.F. (1966): *Characterization of an established line of canine kidney cells (MDCK).* Proc. Soc. Exp. Biol. Med., **122** *(3)*, 931-935.

[38] Valentich, J.D. (1981): *Morphological similarities between the dog kidney cell line MDCK and the mammalian cortical collecting tubule.* Ann. N. Y. Acad. Sci., **372**, 384-405.

[39] Richardson, J.C., Scalera, V., and Simmons, N.L. (1981): *Identification of two strains of MDCK cells which resemble separate nephron tubule segments.* Biochim. Biophys. Acta, **673** *(1)*, 26-36.

[40] Barker, G. and Simmons, N.L. (1981): *Identification of two strains of cultured canine renal epithelial cells (MDCK cells) which display entirely different physiological properties.* Q. J. Exp. Physiol., **66** *(1)*, 61-72.

[41] Public Health England, European Collection of Authenticated Cell Cultures (ECACC), available from: https://www.phe-culturecollections.org.uk/products/celllines/generalcell/detail.jsp?refId=00062106&collection=ecacc_gc, access date: 22.03.2016.

[42] van Meer, G., Voelker, D.R., and Feigenson, G.W. (2008): *Membrane lipids: where they are and how they behave.* Nat. Rev. Mol. Cell Biol., **9** *(2)*, 112-124.

[43] Alberts, B., Johnson, A., Lewis, J. *et al.*: *Molecular Biology of the Cell.* 5th edition, New York, 2008.

[44] Kawai, K., Fujita, M., and Nakao, M. (1974): *Lipid components of two different regions of an intestinal epithelial cell membrane of mouse.* Biochim. Biophys. Acta, **369** *(2)*, 222-233.

[45] Sampaio, J.L., Gerl, M.J., Klose, C. *et al.* (2011): *Membrane lipidome of an epithelial cell line.* Proc. Natl. Acad. Sci. USA, **108** *(5)*, 1903-1907.

[46] Fehon, R.G., McClatchey, A.I., and Bretscher, A. (2010): *Organizing the cell cortex: the role of ERM proteins.* Nat. Rev. Mol. Cell Biol., **11** *(4)*, 276-287.

[47] Berryman, M., Franck, Z., and Bretscher, A. (1993): *Ezrin is concentrated in the apical microvilli of a wide variety of epithelial cells whereas moesin is found primarily in endothelial cells.* J. Cell Sci., **105**, 1025-1043.

[48] Woodward, A.M. and Crouch, D.H. (2001): *Cellular distributions of the ERM proteins in MDCK epithelial cells: regulation by growth and cytoskeletal integrity.* Cell Biol. Int., **25** *(3)*, 205-213.

[49] Gary, R. and Bretscher, A. (1995): *Ezrin self-association involves binding of an N-terminal domain to a normally masked C-terminal domain that includes the F-actin binding site.* Mol. Biol. Cell, **6** *(8)*, 1061-1075.

[50] Simons, P.C., Pietromonaco, S.F., Reczek, D., Bretscher, A., and Elias, L. (1998): *C-Terminal Threonine Phosphorylation Activates ERM Proteins to Link the Cell's Cortical Lipid Bilayer to the Cytoskeleton.* Biochem. Biophys. Res. Commun., **253** *(3)*, 561-565.

[51] Zhu, L., Liu, Y., and Forte, J.G. (2005): *Ezrin oligomers are the membrane-bound dormant form in gastric parietal cells.* Am. J. Physiol. Cell Physiol., **288** *(6)*, C1242-1254.

[52] Bosk, S., Braunger, J.A., Gerke, V., and Steinem, C. (2011): *Activation of F-actin binding capacity of ezrin: synergism of PIP(2) interaction and phosphorylation.* Biophys. J., **100** *(7)*, 1708-1717.

[53] Niggli, V., Andreoli, C., Roy, C., and Mangeat, P. (1995): *Identification of a phosphatidylinositol-4,5-bisphosphate-binding domain in the N-terminal region of ezrin.* FEBS Lett., **376** *(3)*, 172-176.

[54] Bretscher, A., Edwards, K., and Fehon, R.G. (2002): *ERM proteins and merlin: integrators at the cell cortex.* Nat. Rev. Mol. Cell Biol., **3** *(8)*, 586-599.

[55] Hunter, K.W. (2004): *Ezrin, a key component in tumor metastasis.* Trends Mol. Med., **10** *(5)*, 201-204.

[56] Ren, L., Hong, S.H., Cassavaugh, J. *et al.* (2009): *The actin-cytoskeleton linker protein ezrin is regulated during osteosarcoma metastasis by PKC.* Oncogene, **28** *(6)*, 792-802.

[57] Bao, G. and Suresh, S. (2003): *Cell and molecular mechanics of biological materials.* Nature Materials, **2** *(11)*, 715-725.

[58] Zhu, C., Bao, G., and Wang, N. (2000): *Cell mechanics: Mechanical response, cell adhesion, and molecular deformation.* Annu. Rev. Biomed. Eng., **2**, 189-226.

[59] Paluch, E., Sykes, C., Prost, J., and Bornens, M. (2006): *Dynamic modes of the cortical actomyosin gel during cell locomotion and division.* Trends Cell Biol., **16** *(1)*, 5-10.

[60] Apodaca, G. (2002): *Modulation of membrane traffic by mechanical stimuli.* Am. J. Physiol. Renal Physiol., **282** *(2)*, F179-190.

[61] Sept, D., Elcock, A.H., and McCammon, J.A. (1999): *Computer simulations of actin polymerization can explain the barbed-pointed end asymmetry.* J. Mol. Biol., **294** *(5)*, 1181-1189.

[62] Pollard, T.D., Blanchoin, L., and Mullins, R.D. (2000): *Molecular mechanisms controlling actin filament dynamics in nonmuscle cells.* Annu. Rev. Biophys., **29**, 545-576.

[63] Pollard, T.D. (1986): *Rate constants for the reactions of ATP- and ADP-actin with the ends of actin filaments.* J. Cell Biol., **103** *(6 Pt 2)*, 2747-2754.

[64] Blanchoin, L., Boujemaa-Paterski, R., Sykes, C., and Plastino, J. (2014): *Actin dynamics, architecture, and mechanics in cell motility.* Physiol. Rev., **94** *(1)*, 235-263.

[65] Almo, S.C., Pollard, T.D., Way, M., and Lattman, E.E. (1994): *Purification, characterization and crystallization of Acanthamoeba profilin expressed in Escherichia coli.* J. Mol. Biol., **236** *(3)*, 950-952.

[66] Vinson, V.K., De La Cruz, E.M., Higgs, H.N., and Pollard, T.D. (1998): *Interactions of Acanthamoeba Profilin with Actin and Nucleotides Bound to Actin.* Biochemistry, **37** *(31)*, 10871-10880.

[67] Pring, M., Weber, A., and Bubb, M.R. (1992): *Profilin-actin complexes directly elongate actin filaments at the barbed end.* Biochemistry, **31** *(6)*, 1827-1836.

[68] Morone, N., Fujiwara, T., Murase, K. *et al.* (2006): *Three-dimensional reconstruction of the membrane skeleton at the plasma membrane interface by electron tomography.* J. Cell Biol., **174** *(6)*, 851-862.

[69] Mooseker, M.S. and Tilney, L.G. (1975): *Organization of an actin filament-membrane complex. Filament polarity and membrane attachment in the microvilli of intestinal epithelial cells.* J. Cell Biol., **67** *(3)*, 725-743.

[70] Bretscher, A. (1991): *Microfilament structure and function in the cortical cytoskeleton.* Annu. Rev. Cell Biol., **7**, 337-374.

[71] Hotulainen, P. and Lappalainen, P. (2006): *Stress fibers are generated by two distinct actin assembly mechanisms in motile cells.* J. Cell Biol., **173** *(3)*, 383-394.

[72] Kanchanawong, P., Shtengel, G., Pasapera, A.M. *et al.* (2010): *Nanoscale architecture of integrin-based cell adhesions.* Nature, **468** *(7323)*, 580-584.

[73] Smutny, M., Cox, H.L., Leerberg, J.M. *et al.* (2010): *Myosin II isoforms identify distinct functional modules that support integrity of the epithelial zonula adherens.* Nat. Cell Biol., **12** *(7)*, 696-702.

[74] Balda, M.S. and Matter, K. (2008): *Tight junctions at a glance.* J. Cell Sci., **121** *(Pt 22)*, 3677-3682.

[75] Meyer, R.K. and Aebi, U. (1990): *Bundling of actin filaments by alpha-actinin depends on its molecular length.* J. Cell Biol., **110** *(6)*, 2013-2024.

[76] Tyska, M.J. and Warshaw, D.M. (2002): *The myosin power stroke.* Cell Motil. Cytoskeleton, **51** *(1)*, 1-15.

[77] Burton, K. and Taylor, D.L. (1997): *Traction forces of cytokinesis measured with optically modified elastic substrata.* Nature, **385** *(6615)*, 450-454.

[78] Humphrey, D., Duggan, C., Saha, D., Smith, D., and Kas, J. (2002): *Active fluidization of polymer networks through molecular motors.* Nature, **416** *(6879)*, 413-416.

[79] Carvalho, K., Lemiere, J., Faqir, F. *et al.* (2013): *Actin polymerization or myosin contraction: two ways to build up cortical tension for symmetry breaking.* Philos. Trans. R. Soc. Lond., B, Biol. Sci., **368** *(1629)*, 20130005.

[80] Martin, A.C., Kaschube, M., and Wieschaus, E.F. (2009): *Pulsed contractions of an actin-myosin network drive apical constriction.* Nature, **457** *(7228)*, 495-499.

[81] Lee, J.Y. and Harland, R.M. (2007): *Actomyosin contractility and microtubules drive apical constriction in Xenopus bottle cells.* Dev. Biol., **311** *(1)*, 40-52.

[82] Hildebrand, J.D. (2005): *Shroom regulates epithelial cell shape via the apical positioning of an actomyosin network.* J. Cell Sci., **118** *(Pt 22)*, 5191-5203.

[83] Vasquez, C.G., Tworoger, M., and Martin, A.C. (2014): *Dynamic myosin phosphorylation regulates contractile pulses and tissue integrity during epithelial morphogenesis.* J. Cell Biol., **206** *(3)*, 435-450.

[84] Furuse, M., Hata, M., Furuse, K. *et al.* (2002): *Claudin-based tight junctions are crucial for the mammalian epidermal barrier: a lesson from claudin-1–deficient mice.* J. Cell Biol., **156** *(6)*, 1099-1111.

[85] Shin, K., Fogg, V.C., and Margolis, B. (2006): *Tight Junctions and Cell Polarity.* Annu. Rev. Cell Dev. Biol., **22** *(1)*, 207-235.

[86] Van Itallie, C.M., Fanning, A.S., Bridges, A., and Anderson, J.M. (2009): *ZO-1 stabilizes the tight junction solute barrier through coupling to the perijunctional cytoskeleton.* Mol. Biol. Cell, **20** *(17)*, 3930-3940.

[87] Shapiro, L., Fannon, A.M., Kwong, P.D. *et al.* (1995): *Structural basis of cell-cell adhesion by cadherins.* Nature, **374** *(6520)*, 327-337.

[88] Ozawa, M., Engel, J., and Kemler, R. (1990): *Single amino acid substitutions in one Ca2+ binding site of uvomorulin abolish the adhesive function.* Cell, **63** *(5)*, 1033-1038.

[89] Pokutta, S., Herrenknecht, K., Kemler, R., and Engel, J. (1994): *Conformational changes of the recombinant extracellular domain of E-cadherin upon calcium binding.* Eur. J. Biochem., **223** *(3)*, 1019-1026.

[90] Pokutta, S. and Weis, W.I. (2007): *Structure and mechanism of cadherins and catenins in cell-cell contacts.* Annu. Rev. Cell Dev. Biol., **23**, 237-261.

[91] McMahon, H.T. and Gallop, J.L. (2005): *Membrane curvature and mechanisms of dynamic cell membrane remodelling.* Nature, **438** *(7068)*, 590-596.

[92] Mayor, S. and Pagano, R.E. (2007): *Pathways of clathrin-independent endocytosis.* Nat. Rev. Mol. Cell Biol., **8** *(8)*, 603-612.

[93] Kirkham, M. and Parton, R.G. (2005): *Clathrin-independent endocytosis: new insights into caveolae and non-caveolar lipid raft carriers.* Biochim. Biophys. Acta, **1746** *(3)*, 349-363.

[94] Rosenbluth, J. and Wissig, S.L. (1964): *The Distribution of Exogenous Ferritin in Toad Spinal Ganglia and the Mechanism of Its Uptake by Neurons.* J. Cell Biol., **23**, 307-325.

[95] Roth, T.F. and Porter, K.R. (1964): *Yolk Protein Uptake in the Oocyte of the Mosquito Aedes Aegypti. L.* J. Cell Biol., **20**, 313-332.

[96] Sorkin, A. (2004): *Cargo recognition during clathrin-mediated endocytosis: a team effort.* Curr. Opin. Cell Biol., **16** *(4)*, 392-399.

[97] Donaldson, J.G. and Honda, A. (2005): *Localization and function of Arf family GTPases.* Biochem. Soc. Trans., **33** *(Pt 4)*, 639-642.

[98] Nie, Z., Hirsch, D.S., and Randazzo, P.A. (2003): *Arf and its many interactors.* Curr. Opin. Cell Biol., **15** *(4)*, 396-404.

[99] Altschuler, Y., Liu, S., Katz, L. *et al.* (1999): *ADP-ribosylation factor 6 and endocytosis at the apical surface of Madin-Darby canine kidney cells.* J. Cell Biol., **147** *(1)*, 7-12.

[100] Hyman, T., Shmuel, M., and Altschuler, Y. (2006): *Actin is required for endocytosis at the apical surface of Madin-Darby canine kidney cells where ARF6 and clathrin regulate the actin cytoskeleton.* Mol. Biol. Cell, **17** *(1)*, 427-437.

[101] Palacios, F., Price, L., Schweitzer, J., Collard, J.G., and D'Souza-Schorey, C. (2001): *An essential role for ARF6-regulated membrane traffic in adherens junction turnover and epithelial cell migration.* EMBO J., **20** *(17)*, 4973-4986.

[102] Palacios, F., Schweitzer, J.K., Boshans, R.L., and D'Souza-Schorey, C. (2002): *ARF6-GTP recruits Nm23-H1 to facilitate dynamin-mediated endocytosis during adherens junctions disassembly.* Nat. Cell Biol., **4** *(12)*, 929-936.

[103] Macia, E., Ehrlich, M., Massol, R. *et al.* (2006): *Dynasore, a cell-permeable inhibitor of dynamin.* Dev. Cell, **10** *(6)*, 839-850.

[104] von Kleist, L., Stahlschmidt, W., Bulut, H. *et al.* (2011): *Role of the clathrin terminal domain in regulating coated pit dynamics revealed by small molecule inhibition.* Cell, **146** *(3)*, 471-484.

[105] Binnig, G., Rohrer, H., Gerber, C., and Weibel, E. (1982): *Surface Studies by Scanning Tunneling Microscopy.* Phys. Rev. Lett., **49** *(1)*, 57-61.

[106] Binnig, G., Quate, C.F., and Gerber, C. (1986): *Atomic Force Microscope.* Phys. Rev. Lett., **56** *(9)*, 930-933.

[107] Binnig, G. and Rohrer, H. (1987): *Scanning Tunneling Microscopy - from Birth to Adolescence.* Rev. Mod. Phys., **59** *(3)*, 615-625.

[108] Janshoff, A. and Steinem, C. (2015): *Mechanics of lipid bilayers: What do we learn from pore-spanning membranes?* Biochim. Biophys. Acta, **1853** *(11 Pt B)*, 2977-2983.

[109] Brückner, B.R. and Janshoff, A. (2015): *Elastic properties of epithelial cells probed by atomic force microscopy.* Biochim. Biophys. Acta, **1853** *(11 Pt B)*, 3075-82.

[110] Hutter, J.L. and Bechhoefer, J. (1993): *Calibration of atomic‐force microscope tips.* Rev. Sci. Instrum., **64** *(7)*, 1868-1873.

[111] Naeem, S., Liu, Y., Nie, H.-Y., Lau, W.M., and Yang, J. (2008): *Revisiting atomic force microscopy force spectroscopy sensitivity for single molecule studies.* J. Appl. Phys., **104** *(11)*, 114504.

[112] Butt, H.J. and Jaschke, M. (1995): *Calculation of Thermal Noise in Atomic-Force Microscopy.* Nanotechnology, **6** *(1)*, 1-7.

[113] Sneddon, I.N. (1965): *The relation between load and penetration in the axisymmetric boussinesq problem for a punch of arbitrary profile.* Int. J. Eng. Sci., **3** *(1)*, 47-57.

[114] Briscoe, B.J., Sebastian, K.S., and Adams, M.J. (1994): *The effect of indenter geometry on the elastic response to indentation.* J. Phys. D: Appl. Phys., **27** *(6)*, 1156.

[115] Costa, K.D. and Yin, F.C. (1999): *Analysis of indentation: implications for measuring mechanical properties with atomic force microscopy.* J. Biomech. Eng., **121** *(5)*, 462-471.

[116] Radmacher, M. (1997): *Measuring the elastic properties of biological samples with the AFM.* IEEE Eng. Med. Biol. Mag., **16** *(2)*, 47-57.

[117] Nikkhah, M., Strobl, J.S., De Vita, R., and Agah, M. (2010): *The cytoskeletal organization of breast carcinoma and fibroblast cells inside three dimensional (3-D) isotropic silicon microstructures.* Biomaterials, **31** *(16)*, 4552-4561.

[118] Cross, S.E., Jin, Y.S., Tondre, J. *et al.* (2008): *AFM-based analysis of human metastatic cancer cells.* Nanotechnology, **19** *(38)*, 384003.

[119] Domke, J. and Radmacher, M. (1998): *Measuring the Elastic Properties of Thin Polymer Films with the Atomic Force Microscope.* Langmuir, **14** *(12)*, 3320-3325.

[120] Hochmuth, R.M., Wiles, H.C., Evans, E.A., and McCown, J.T. (1982): *Extensional flow of erythrocyte membrane from cell body to elastic tether. II. Experiment.* Biophys. J., **39** *(1)*, 83-89.

[121] Heinrich, V. and Waugh, R.E. (1996): *A piconewton force transducer and its application to measurement of the bending stiffness of phospholipid membranes.* Ann. Biomed. Eng., **24** *(5)*, 595-605.

[122] Brochard-Wyart, F., Borghi, N., Cuvelier, D., and Nassoy, P. (2006): *Hydrodynamic narrowing of tubes extruded from cells.* Proc. Natl. Acad. Sci. USA, **103** *(20)*, 7660-7663.

[123] Sheetz, M.P. (2001): *Cell control by membrane-cytoskeleton adhesion.* Nat. Rev. Mol. Cell Biol., **2** *(5)*, 392-6.

[124] Krieg, M., Helenius, J., Heisenberg, C.P., and Muller, D.J. (2008): *A bond for a lifetime: employing membrane nanotubes from living cells to determine receptor-ligand kinetics.* Angew. Chem. Int. Ed. Engl., **47** *(50)*, 9775-9777.

[125] Giaever, I. and Keese, C.R. (1984): *Monitoring fibroblast behavior in tissue culture with an applied electric field.* Proc. Natl. Acad. Sci. USA, **81** *(12)*, 3761-3764.

[126] Giaever, I. and Keese, C.R. (1993): *A morphological biosensor for mammalian cells.* Nature, **366** *(6455)*, 591-592.

[127] Xiao, C. and Luong, J.H. (2003): *On-line monitoring of cell growth and cytotoxicity using electric cell-substrate impedance sensing (ECIS).* Biotechnol. Prog., **19** *(3)*, 1000-1005.

[128] Lo, C.M., Keese, C.R., and Giaever, I. (1995): *Impedance analysis of MDCK cells measured by electric cell-substrate impedance sensing.* Biophys. J., **69** *(6)*, 2800-2807.

[129] Lo, C.M. and Ferrier, J. (1998): *Impedance analysis of fibroblastic cell layers measured by electric cell-substrate impedance sensing.* Phys. Rev. E, **57** *(6)*, 6982-6987.

[130] Elbashir, S.M., Lendeckel, W., and Tuschl, T. (2001): *RNA interference is mediated by 21- and 22-nucleotide RNAs.* Genes Dev., **15** *(2)*, 188-200.

[131] Elbashir, S.M., Harborth, J., Lendeckel, W. *et al.* (2001): *Duplexes of 21-nucleotide RNAs mediate RNA interference in cultured mammalian cells.* Nature, **411** *(6836)*, 494-498.

[132] Ketting, R.F., Fischer, S.E., Bernstein, E. *et al.* (2001): *Dicer functions in RNA interference and in synthesis of small RNA involved in developmental timing in C. elegans.* Genes Dev., **15** *(20)*, 2654-2659.

[133] Bernstein, E., Caudy, A.A., Hammond, S.M., and Hannon, G.J. (2001): *Role for a bidentate ribonuclease in the initiation step of RNA interference.* Nature, **409** *(6818)*, 363-366.

[134] Dykxhoorn, D.M., Novina, C.D., and Sharp, P.A. (2003): *Killing the messenger: short RNAs that silence gene expression.* Nat. Rev. Mol. Cell Biol., **4** *(6)*, 457-467.

[135] Zernike, F. (1942): *Phase contrast, a new method for the microscopic observation of transparent objects.* Physica, **9** *(7)*, 686-698.

[136] Zernike, F. (1942): *Phase contrast, a new method for the microscopic observation of transparent objects part II.* Physica, **9** *(10)*, 974-986.

[137] Riedl, J., Crevenna, A.H., Kessenbrock, K. *et al.* (2008): *Lifeact: a versatile marker to visualize F-actin.* Nat. Meth., **5** *(7)*, 605-607.

[138] Hertz, H. (1882): *Ueber die Berührung fester elastischer Körper.* J. Reine Angew. Math., **1882** *(92)*, 156-171.

[139] Mathur, A.B., Collinsworth, A.M., Reichert, W.M., Kraus, W.E., and Truskey, G.A. (2001): *Endothelial, cardiac muscle and skeletal muscle exhibit different viscous and elastic properties as determined by atomic force microscopy.* J. Biomech., **34** *(12)*, 1545-1553.

[140] Yarmola, E.G., Somasundaram, T., Boring, T.A., Spector, I., and Bubb, M.R. (2000): *Actin-latrunculin A structure and function. Differential modulation of actin-binding protein function by latrunculin A.* J. Biol. Chem., **275** *(36)*, 28120-7.

[141] Bubb, M.R., Senderowicz, A.M., Sausville, E.A., Duncan, K.L., and Korn, E.D. (1994): *Jasplakinolide, a cytotoxic natural product, induces actin polymerization and competitively inhibits the binding of phalloidin to F-actin.* J. Biol. Chem., **269** *(21)*, 14869-14871.

[142] Holzinger, A. and Meindl, U. (1997): *Jasplakinolide, a novel actin targeting peptide, inhibits cell growth and induces actin filament polymerization in the green alga Micrasterias.* Cell Motil. Cytoskeleton, **38** *(4)*, 365-372.

[143] Noireaux, V., Golsteyn, R.M., Friederich, E. *et al.* (2000): *Growing an actin gel on spherical surfaces.* Biophys. J., **78** *(3)*, 1643-1654.

[144] Rotsch, C. and Radmacher, M. (2000): *Drug-Induced Changes of Cytoskeletal Structure and Mechanics in Fibroblasts: An Atomic Force Microscopy Study.* Biophys. J., **78** *(1)*, 520-535.

[145] Zhang, X., Cui, X., Cheng, L. *et al.* (2012): *Actin stabilization by jasplakinolide affects the function of bone marrow-derived late endothelial progenitor cells.* PLoS One, **7** *(11)*, e50899.

[146] Shurety, W., Stewart, N.L., and Stow, J.L. (1998): *Fluid-phase markers in the basolateral endocytic pathway accumulate in response to the actin assembly-promoting drug Jasplakinolide.* Mol. Biol. Cell, **9** *(4)*, 957-975.

[147] Bubb, M.R., Spector, I., Beyer, B.B., and Fosen, K.M. (2000): *Effects of jasplakinolide on the kinetics of actin polymerization. An explanation for certain in vivo observations.* J. Biol. Chem., **275** *(7)*, 5163-5170.

[148] Gardel, M.L., Shin, J.H., MacKintosh, F.C. *et al.* (2004): *Elastic behavior of cross-linked and bundled actin networks.* Science, **304** *(5675)*, 1301-1305.

[149] Lieleg, O., Claessens, M.M.A.E., and Bausch, A.R. (2010): *Structure and dynamics of cross-linked actin networks.* Soft Matter, **6** *(2)*, 218-225.

[150] Bulut, G., Hong, S.H., Chen, K. *et al.* (2012): *Small molecule inhibitors of ezrin inhibit the invasive phenotype of osteosarcoma cells.* Oncogene, **31** *(3)*, 269-281.

[151] Hayashi, H., Tamura, A., Krishnan, D. *et al.* (2013): *Ezrin Is Required for the Functional Regulation of the Epithelial Sodium Proton Exchanger, NHE3.* PLoS One, **8** *(2)*, e55623.

[152] Ozawa, M., Hoschützky, H., Herrenknecht, K., and Kemler, R. (1990): *A possible new adhesive site in the cell-adhesion molecule uvomorulin.* Mechanisms of Development, **33** *(1)*, 49-56.

[153] McNeil, E., Capaldo, C.T., and Macara, I.G. (2006): *Zonula occludens-1 function in the assembly of tight junctions in Madin-Darby canine kidney epithelial cells.* Mol. Biol. Cell, **17** *(4)*, 1922-1932.

[154] Schneider, D., Baronsky, T., Pietuch, A. *et al.* (2013): *Tension monitoring during epithelial-to-mesenchymal transition links the switch of phenotype to expression of moesin and cadherins in NMuMG cells.* PLoS One, **8** *(12)*, e80068.

[155] Gumbiner, B.M. (2005): *Regulation of cadherin-mediated adhesion in morphogenesis.* Nat. Rev. Mol. Cell Biol., **6** *(8)*, 622-634.

[156] Niessen, C.M., Leckband, D., and Yap, A.S. (2011): *Tissue organization by cadherin adhesion molecules: dynamic molecular and cellular mechanisms of morphogenetic regulation.* Physiol. Rev., **91** *(2)*, 691-731.

[157] El-Amraoui, A. and Petit, C. (2013): *Cadherin defects in inherited human diseases.* Prog. Mol. Biol. Transl. Sci., **116**, 361-384.

[158] Roh-Johnson, M., Shemer, G., Higgins, C.D. *et al.* (2012): *Triggering a cell shape change by exploiting preexisting actomyosin contractions.* Science, **335** *(6073)*, 1232-1235.

[159] Ladoux, B., Anon, E., Lambert, M. *et al.* (2010): *Strength dependence of cadherin-mediated adhesions.* Biophys. J., **98** *(4)*, 534-542.

[160] Leckband, D.E., le Duc, Q., Wang, N., and de Rooij, J. (2011): *Mechanotransduction at cadherin-mediated adhesions.* Curr. Opin. Cell Biol., **23** *(5)*, 523-530.

[161] Martin, A.C., Gelbart, M., Fernandez-Gonzalez, R., Kaschube, M., and Wieschaus, E.F. (2010): *Integration of contractile forces during tissue invagination.* J. Cell Biol., **188**, 735-749.

[162] Rauzi, M., Verant, P., Lecuit, T., and Lenne, P.F. (2008): *Nature and anisotropy of cortical forces orienting Drosophila tissue morphogenesis.* Nat. Cell Biol., **10** *(12)*, 1401-1410.

[163] Sawyer, J.K., Harris, N.J., Slep, K.C., Gaul, U., and Peifer, M. (2009): *The Drosophila afadin homologue Canoe regulates linkage of the actin cytoskeleton to adherens junctions during apical constriction.* J. Cell Biol., **186** *(1)*, 57-73.

[164] Sinha, B., Koster, D., Ruez, R. *et al.* (2011): *Cells respond to mechanical stress by rapid disassembly of caveolae.* Cell, **144** *(3)*, 402-413.

[165] Mayor, S. (2011): *Need tension relief fast? Try caveolae.* Cell, **144** *(3)*, 323-324.

[166] Lahtinen, U., Honsho, M., Parton, R.G., Simons, K., and Verkade, P. (2003): *Involvement of caveolin-2 in caveolar biogenesis in MDCK cells.* FEBS Lett., **538** *(1-3)*, 85-88.

[167] Vogel, U., Sandvig, K., and van Deurs, B. (1998): *Expression of caveolin-1 and polarized formation of invaginated caveolae in Caco-2 and MDCK II cells.* J. Cell Sci., **111**, 825-832.

Appendix

A List of Abbreviations and Symbols

A	Area
AC	Alternate current
ADP	Adenosine diphosphate
AFM	Atomic force microscope
ARF	ADP ribosylation factor
Arp2/3	Actin related protein complex 2/3
ATP	Adenosine triphosphate
BSA	Bovine serum albumin
c	Concentration
cDNA	Complementary deoxyribonucleic acid
C-ERMAD	C-terminal ezrin, radixin, moesin association domain
C_m	Membrane capacity
CME	Clathrin-mediated endocytosis
CPE	Constant phase element
ctrl	Control
D	Diffusion coefficient
DAPI	4',6-diamidino-2-phenylindole
DMSO	Dimethyl sulfoxide
DNA	Deoxyribonucleic acid
DTT	Dithiothreitol
E	Young's modulus
ECIS	Electric cell-substrate impedance sensing
EDTA	Ethylenediaminetetraacetic acid
EMT	Epithelial-to-mesenchymal transition
ERM	Ezrin radixin moesin

F	Force
F_{tether}	Tether rupture force
FBS	Fetal bovine serum
FERM domain	4.1 ezrin, radixin, moesin domain
FITC	Fluorescein isothiocyanate
GDA	Glutardialdehyde
GFP	Green fluorescence protein
GTP	Guanosine triphosphate
h	Height
HEPES	4-(2-hydroxyethyl)-1-piperazineethanesulfonic acid
I	Current
i	Imaginary unit
IgG	Immunoglobulin G
Jas	Jasplakinolide
K_A	Area compressibility modulus
$\tilde{K}_A$	Apparent area compressibility modulus
k_B	Boltzmann constant
Lat. A	Latrunculin A
LB medium / agar	Lysogeny broth medium / agar
MDCK	Madine-Darby canine kidney
MEM	Minimal essential medium
mRNA	Messenger RNA
NA	numerical aperture
NSC	NSC 668394
PBS^{--}	phospate buffered saline without calcium and magnesium
PFA	Paraformaldehyde
PIP_2	Phosphatidylinositol 4,5-bisphosphate
R	Electrical resistance
R_b	Barrier resistance
r	Radius

r_{sphere}	Radius of a sphere
RIPA buffer	Radioimmunoprecipitation assay buffer
RISC	Ribonucleic acid-induced silencing complex
RNA	Ribonucleic acid
SDS	Sodium dodecyl sulphate
SEM	Standard error of the mean
siRNA	Small interfering RNA
T	Tension (Temperature)
t_{act}	Tension originating from active cortex contraction
t_0	Overall tension
t_t	Membrane tension
U	Voltage (electric potential difference)
wt	Wild type
Z	Impedance
Z_{im}	Imaginary part of impedance
Z_{re}	Real part of impedance
ZO-1	Zonula occludens-1
α	Describes cell-substrate distance
γ_{ad}	Tension originating from membrane-cytoskeleton attachment
γ_m	In-plane tension
δ	Indentation depth
η	Viscosity
κ	Bending modulus
ν	Poisson ratio
v_t	Pulling velocity
θ	Half opening angle of the conical indenter
ϕ	Spreading angle
ω	Frequency

B List of Figures

C List of Tables

Danksagung

“Einer allein kann kein Dach tragen“ heißt ein altes afrikanisches Sprichwort. An vielen Stellen durfte ich erleben, wie groß und schwer das Dach „Doktorarbeit“ manchmal sein kann. Zum Glück gab es immer Menschen, die mich begleitet und „mit angefasst“ haben, wenn das Dach zu schwer wurde. Dafür möchte ich mich an dieser Stelle aufrichtig bedanken. „Ein Freund ist jemand, der den Weg mit dir teilt“ lautet ein weiteres afrikanisches Sprichwort.

Prof. Dr. Andreas Janshoff danke ich für die Bereitstellung des umfangreichen und spannenden Themas. Danke für deinen Enthusiasmus, aber auch für alle ehrlichen und fairen Diskussionen. Danke für die großen Freiheiten, die du mir gegeben hast, mich in vielen verschiedenen Dingen weiterzubilden und das damit verbundene Vertrauen.

Den Mitgliedern meines Thesis Committees, Prof. Dr. Sarah Köster und Prof. Dr. Mikael Simons danke ich für die angenehme Betreuung und für alles Feedback und alle Diskussionen während der Thesis Committee Meetings. Danke für die spannenden Kooperationen.

Ich danke den weiteren Mitgliedern der Prüfungskommission, Prof. Dr. Michael Meinecke, Dr. Florian Rehfeldt und Prof. Dr. Silvio Rizzoli.

Der Konrad-Adenauer-Stiftung (Begabtenförderung) danke ich für die finanzielle Unterstützung im Rahmen der Promotionsförderung und für die ideelle Förderung mit vielen hervorragenden Seminaren zu spannenden Themen. Danke Dr. Gernot Uhl für die gute Stipendiaten-Betreuung.

Burkhardt, dir danke ich für alle kleinen und großen Hilfen bei der Datenanalyse und für die angenehme Zusammenarbeit im PC-Nebenfach-Modul. Danke, dass du mich aus dem Loch im Labor gezogen hast.

Ingo, danke, dass du mich schon seit meiner Bachelorarbeit begleitest und mich immer noch aushältst. Danke für alle Unterstützung in meiner Dissertation, aber auch in vielen anderen Dinge. Danke für die intensiven Gespräche.

Angela und Anja, manchmal habt ihr geknurrt, weil ich meine Vorstellungen in der Zellkultur hatte. Dennoch habt ihr immer alles mitgetragen, was ich ausprobieren wollte. Danke für diese Bereitschaft. Danke aber auch für euren zuverlässigen Zell-Service und eure Flexibilität, die weit über das normale Maß hinausgeht. Euer Wissen hat mir den Einstieg in die Zellkultur erst ermöglicht.

Petra, was wäre ein Arbeitstag ohne einen Besuch bei dir gewesen? Danke für all deine Unterstützung. Danke für alles, was ich durch dich lernen durfte und die vielen lustigen Momente. Danke für unzählige Liter Kaffee.

Anna, dir danke ich ganz besonders. Du hast mich in meiner Masterarbeit betreut und warst auch zu Beginn meiner Doktorarbeit noch im Arbeitskreis und hattest immer ein offenes Ohr. Danke für deine Unterstützung und die vielen gemeinsamen Experimente. Danke für dein Wesen und deine geradlinige Art.

Thilo, danke, dass wir seit unserer Masterarbeit gemeinsam im Arbeitskreis gearbeitet haben. Danke für die vielen guten Gespräche und vor allem für deine Hilfsbereitschaft.

Helen, meine Tischnachbarin, danke, dass wir uns ein Büro teilen durften. Danke für deine offene und direkte Art, für deine Verlässlichkeit und für die gemeinsamen Projekte und guten Diskussionen. Danke für die Fortführung der „Schlechten-Witze-Kasse“. Ganz besonders danke ich dir für das kritische Lesen meiner Doktorarbeit und die vielen Anmerkungen.

Moechen, danke für die vielen lustigen Gespräche innerhalb und außerhalb der Uni. Danke für deine positive Art und die lustigen gemeinsamen Arbeitskreisabende. Danke für den Heidegeist und alle anderen alkoholischen Neukreationen von dir.

Mark, danke für dein entspanntes Wesen und deine lockere Art. Die Betreuung während deines Praktikums und deiner Bachelorarbeit hat sehr viel Spaß gemacht.

Danke dem gesamten Arbeitskreis Janshoff, den alten Janseaten für die gemeinsame Zeit und den jungen Janseaten, die immer wieder frischen Wind in unsere Abteilung bringen.

Dem Arbeitskreis Steinem danke ich für die gute und angenehme Zusammenarbeit.

Michaela, danke für die gemeinsame Zeit an der Uni. Danke für deine Hilfe und vor allem den Spaß beim Western Blot. Danke für die lustige Tagung in Lissabon und viele phantastische Törtchen.

Und dann sind da noch die Menschen außerhalb der Uni, denen mein besonderer Dank gilt.

Mein größter Dank und meine Hochachtung gilt meinen Eltern. Danke für euren grenzenlosen Rückhalt und für euren Glauben an mich. Ihr habt mir immer den Rücken gestärkt. Der Ort, an den ich immer wieder gerne zurückkomme, nach Hause, gibt mir Sicherheit und Halt. Danke!

Olli, danke, dass wir uns durch das Studium begegnet sind. Danke für dein offenes Ohr und dass du einfach immer da bist, wenn ich dich brauche. Danke für die vielen Abende in der Stadt oder zu Hause mit Bier und Pizza.

Wolfram, der Dank für das sorgfältige Lesen meiner Arbeit ist nichts im Vergleich dazu, wofür ich dir sonst noch danken möchte. Da das aber den Umfang der Danksagung sprengen würde, sage ich ganz einfach: Danke!